



Universitatea *Transilvania* din Braşov

HABILITATION THESIS

**Color and Multispectral Texture Image Analysis.
Models, Features and Applications**

**Domain: Electronics and Telecommunications
Engineering**

**Author: Laurențiu-Mihail Ivanovici
University: Universitatea Transilvania din Braşov**

BRAŞOV, 2015

Contents

Contents	i
I Abstract (in Romanian)	1
II Scientific and professional achievements and the evolution and development plans for career development	21
II.1 Scientific and professional achievements	23
1 Color and multispectral texture images	25
2 Fractal models	31
2.1 Midpoint displacement algorithm	32
2.2 Extension to color	35
2.3 Vector color fractal generator	38
2.4 Visual impact of increment distribution	43
2.5 Weierstrass function	45
2.6 Perlin noise	46
3 Fractal features	49
3.1 Fractal dimension	49
3.2 Fractal dimension estimation	51
3.2.1 The box-counting dimension	51
3.2.2 Probabilistic box-counting	53
3.2.3 Correlation dimension	60
3.2.4 Covering blanket	66
3.3 Lacunarity	67
3.4 Limitations of current estimation techniques	69
3.5 An equivalent estimation approach	72

4	Morphological features	75
4.1	Mathematical morphology tools	76
4.1.1	Mathematical morphology for binary images	76
4.1.2	Mathematical morphology for gray-scale images	78
4.1.3	Applications and texture feature extraction	80
4.1.4	Mathematical morphology for color images	83
4.2	Pseudo-morphologies	85
4.2.1	Probabilistic pseudo-morphology	85
4.2.2	Probabilistic color pseudo-morphology	87
4.2.3	Maximum distance pseudo-morphology	91
4.3	Covering blanket	94
4.4	Granulometry or pattern spectrum	96
4.5	Morphological covariance	98
5	Applications	101
5.1	Image segmentation	101
5.2	Watershed segmentation	106
5.3	Active contours	107
5.4	Feature-based textured image segmentation	110
5.5	Color texture classification	112
5.6	Discussion	113
II.2	The evolution and development plans for career de- velopment (in Romanian)	115
II.3	Bibliography	127

Part I

Abstract (in Romanian)

Rezumat

Cercetările care constituie suportul pentru această teză de abilitare¹ au început în 2007 în colaborare cu Noël Richard de la laborator de cercetare XLIM-SIC, Université de Poitiers, Franța. Pe lângă prezentarea și evidențierea realizărilor notabile de până acum, în teza de față se regăsesc direcțiile viitoare de cercetare. După o scurtă introducere despre imaginile color și multispectrale reprezentând texturi abordate modele fractale ce pot fi utilizate pentru modelarea matematică a texturilor. Modelele sunt utile atât pentru sinteză cât și pentru analiză. În cadrul analizei sunt abordate diverse tehnici de extragere de trăsături în vederea caracterizării texturilor, în special trăsături fractale și morfologice². În finalul tezei sunt prezentate ca aplicații segmentarea imaginilor și clasificarea texturilor.

Texturile reprezintă variația unui semnal (i.e. imagine) la o scală mai mică decât cea de interes [96]. Texturile pot fi regulate, cvasi-regulate sau neregulate (vezi Fig. 1). Cele mai multe texturi naturale sunt neregulate. O altă taxonomie împarte texturile în deterministe sau probabiliste.



Fig. 1: Tipuri de texturi.

Noțiunea de textură a fost introdusă în anii 60-70 în contextul analizei imaginilor în nivele de gri ce prezentau variații pe suprafața obiectelor de interes, fapt ce făcea dificilă operația de segmentare. După Haralick [53] texturile pot fi descrise folosind termeni precum fin, rugos, ridat ș.a.

¹M. Ivanovici, “Color and Multispectral Texture Image Analysis – Models, Features and Applications”, Transilvania University Press, ISBN 978-606-19-0587-4, 2015, <http://miv.unitbv.ro/downloads/MIVCMTIAMFA2015.pdf>

²Este vorba aici de tehnici ce țin de morfologia matematică - domeniu fundamental pentru abordări neliniare în prelucrarea și analiza imaginilor. Vezi P. Soille *Mathematical morphology and image analysis*.

Haralick a pus bazele analizei de textură și a propus o serie de 14 trăsături pentru analiza texturilor [53] pe baza matricilor de dependență spațială a nivelelor de gri (cunoscute drept *matrici de coocurență*): omogenitatea, contrastul, numărul și natura frontierelor sau complexitatea unei texturi. De la Haralick încoace diverse tehnici de caracterizare a texturilor au fost propuse și clasificate în [117] ca: geometrice, statistice, bazate pe modele sau metode de prelucrarea semnalelor. Câteva tehnici importante sunt descrise în [93] [33] [65] [72].

În cadrul acestei teze ne concentrăm atenția asupra noțiunii de complexitate, în contextul analizei de texturi. Există diverse definiții ale complexității, cum ar fi complexitatea Kolmogorov sau entropia. Recent, împreună cu N. Richard am propus și înființat un nou Comitet Tehnic TC 8-14 în cadrul Diviziei 8 a CIE³ intitulat *Specification of Spatio-Chromatic Complexity*. Obiectivul acestui comitet este de a defini complexitatea spațio-cromatică a unei texturi color, într-o formă vectorială și generică, care să țină cont de variațiile spațiale și spectrale ale texturii, în vederea elaborării unui standard internațional.

Pentru validarea modelelor și uneltelor de analiza texturilor există diverse baze de date, unele dintre ele construite cu scopul de a testa metodele de caracterizare cu privire la invarianța la translatare, rotire, scalare sau modificarea iluminantului. Cele mai cunoscute sunt Outex [89] și Vis-*Tex*⁴. Recent, comunitatea științifică și-a orientat atenția către analiza texturilor multispectrale. Există câteva baze de date disponibile, una fiind baza CAVE⁵, Columbia University, New York care conține imagini multispectrale având 31 de benzi spectrale, de la 400 nm la 700 nm, în pași de 10 nm. Alte baze de imagini multispectrale sunt disponibile: University of East Anglia, United Kingdom⁶, Brno University of Technology, Czech Republic⁷ sau the Joint Research Center, the Institute for Environment and Sustainability⁸. Cea din urmă conține imagini satelitare achiziționate de satelitul Landat 7.

Modele fractale

Geometria fractală a fost introdusă de B. Mandelbrot în 1983 [79] pentru a descrie mulțimi auto-similare numite *fractali*. Auto-similaritatea este un concept central al geometriei fractale, fiind strâns legat de noțiunea de dimensiune și, implicit, de complexitate. Dimensiunea fractală este o măsură a complexității unui obiect fractal. Modelele fractale sunt utilizate pentru generarea de texturi sintetice, forme sau chiar peisaje în grafica compute-

³Comisia Internațională de Iluminare.

⁴<http://vismod.media.mit.edu/vismod/imagery/VisionTexture/>

⁵<http://www.cs.columbia.edu/CAVE/databases/multispectral/>

⁶<http://www2.cmp.uea.ac.uk/Research/compvis/MultiSpectralDB.htm>

⁷<http://splab.cz/en/download/databaze/multispec>

⁸<http://image2000.jrc.ec.europa.eu/DI/IM.htm>

rizată. Din multitudinea de modele, ne-am concentrat atenția pe generarea de fractali stocastici, în speță generarea de zgomot brownian fracțional. O tehnică de generare a unui astfel de zgomot se numește *random midpoint displacement* propusă de D. Saupe în [93].

Pentru proiectarea unui generator de imagini fractale color, am extins în [63] metoda *random midpoint displacement* de la nivele de gri la domeniul color⁹. Am ales să lucrăm în spațiul de culoare RGB deoarece prezintă o organizare cubică coerentă cu construcția obiectului fractal. În cazul imaginilor color RGB, incrementele cu care punctul de mijloc se deplasează reprezintă diferențe, în sensul distanței euclidiene, între vectori tri-dimensionali X_k , situați în oricare două puncte t_1, t_2 și s_1, s_2 din spațiul suport. Varianța acestor incremente este:

$$\sigma_i^2 = \left(\sqrt{\sum_{k=r,g,b} (X_k(t_1, t_2) - X_k(s_1, s_2))^2} \right)^2 \quad (1)$$

$$\sigma_i^2 = \frac{[X_r(t_1, t_2) - X_r(s_1, s_2)]^2 + [X_g(t_1, t_2) - X_g(s_1, s_2)]^2 + \dots}{\dots + [X_b(t_1, t_2) - X_b(s_1, s_2)]^2} \quad (2)$$

În ipoteza că aceste incremente sunt statistic independente pe cele trei coordonate RGB, cu alte cuvinte simulii color pe cele trei canale nu sunt corelați, putem distribui operatorul de mediere statistică la fiecare termen:

$$\sigma_i^2 = \frac{[X_r(t_1, t_2) - X_r(s_1, s_2)]^2}{\dots} + \frac{[X_g(t_1, t_2) - X_g(s_1, s_2)]^2}{\dots} + \frac{[X_b(t_1, t_2) - X_b(s_1, s_2)]^2}{\dots} \quad (3)$$

Deoarece fiecare din cei trei termeni este proporțional cu $\left(\sum_{i=1}^2 (t_i - s_i)^2 \right)^H$, conform construcției obiectului fractal în cadrul metodei originale, putem concluziona că și suma la rândul ei va fi proporțională cu diferența coordonatelor spațiale:

$$\sigma_i^2 \propto 3 \cdot \left(\sum_{i=1}^2 (t_i - s_i)^2 \right)^H \propto \left(\sum_{i=1}^2 (t_i - s_i)^2 \right)^H \quad \square \quad (4)$$

Am demonstrat astfel că modelul nostru e valabil pentru imaginile color fractale generate utilizând spațiul de culoare RGB. Din punctul de vedere al implementării, am modificat algoritmul prezentat în [93] pentru a face calcule pe triplete RGB. În Fig. 2 sunt prezentate imagini fractale color obținute, pentru care complexitatea diferă (prin valoarea factorului Hurst).

⁹M. Ivanovici, N. Richard, *Fractal Dimension of Color Fractal Images*, IEEE Transactions on Image Processing, January 2011, <http://dx.doi.org/10.1109/TIP.2010.2059032>

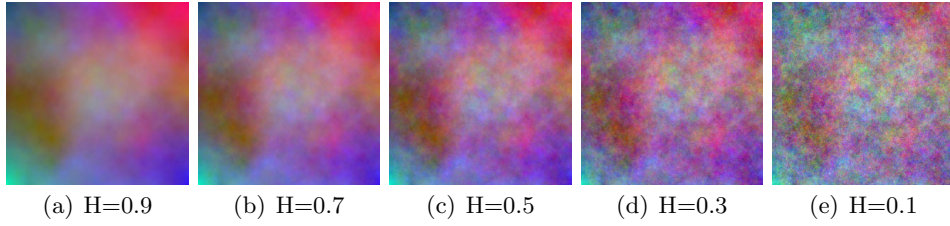


Fig. 2: Imagini color fractale generate utilizând spațiul RGB.

Trăsături fractale

Pentru analiza texturilor cu caracter fractal, stocastic ne vom opri atenția asupra a două trăsături fractale importante: dimensiunea fractală și lacunaritatea. Dimensiunea fractală este o măsură a complexității unui fractal, indicând nivelul de neregularitate a acestuia și *cât* spațiu ocupă. Lacunaritatea este o măsură fractală complementară care indică *cum* este ocupat spațiul, fiind similară unei distribuții. Trăsăturile fractale sunt utilizate pentru analiza multi-scală a imaginilor și semnalelor multidimensionale, prin observarea variației unei măsuri ca funcție de scala de analiză.

Dimensiunea fractală teoretică este dimensiunea Haudorff [40]. În practică însă, această dimensiune se estimează prin calculul fie al dimensiunii de similaritate, al dimensiunii *box-counting*, al dimensiunii de corelație sau al altor dimensiuni. Algoritmul probabilist de estimare a dimensiunii *box-counting* dim_B propus de R. Voss [123] consideră imaginea F ca fiind o mulțime de puncte într-un spațiu euclidian. După [70], aranjamentul spațial al mulțimii este caracterizat de matricea de probabilitate $P(m, \delta)$ - aceea de a avea m puncte într-un cub (box) de dimensiune δ , centrat, pe rând, în toate punctele imaginii analizate. Pentru fiecare valoare δ , matricea este normalată astfel încât:

$$\sum_{m=1}^Q P(m, \delta) = 1, \quad \forall \delta \quad (5)$$

unde Q reprezintă numărul de puncte din cuburile de dimensiune δ . Dacă notăm cu M numărul total de puncte al imaginii, numărul de cuburi care conțin m puncte este $(M/m)P(m, \delta)$. Prin urmare, numărul total de cuburi necesar pentru a acoperi imaginea este:

$$\langle N(\delta) \rangle = \sum_{m=1}^N \frac{M}{m} P(m, \delta) = M \sum_{m=1}^N \frac{1}{m} P(m, \delta) \quad (6)$$

care reprezintă un estimat al lui $N(\delta)$, deci cantitatea $\sum_{m=1}^Q \frac{1}{m} P(m, \delta)$ este direct proporțională cu $\delta^{-dim_B F}$ și poate fi utilizată pentru calcularea

dimensiunii box-counting: $N(\delta) = \sum_{m=1}^N \frac{1}{m} P(m, \delta) \propto \delta^{-dim_B}$.

Dacă în abordarea prezentată o imagine în nivele de gri poate fi modelată ca o suprafață discretă $z = f(x, y)$ într-un spațiu tri-dimensional, în care z este luminanța în fiecare punct (x, y) al spațiului suport, modelul poate fi extins la imagini color și multispectrale. În [63] am considerat imaginile color ca fiind hiper-suprafețe într-un spațiu de culoare RGB: $f(x, y) = (r, g, b)$. Prin urmare, avem de-a face cu un hiper-spațiu euclidian cinci-dimensional, iar fiecare pixel poate fi privit ca un vector cinci-dimensional (x, y, r, g, b) .

Algoritmul lui Voss definește cuburi de dimensiune δ centrate în pixelul curent $(x, y, z = f(x, y))$ și numără câți pixeli se află în interiorul cubului determinat de următoarele colțuri diagonal opuse: $(x - \frac{\delta}{2}, y - \frac{\delta}{2}, z - \frac{\delta}{2})$ și $(x + \frac{\delta}{2}, y + \frac{\delta}{2}, z + \frac{\delta}{2})$. Într-o extindere directă a algoritmului lui Voss la imagini color am număra pixelii $F = f(x, y, r, g, b)$ pentru care distanța euclidiană la centrul hiper-cubului $F_c = f(x_c, y_c, r_c, g_c, b_c)$ ar fi mai mică decât δ :

$$|F - F_c| = \sqrt{\sum_{i=1}^5 |f_i - f_{ci}|^2} \leq \delta \quad (7)$$

Dat fiind că distanța euclidiană în spațiul RGB nu corespunde distanței perceptuale între culori, preferăm să folosim distanța Minkowski:

$$|F - F_c| = \max(|f_i - f_{ci}|) \leq \delta \quad \forall i = \overline{1, 5} \quad (8)$$

Practic, pentru un anume pătrat de dimensiune δ din domeniul suport (x, y) , numărăm câți pixeli se situează într-un cub RGB tri-dimensional de dimensiune δ centrat în pixelul curent. În Figura 3 sunt prezentate trei texturi naturale (orange, psoriazis și cladonia), pentru care rezultă curbele $N(\delta)$ din graficul alăturat și următoarele dimensiuni fractale color: 2.0, 3.39 și 3.71.

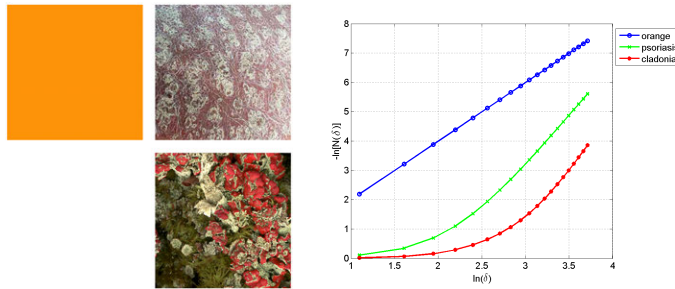


Fig. 3: Trei texturi și curbele $N(\delta)$ corespunzătoare.

Lacunaritatea, așa cum a fost definită de Voss, este bazată pe momentele de ordinul unu, $M(\delta)$ și de ordinul doi, $M^2(\delta)$ calculate pe baza probabilităților $P(m, \delta)$:

$$M(\delta) = \sum_{m=1}^N mP(m, \delta) \quad M^2(\delta) = \sum_{m=1}^N m^2P(m, \delta) \quad (9)$$

$$\Lambda(\delta) = \frac{M^2(\delta) - (M(\delta))^2}{(M(\delta))^2} \quad (10)$$

Modelând imaginile color la fel cum am făcut-o pentru estimarea dimensiunii fractale box-counting, obținem următoarele rezultate¹⁰ prezentate în Fig. 4 și anume curbele de lacunaritate obținute pentru trei din imaginile fractale color din Fig. 2 și cele trei texturi din Fig. 3.

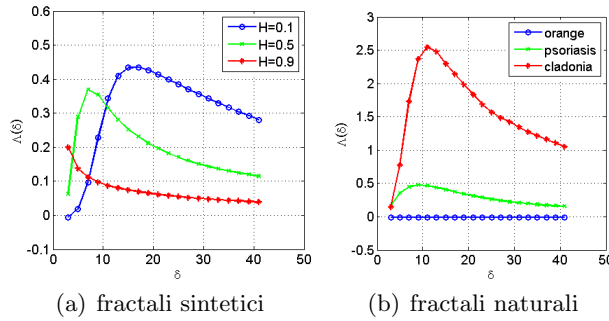


Fig. 4: Curbe de lacunaritate.

După cum a spus Mandelbrot, interpretarea curbelor de lacunaritate are legătură cu perceperea *munților* și *văilor* din complexitatea hipersuprafeței unei texturi.

Trăsături morfologice

Domeniul de morfologie matematică a fost fondat de G. Matheron [83] și J. Serra [110] și constituie un cadru matematic pentru prelucrări neliniare și analiză de imagini. Morfologia matematică a fost introdusă pentru imagini binare, operatorii morfologici bazându-se pe teoria mulțimilor [47]. Extinderea morfologiei matematice la domeniul imaginilor în nivele de gri se bazează pe teoria laticelor, care implică o ordonare parțială a valorilor pixelilor din imagine, astfel încât să existe un *infimum* și un *supremum* pentru orice submulțime de valori de pixeli. Aplicațiile morfologiei matematice includ filtrare, segmentare sau analiză de textură [114].

Extinderea morfologiei matematice la domeniul imaginilor color și multispectrale nu este directă, din cauza valorilor vectoriale ale pixelilor din

¹⁰M. Ivanovici, N. Richard, The lacunarity of colour fractal images, 16th IEEE International Conference on Image Processing, 2009, <http://dx.doi.org/10.1109/ICIP.2009.5414394>

imagine și implicit a nevoii de a defini o ordine potrivită cu natura vectorială. Metodele de ordonare a vectorilor se pot clasifica în patru categorii [11]: marginală, redusă, condițională sau parțială, fiecare dintre acestea având avantaje și dezavantaje în funcție de rezultatul lor vizavi de o aplicație anume.

Diverse abordări au fost propuse pentru morfologie matematică pentru imagini color și multispectrale [5]. În paralel cu dezvoltarea acestor abordări, în cadrul cărora operatorii respectă toate proprietățile morfologiei matematice, au fost propuse diverse *pseudo-morfologii*. Acestea nu necesită o ordonare a valorilor pixelilor ci se bazează pe estimarea valorilor extreme ale unei mulțimi date [51] [4] [17].

În [60] am propus estimarea valorilor extreme ale unei mulțimi, respectiv *infimum* și *supremum*, utilizând inegalitatea lui Cebîșev, ce permite estimarea probabilității ca o submulțime de vectori să aparțină unui interval centrat în jurul mediei distribuției [25]. Fie ξ o variabilă aleatoare de medie μ_ξ și dispersie σ_ξ , atunci inegalitatea lui Cebîșev spune că:

$$P\{|\xi - \mu_\xi| \geq k\sigma_\xi\} \leq \frac{1}{k^2} \quad (11)$$

Ecuția (11) este valabilă pentru orice distribuție cu medie și dispersie finite [91]. Utilizând parametrul k putem determina valori pseudo-extreme apropiate de minimul respectiv maximul distribuției. Prin urmare, putem defini pseudo-extremele probabilistice ale unei distribuții, \mathcal{E}^+ și \mathcal{E}^- , pe baza inegalității lui Cebîșev, astfel:

$$\begin{cases} \mathcal{E}^+ \triangleq \mu_\xi + k\sigma_\xi \\ \mathcal{E}^- \triangleq \mu_\xi - k\sigma_\xi \end{cases} \quad (12)$$

Alegând valoarea optimă pentru k , eroarea dintre extremele probabilistice și cele reale ale distribuției poate fi cât mai redusă. Pe baza acestei abordări, în [17] am propus o pseudo-morfologie probabilistică (PPM) pentru imagini în nivele de gri, există apoi la domeniul imaginilor color¹¹. Dată fiind o imagine $f : \mathcal{D}_f \rightarrow \mathcal{S} \subset \mathbb{R}$, și un element structurand plat g având suportul \mathcal{D}_g , am definit pseudo-erodarea și pseud-dilatarea după cum urmează:

$$[\varepsilon_g(f)](x) = \bigwedge_{z \in \mathcal{D}_g} f(x+z) \triangleq \mu_\xi - k\sigma_\xi, \quad \forall x \in \mathcal{D}_f \quad (13)$$

$$[\delta_g(f)](x) = \bigvee_{z \in \mathcal{D}_g} f(x-z) \triangleq \mu_\xi + k\sigma_\xi, \quad \forall x \in \mathcal{D}_f \quad (14)$$

¹¹A. Căliman, M. Ivanovici, N. Richard, Probabilistic pseudo-morphology for grayscale and color images, Pattern Recognition, ISSN 0031-3203, February 2014, <http://dx.doi.org/10.1016/j.patcog.2013.08.021>

unde variabila aleatoare ξ modelează nivelele de gri ale pixelilor din domeniul $\mathcal{D}_f \cap \mathcal{D}_g$. Media μ_ξ și dispersia σ_ξ sunt calculate local, în funcție de dimensiunea și poziția elementului structurant. Pentru valori mici ale lui k (0.2), pseudo-extremele probabilistice sunt aproape de valoarea medie statistică, iar comportamentul operatorilor PPM este similar cu al unui filtru liniar de netezire (vezi Fig. 5 și 6). Pentru $k = 2$, o valoare optimă pentru imaginea Lenna, rezultatele sunt similare cu acelea obținute în cazul utilizării operatorilor morfologiei matematice clasice pentru imagini în nivele de gri (GLMM). Se pot observa câteva diferențe: morfologia clasică introduce artefacte (e.g. la partea superioară a pălăriei). Datorită filtrării implicite ale operatorilor PPM, pseudo-erodările și pseudo-dilatările nu prezintă astfel de artefacte, forma elementului structurant nefiind vizibilă. În plus, abordarea PPM este capabilă să păstreze detalii morfologice (e.g. cele de la sprâncene) sau ale texturii (e.g. penele de la pălărie). Toate acestea dovedesc faptul că operatorii PPM dobândesc o anumită robustețe, fiind mai puțin influențați de zgomot, iar structurile morfologice și texturale sunt mai bine păstrate. Pentru o valoare mare cum ar fi $k = 4$, extremele probabilistice sunt departe de media statistică locală, fiind aproape de negru și alb - extremele intervalului de nivele de gri. Acest caz este similar cu cel al morfologiei clasice utilizând elemente structurante non-plate.

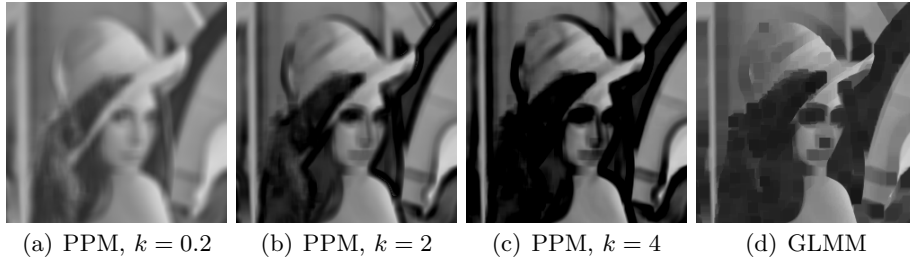


Fig. 5: Erodări PPM pentru diverse valori ale lui k , comparativ cu GLMM, ambele utilizând un element structurant plat de dimensiune 11×11 .

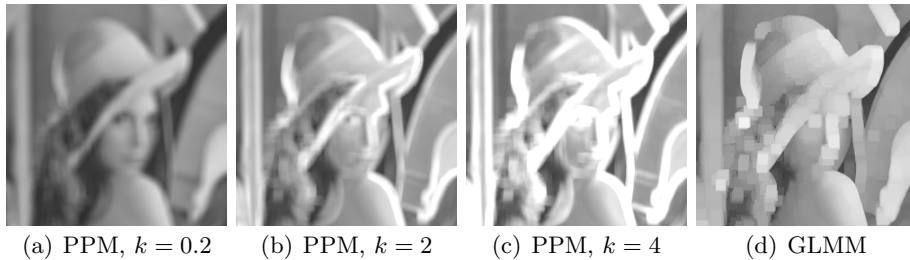


Fig. 6: Dilatări PPM pentru diverse valori ale lui k , comparativ cu GLMM, ambele utilizând un element structurant plat de dimensiune 11×11 .

Pentru imaginile color și multispectrale, valorile pixelilor sunt vectoriale. Concret, în cazul imaginilor color acestea pot fi modelate ca $f : \mathcal{D}_f \rightarrow \mathcal{S} \subset \mathbb{R}^3$. Pentru a exinde abordarea PPM la domeniul color sau multispectral, trebuie să evaluăm corect varianța pixelilor în vederea utilizării inegalității lui Cebîșev. În [17] am propus o extindere la color și multispectral bazată pe analiza componentelor principale (PCA). PCA este o transformare liniară care are ca scop identificarea unui nou spațiu de reprezentare, în care varianța datelor este maximizată pe una din axe, denumite componente principale [92]. Versorii spațiului sunt vectorii proprii ai matricii de covarianță. În Figura 7 este ilustrată construcția pseudo-extremelor probabilistice (pe prima și pe ambele componente principale) în cazul unor vectori bi-dimensionali.

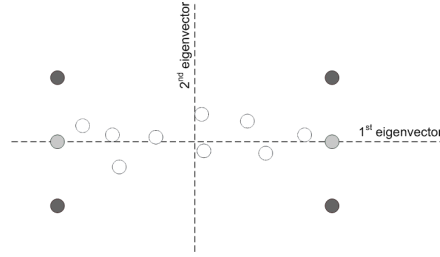


Fig. 7: Calculul pseudo-extremelor unei mulțimi de vectori bidimensionali (alb): utilizând doar prima componentă principală (gri deschis) sau ambele componente principale (gri închis).

După utilizarea PCA și a inegalității lui Cebîșev, cele două pseudo-extreme trebuie ordonate și etichetate ca fiind maxim, respectiv minim (problemă intrinsecă datorită naturii vectoriale a datelor). În lucrarea [17] am ordonat pseudo-extremele construite pe prima componentă principală utilizând un set de trei perechi de puncte de referință, alese arbitrar, ordonate *a priori*. Procesul de ordonare este realizat pe baza proiecțiilor pseudo-extremelor pe axa determinată de punctele de referință. Procesul este ilustrat în Figura 8, unde ordonarea *a priori* considerată pentru punctele de referință este $R^+ > R^-$ și prin urmare pseudo-extremele E_α și E_β vor fi ordonate $E_\alpha > E_\beta$.

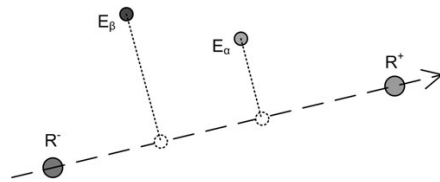


Fig. 8: Ordonarea extremelor E_α și E_β folosind referințele R^- și R^+ .

În [18], referințele au fost calculate automat ca fiind pseudo-extremele globale, pe fiecare componentă principală, pentru întreaga distribuție a valorilor de pixeli ai imaginii. În acest fel, trei perechi de referințe au fost obținute după cum urmează: $(\mathcal{R}_1^-, \mathcal{R}_1^+)$, $(\mathcal{R}_2^-, \mathcal{R}_2^+)$, $(\mathcal{R}_3^-, \mathcal{R}_3^+)$, cu $\mathcal{R}_i^- < \mathcal{R}_i^+$, $i = \overline{1, 3}$. Ordonarea referințelor a fost realizată utilizând proiecțiile acestora pe axa alb-negru a spațiului de culoare. Astfel, operațiile de pseudo-erodare și pseudo-dilatate pentru o imagine color f și un element structurant g de suport \mathcal{D}_g pot fi definite ca:

$$\begin{aligned} [\varepsilon_g(f)](x) &= \bigwedge_{z \in \mathcal{D}_g} f(x+z) \triangleq \\ &= \begin{cases} \arg \min_i [\overrightarrow{\mathcal{R}_0^- \mathcal{R}_0^+} \cdot \overrightarrow{\mathcal{R}_0^- i}], i \in \{\mathcal{E}_\alpha, \mathcal{E}_\beta\} \\ \arg \min_i [\overrightarrow{\mathcal{R}_1^- \mathcal{R}_1^+} \cdot \overrightarrow{\mathcal{R}_1^- i}], i \in \{\mathcal{E}_\alpha, \mathcal{E}_\beta\} \text{ if } \overrightarrow{\mathcal{R}_0^- \mathcal{R}_0^+} \cdot \overrightarrow{\mathcal{E}_\alpha \mathcal{E}_\beta} = 0 \\ \arg \min_i [\overrightarrow{\mathcal{R}_2^- \mathcal{R}_2^+} \cdot \overrightarrow{\mathcal{R}_1^- i}], i \in \{\mathcal{E}_\alpha, \mathcal{E}_\beta\} \text{ if } \overrightarrow{\mathcal{R}_0^- \mathcal{R}_0^+} \cdot \overrightarrow{\mathcal{E}_\alpha \mathcal{E}_\beta} = \overrightarrow{\mathcal{R}_1^- \mathcal{R}_1^+} \cdot \overrightarrow{\mathcal{E}_\alpha \mathcal{E}_\beta} = 0 \end{cases} \quad (15) \end{aligned}$$

$$\begin{aligned} [\delta_g(f)](x) &= \bigvee_{z \in \mathcal{D}_g} f(x-z) \triangleq \\ &= \begin{cases} \arg \max_i [\overrightarrow{\mathcal{R}_0^- \mathcal{R}_0^+} \cdot \overrightarrow{\mathcal{R}_0^- i}], i \in \{\mathcal{E}_\alpha, \mathcal{E}_\beta\} \\ \arg \max_i [\overrightarrow{\mathcal{R}_1^- \mathcal{R}_1^+} \cdot \overrightarrow{\mathcal{R}_1^- i}], i \in \{\mathcal{E}_\alpha, \mathcal{E}_\beta\} \text{ if } \overrightarrow{\mathcal{R}_0^- \mathcal{R}_0^+} \cdot \overrightarrow{\mathcal{E}_\alpha \mathcal{E}_\beta} = 0 \\ \arg \max_i [\overrightarrow{\mathcal{R}_2^- \mathcal{R}_2^+} \cdot \overrightarrow{\mathcal{R}_1^- i}], i \in \{\mathcal{E}_\alpha, \mathcal{E}_\beta\} \text{ if } \overrightarrow{\mathcal{R}_0^- \mathcal{R}_0^+} \cdot \overrightarrow{\mathcal{E}_\alpha \mathcal{E}_\beta} = \overrightarrow{\mathcal{R}_1^- \mathcal{R}_1^+} \cdot \overrightarrow{\mathcal{E}_\alpha \mathcal{E}_\beta} = 0 \end{cases} \quad (16) \end{aligned}$$

unde $\overrightarrow{\mathcal{R}_i^- \mathcal{R}_i^+}$ este direcția ordonată determinată de punctele de referință \mathcal{R}_i^- și \mathcal{R}_i^+ , iar \mathcal{E}_α și \mathcal{E}_β reprezintă pseudo-extremele culorilor din suportul elementului structurant. În Figura 9 sunt prezentate câteva rezultate ale abordării PPM pe imaginea color "Miro". Toate operațiile au fost realizate în spațiul de culoare RGB deoarece acesta are componente corelate, utilizarea PCA având astfel sens.

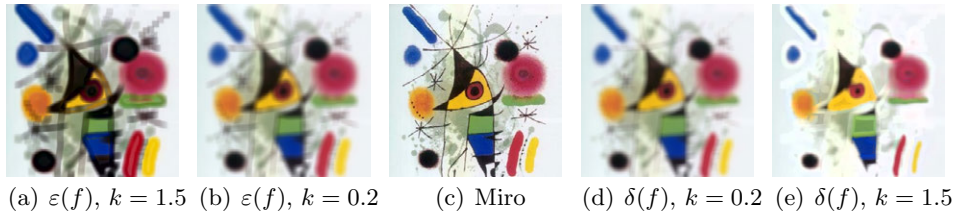


Fig. 9: Pseudo-erodări și pseudo-dilatări utilizând un element structurant de dimensiune 11×11 și două valori ale parametrului k .

Poate fi observată o anumită similaritate între rezultatele abordării extinse la domeniul color și cea pentru imagini în nivele de gri: (i) pseudo-dilatările *deschid* imaginea, pe când pseudo-erodările o fac mai întunecată, ca urmare a utilizării axei alb-negru pentru ordonarea culorilor de referință;

(ii) un efect de filtrare trece-jos, intrinsec procesului statistic; (iii) influența parametrului k al inegalității lui Cebîșev - o valoare mică determină rezultate similare cu cele ale unui filtru de netezire, pe când valori mari determină un comportament ne-liniar.

În [29] am propus o pseudo-morfologie bazată de distanța maximă calculată pentru valorile vectoriale ale pixelilor dintr-o vecinătate¹². Dată fiind o imagine color reprezentată în spațiul CIE Lab, $f : \mathcal{D}_f \rightarrow \mathbb{R}^3$, de suport $\mathcal{D}_f \subset \mathbb{Z}^2$, definim pseudo-extremele din vecinătatea \mathcal{D}_g dată de elementul structurant plat g ca fiind:

$$\{\mathbf{e}_a, \mathbf{e}_b\} = \arg \max_{f(i), f(j)} d(f(i), f(j)), \quad \forall i, j \in \mathcal{D}_f \cap \mathcal{D}_g \quad (17)$$

unde $d(\cdot, \cdot)$ reprezintă distanța CIE Lab ΔE [112]. După calcularea pseudo-extremelor, problema etichetării acestora se poate rezolva pe baza distanțelor la axa alb-negru sau la culori de referință [17] [18]. Am optat pentru o ordonare lexicografică $<_\ell$. Pentru doi vectori \mathbf{v} și \mathbf{v}' :

$$\forall \mathbf{v}, \mathbf{v}' \in \mathbb{R}^n, \mathbf{v} <_\ell \mathbf{v}' \Leftrightarrow \exists i \in \{1, \dots, n\}, (\forall j < i, v_j = v'_j) \wedge (v_i < v'_i) \quad (18)$$

Definim astfel *pseudo-erodarea* ca fiind minimul, în sens lexicografic:

$$[\varepsilon_g(f)](k) = \min_\ell \{\mathbf{e}_a, \mathbf{e}_b\} \quad \forall k \in \mathcal{D}_f \quad (19)$$

iar *pseudo-dilatarea* ca fiind maximul lexicografic:

$$[\delta_g(f)](k) = \max_\ell \{\mathbf{e}_a, \mathbf{e}_b\} \quad \forall k \in \mathcal{D}_f \quad (20)$$

Pentru imagini multispectrale $f : \mathcal{D}_f \rightarrow \mathbb{R}^n$, folosim aceeași definiție a pseudo-extremelor, dar distanța utilizată este cea euclidiană în spațiul \mathbb{R}^n , iar etichetarea este realizată pe baza unei pre-ordini a energiei pixelilor (ordonarea lexicografică neavând sens):

$$\forall \mathbf{v}, \mathbf{v}' \in \mathbb{R}^n, \mathbf{v} <_e \mathbf{v}' \Leftrightarrow \sum_{i=1}^n v_i^2 < \sum_{i=1}^n v'_i{}^2 \quad (21)$$

Figura 10 prezintă rezultatele aplicării operatorului de pseudo-dilatate morfologică bazat pe calculul distanței maxime pentru diverse dimensiuni ale elementului structurant pentru o imagine (Pompoms) din baza de date CAVE¹³, Columbia University, New York.

¹²R. Coliban, M. Ivanovici, Color and Multispectral Texture Characterization Using Pseudo-Morphological Tools, IEEE International Conference on Image Processing (ICIP), Paris, France, October 27-30, 2014, <http://dx.doi.org/10.1109/ICIP.2014.7025126>

¹³<http://www.cs.columbia.edu/CAVE/databases/multispectral/>



Fig. 10: Pseudo-dilatări ale imaginii Pompons pentru diverse dimensiuni ale elementului structurant: 3×3 , 5×5 , 7×7 , 9×9 .

Ca aplicație directă pentru analiza texturilor, pentru imaginea Pompons din baza CAVE am calculat și reprezentat grafic funcțiile de granulometrie și covarianță morfologică pentru domeniul multispectral, conform definițiilor din Capitolului 4 al tezei de față (Figura 11) și le-am comparat cu variantele lor pentru imagini color și în nivele de gri: comportamentul tuturor celor trei curbe este unul foarte asemănător, dovedind validitatea extinderii operatorilor la domeniul multispectral.

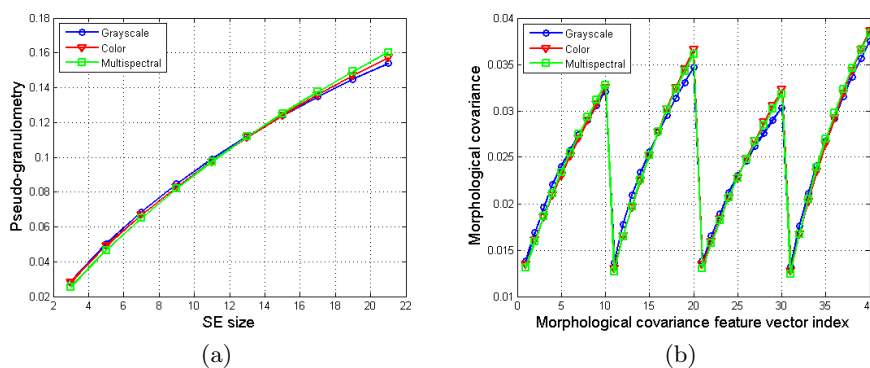


Fig. 11: Pseudo-granulometria și covarianța morfologică bazate pe distanța maximă.

Aplicații

În continuare ne vom concentra pe o aplicație majoră, și anume segmentarea imaginilor, inclusiv pe baza clasificării texturilor. Conceptele teoretice ale segmentării imaginii sunt prezentate în lucrări precum [66] și [46]. În acest rezumat sunt succint prezentate câteva tehnici de segmentare, prezentate pe larg, alături de alte tehnici, în capitolul *Color Image Segmentation*¹⁴ apărut la editura Springer.

¹⁴M. Ivanovici, N. Richard, D. Paulus, *Color Image Segmentation*, in *Advanced Color Image Processing and Analysis*, ed. Christine Fernandez-Maloigne, Springer New York, 2013, ISBN 978-1-4419-6190-7, <http://www.springer.com/us/book/9781441961891>

Segmentarea *watershed*

Tehnica de segmentare watershed este o abordare bazată pe regiuni, în care imaginea este modelată ca un relief [13] [103]. Este abordarea fundamental legată de morfologia matematică. Procesul de segmentare este inspirat din fenomene naturale (i.e. precipitații) - prin inundarea văilor reliefului imaginii se vor forma bazine, iar liniile de demarcație dintre acestea vor constitui frontierele segmentelor hărții de segmentare [14]. Când relieful este complet inundat, rețeaua de baraje *watershed* reprezintă harta de segmentare. În Figura 12 este ilustrat procesul de segmentare: a) bazinele încep să se inunde, iar bazinele V_1 și V_3 inundă două minime locale; b) un baraj este construit între văile V_1 și V_2 și un altul între V_2 și V_3 .

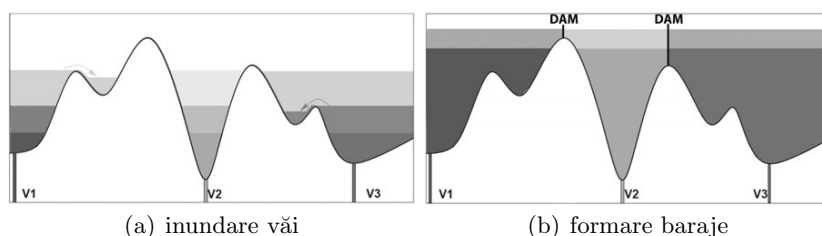


Fig. 12: Ilustrarea tehnicii de segmentare watershed.

Tradițional, segmentarea watershed are loc în domeniul original al imaginii, dar există abordări cum ar fi [131] în care segmentarea se realizează într-un spațiu al trăsăturilor. În Figura 13 este prezentat un exemplu de segmentare utilizând tehnica watershed, cu o fereastră locală de dimensiune 21×21 . De regulă, poate urma o fază de fuziune a regiunilor care rezultă în cazul unei suprasedgmentări.

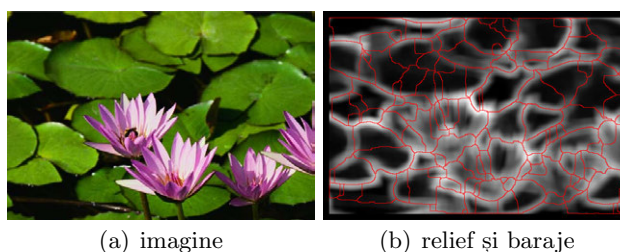


Fig. 13: Exemplu segmentare watershed.

Chanussot et al. a extins tehnica de segmentare watershed la domeniul color utilizând o tehnică bit mixing pentru morfologie vectorială [22].

Contururile active

Contururile active au fost introduse de Terzopoulos et al. în 1988 [69] și sunt utilizate cu succes în segmentarea imaginilor. Sunt definite ca funcții *spline*

de energie minimă ghidate de forțe externe influențate de conținutul imaginii astfel încât funcțiile vor converge ca poziție către trăsături ale imaginii cum ar fi frontierele.

Conturul inițial este deformat iterativ în funcție de câteva energii specificate. Conform definiției originale, un contur activ este o curbă spline $c(s) = [x(s), y(s)]$, cu $s \in [0, 1]$, care minimizează următoarea funcțională energetică [116]:

$$\varepsilon(c) = \varepsilon_{\text{int}}(c) + \varepsilon_{\text{ext}}(c) = \int_0^1 [E_{\text{int}}(c(s)) + E_{\text{ext}}(c(s))] ds \quad (22)$$

unde $\varepsilon_{\text{int}}(c)$ reprezintă energia *internă*, intrinsecă curbei, iar $\varepsilon_{\text{ext}}(c)$ energia *externă*, calculată pe baza imaginii. Energia internă ε_{int} este de regulă:

$$\varepsilon_{\text{int}}(c) = \int_0^1 \frac{1}{2} [\alpha(s) |c'(s)|^2 + \beta(s) |c''(s)|^2] ds \quad (23)$$

unde $c'(s)$ și $c''(s)$ sunt prima și a doua derivată, ponderate cu $\alpha(s)$ și $\beta(s)$, care sunt de regulă constante în cele mai multe implementări de contururi active.

Energia externă este dată de un anumit model de difuzie, calculat pe imaginea de segmentat. Pentru extinderea la domeniul color, am utilizat momentul de ordin întâi al integralei de corelație pentru a defini un model de difuzie pentru imagini color [64]. În Figura 14 sunt prezentate rezultatele abordării noastre multi-rezoluție. Ipoteza de lucru pe care o facem este aceea că în imagine sunt prezente două tipuri de texturi, prezentând complexități diferite: una corespunzătoare obiectelor de interes și alta fundalului (complexitatea acestuia din urma fiind de regulă mai mică).

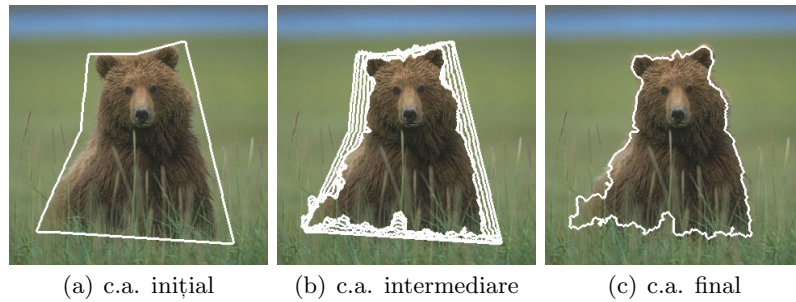


Fig. 14: Exemplu de segmentare utilizând contururi active (c.a.) pe o imagine color din baza Berkely (100080).

În cadrul abordării noastre, energia externă este intim legată de dimensiunea de corelație, fiind practic valoarea medie a distribuției $C(\delta)$, și reprezintă o măsură a eterogenității texturii locale, într-o anumită vecinătate,

la o anumită rezoluție¹⁵. Concret, forțele energiei externe care conduc conturul activ sunt date de media distanțelor ΔE din spațiul de culoare CIE Lab calculate la diverse rezoluții ale imaginii (Figura 15). Pentru o anumită rezoluție, valoarea în punctul (x, y) a suprafeței energetice este dată de media celor $n^2(n^2 - 1)/2$ distanțe dintr-o vecinătate de dimensiune $n \times n$ centrată în punctul respectiv:

$$E_{\text{ext}}(x, y)|_{n \times n} = \frac{2}{n^2(n^2 - 1)} \sum_{i=1}^{n^2} \sum_{j=i+1}^{n^2} \Delta E(v_i, v_j) \quad (24)$$

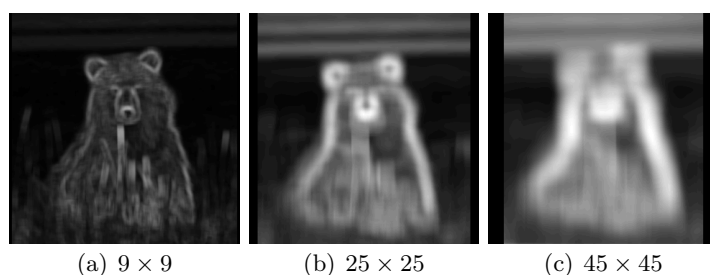


Fig. 15: Pseudo-imagini de difuzie pentru imaginea Berkely 100080.

Segmentarea bazată de trăsături texturale

Deseori segmentarea este realizată într-un spațiu al trăsăturilor, nu direct pe valorile pixelilor din imagine. De obicei, o tehnică de clasificare (e.g. k -means) este utilizată pentru a clasifica pixelii în funcție de trăsăturile lor locale, calculate pentru o anumită vecinătate în jurul pixelului considerat. În Figura 16 sunt prezentate rezultatele segmentării utilizând trăsăturile morfologice prezentate în Capitolul 4: granulometria și covarianța morfologică. Clasificarea utilizată a fost una nesupervizată, k -means pentru $k = 2$ pe baza ipotezei că în imagine sunt prezente doar două texturi: una corespunzătoare obiectului de interes și alta fundalului.

Pentru a ilustra tehnica de segmentare pentru imagini color, am folosit ca trăsătură locală vectorul de volume calculate într pseudo-dilatări și pseudo-erodări, pentru diverse dimensiuni ale elementului structurant. Cele două operații pseudo-morfologice probabilistice (PPM) sunt prezentate în Capitolul 4. Sunt comparate rezultatele obținute folosind pseudo-morfologia α -trimmed (calculată în spațiul RGB) și morfologia bazată pe ordonare lexicografică (în spațiu HSV, cu prioritatea componentelor V, S, H). Am calculat vectorii de volum local, folosind o fereastră glisantă, apoi o clasificare

¹⁵M. Ivanovici, D. Stoica, Color diffusion model for active contours - an application to skin lesion segmentation, Annual International Conference of the IEEE, Engineering in Medicine and Biology Society (EMBC), 2012, <http://dx.doi.org/10.1109/EMBC.2012.6347202>

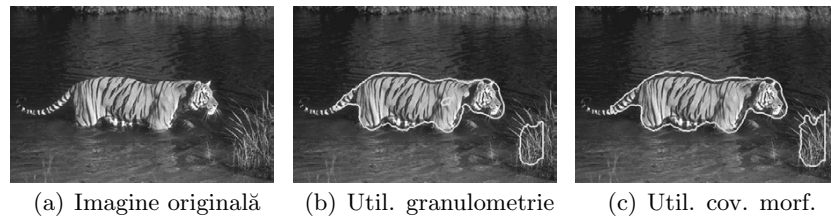


Fig. 16: Exemplu de segmentare bazată pe trăsături texturale.

k -means în două clase. Am realizat și o segmentare manuală, ideală, utilizată drept referință pentru calculul procentului de pixeli corect clasificați. Rezultatele sunt prezentate în Figura 17.

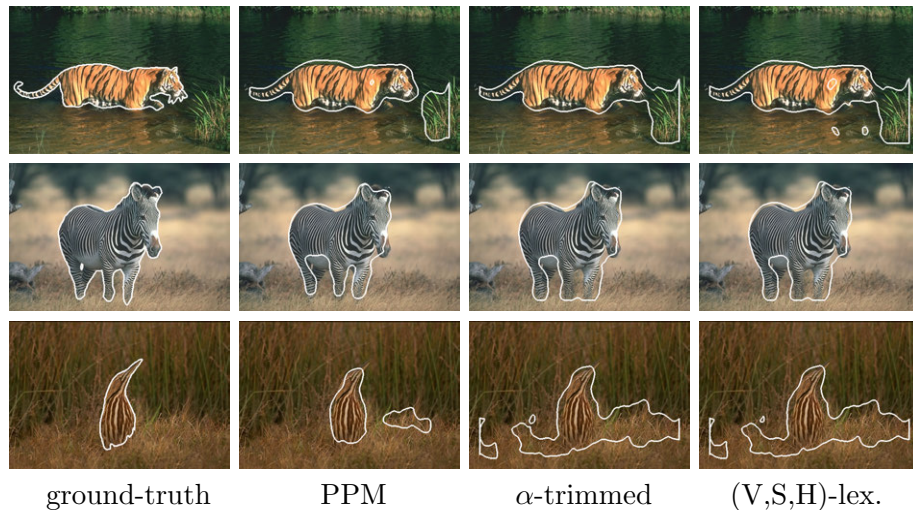


Fig. 17: Rezultatele segmentării bazate pe trăsături texturale color.

Din punct de vedere cantitativ, am calculat procentul de pixeli corect clasificați ca un criteriu de evaluare a calității segmentării [21]. Rezultatele sunt prezentate în tabelul următor. În experimentele noastre, în cele mai multe din cazuri, abordarea PPM conduce la o segmentare mai bună, dată fiind capacitatea mai bună de a evalua corect complexitatea texturii și variația acesteia la diverse scale de analiză.

	PPM	α -trimmed	(V,S,H) lex.
Berkeley108073	92.37%	91.41%	90.57%
Berkeley130066	96.06%	95.37%	95.40%
Berkeley43033	96.35%	86.01%	86.19%

În loc de încheiere

Procesul de segmentare necesită adresarea și soluționarea următoarelor trei probleme: (i) determinarea trăsăturilor capabile să caracterizeze corect omogenitatea regiunilor imaginii; (ii) măsurile de similaritate sau funcțiile de distanță utilizate pentru trăsături și (iii) abordarea cadru de segmentare care optimizează harta de segmentare ca o funcție de perechea trăsăturimetrici. Am prezentat separat câteva tehnici de segmentare, dar de regulă există o graniță foarte fină între acestea și deseori sunt preferate abordări hibride care combină de exemplu piramidele și watershed [2]. Totuși, tehnicile de segmentare au evoluat către câteva tehnici cadru unanim acceptate: abordări piramidale, watershed, JSEG, tăieturi în graf, contururi active sau, recent, TurboPixels.

Întrebarea lui Haralick persistă însă și astăzi: care este valoarea optimă pentru criteriul de omogenitate ales? Nu există rețete prestabilite. Noi perspective apar dinspre teoria percepției, în special a teoriei Gestalt. Deoarece definiția omogenității, respectiv a eterogenității, trebuie exprimată drept complexitatea unei trăsături sau a distribuției acesteia, teoriile perceptuale caută să explice care sunt parametrii fizici luați în considerare de către sistemul vizual uman. O problemă deschisă este dată deci de relația dintre legea similarității Gestalt și omogenitate. Randal [100] face legătura dintre legea de similaritate și gruparea în regiuni omogene de culoare sau textură. Definiția omogenității și implicit a complexității unei texturi rămâne însă imperfectă și reprezintă în continuare o nișă de viitor în cercetare.

Part II

Scientific and professional achievements and the evolution and development plans for career development

Subpart II.1

Scientific and professional achievements

Chapter 1

Color and multispectral texture images

Texture represents the variation of the signal or image data at scales smaller than the scale of interest, according to [96]. Textures can be regular, semi-regular and irregular (see Figure 1.1). In other words, they can be deterministic or stochastic. In the regular ones, a texture element called *texel* repeats itself periodically, forming a deterministic structure. The irregular textures do not possess such an element, they are composed of random variations of the signal. The intermediate class of semi-regular textures can be described by texels which have random location or size. Most natural textures are irregular. For the stochastic textures the presence of visible and well-identified texels lacks, but certain statistical features (e.g. statistical moments) remain constant or invariant, consequently some authors consider textures as being stationary random fields.



Fig. 1.1: Types of textures.

The notion of texture emerged in the 60-70s in the context of analysis of gray-scale images that present certain variations at object surface that rendered difficult the task of image segmentation. According to Haralick [53], human beings use three types of features for interpreting color images: spectral, textural and contextual features. The texture features contain

information about the spatial arrangement of pixel values. Texture can be described using terms like fine, coarse or smooth, rippled, mottled, irregular or lineated [53]. Most of the features focus on only one aspect of gray scale texture images, like contrast or coarseness. Color information or color features are sometimes concatenated with texture features for the purpose of classification, in order to boost the correct classification rate.

Haralick introduced in [53] the gray-tone spatial-dependence matrices, also known as gray-level cooccurrence matrices, as a way to characterize texture. Based on these matrices he proposed 14 texture features regarding homogeneity, contrast, number and nature of boundaries, and the complexity of image. Various texture characterization have been proposed since then and in [117] the existing techniques were classified as being: geometrical, statistical, image model-based methods and signal processing approaches. The geometrical methods aim at describing the regular and semi-regular textures by the shape and position or the texels [96], thus being based on detection of the texture elements and the recovering of their spatial distribution. The statistical approaches are usually based on second-order statistics or the auto-correlation function [53]; these are suited for the analysis of irregular textures as well. The model-based methods use a mathematical model to describe the analyzed image like fractals [93] or Markov random fields [33], which can also be used for synthesizing the texture images. The signal processing approaches include the usage of filters to extract information from textures, e.g. Gabor filters [65], Laws filters [72], or non-linear filters from mathematical morphology [114].

In this book we dedicate our attention to the notion of complexity, in the context of texture image analysis. The etymology of the word itself, from the Latin word *complex* meaning “twisted together” designating a system composed of closely-connected components, indicates that the complexity integrates or should be able to integrate various aspects of the under-study object - the texture in our case. There exist various definitions of complexity, including Kolmogorov complexity and entropy. Recently, N. Richard and myself proposed a new Technical Committee within Division 8 of CIE entitled *Specification of Spatio-Chromatic Complexity* and it was approved as TC 8-14. Its objective is to produce a single definition of spatio-chromatic complexity embedding the spatial and chromatic variations in a generic and vector form, based on the existing definitions of the complexity and the integration of various aspects of non-uniform surfaces, generally denoted as textures. Following this line of thought, in this book we focus on a fractal point of view to texture analysis (see the following two chapters). Together with such an integrative approach and point of view, we stress out the importance of vector processing, as opposed to marginal analysis.

Various texture image databases have been constructed for the purpose of testing translation, rotation, scale and illuminant-invariant feature extraction or classification approaches. Two of the most used and well-known

texture image data-bases are Outex [89] and VisTex¹. A subset of the VisTex data-base is presented in Figure 1.2.



Fig. 1.2: Various color textures from the VisTex data base.

Color images are vector images, usually represented using the RGB color space used for image acquisition. The information represent lambdas in the visible spectrum (roughly from 380 nm to 700 nm). There are several elements of particular interest when we take color into consideration for the analysis of texture images: metamers, human perception... Color can be treated independently of the texture information, see for instances approaches where the color features were concatenated with texture features for the purpose of improving the classification task, of treated vectorial (see full-band or vector processing). Recently, there is a high interest in multispectral and hyperspectral imaging techniques.

The multispectral imaging refers to the techniques used for image data acquisition at various wavelengths across the electromagnetic spectrum, including those beyond the visible range. The result is an n-dimensional or multivariate image that reveals additional information compared to visible-spectrum images. The multispectral images are an invaluable source of information in a wide range of domains, especially for agriculture, since they allow to emphasize or assess various aspects such as vegetation status, soil humidity, etc. Starting with the first Landsat satellite system, there is a clear trend in equipping satellites with multispectral instruments.

See for instance in Figure 1.3 several bands of a multispectral image from the CAVE² data-base, Columbia University, New York. The multispectral images from this data-base have 31 bands, from 400 nm to 700 nm, in steps of

¹<http://vismod.media.mit.edu/vismod/imagery/VisionTexture/>

²<http://www.cs.columbia.edu/CAVE/databases/multispectral/>

10 nm. The RGB image is rendered based on the multispectral information.

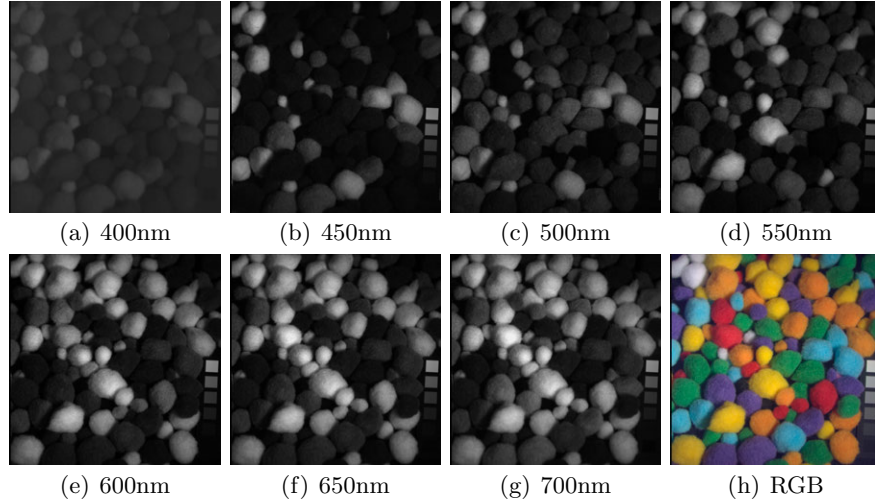


Fig. 1.3: Various lambdas and the RGB *pompoms* image from CAVE database.

Take for instance the four color points in the Pompoms image in Figure 1.3. The corresponding spectral signatures are depicted in Figure 1.4.

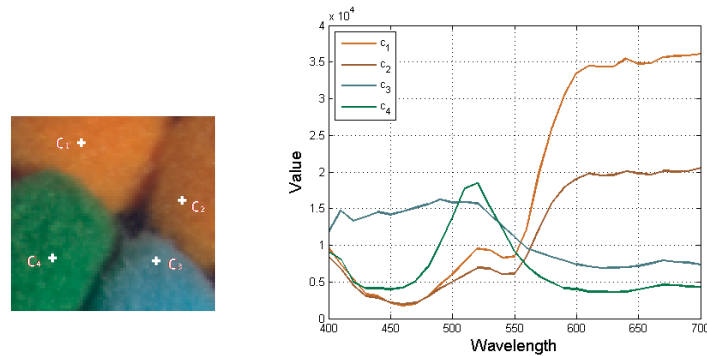


Fig. 1.4: Crop of the Pompoms image and the multispectral signatures of the four highlighted pixels.

Apart from CAV, several open-access multispectral image data-bases of multispectral images are available from University of East Anglia, United Kingdom³, Brno University of Technology, Czech Republic⁴ or the Joint Research Center, the Institute for Environment and Sustainability⁵. The

³<http://www2.cmp.uea.ac.uk/Research/compvis/MultiSpectralDB.htm>

⁴<http://splab.cz/en/download/databaze/multispec>

⁵<http://image2000.jrc.ec.europa.eu/DI/IM.htm>

latter one called IMAGE2000 contains satellite images Europe produced by the instrument on Landsat 7.

We would like to emphasize the fact that multivariate or n-dimensional models obtained by a generalization of the ones existing for gray scale images do not always perfectly suit color or multispectral information: n-dimensional Euclidian spaces may not be used, because of the high correlation between various bands of the color or multispectral images. Take for instance the example in Figure 1.5 - a natural color texture representing a sugar beet crop.

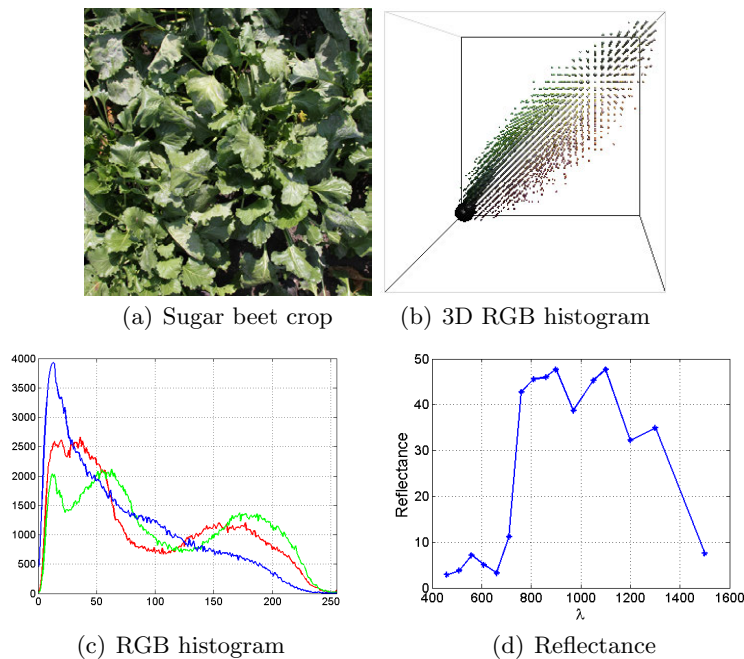


Fig. 1.5: Sugar beet texture image example.

The sugar beet example shows that there is high reflectance in the IR and NIR domain, the spectral signature being characteristic for vegetation. In Chapter 2 in a first approach we make the assumption that there is independence between the color components of the generated synthetic color texture, but this is clearly false for natural ones. However, the hypothesis of independence between color components or spectral bands helped us to generate highly complex textures that can be used as references for validation and calibration of various complexity estimation methods or features. In order to model natural texture images this hypothesis has to be adapted, so that a certain correlation is introduced between various spectral bands.

Chapter 2

Fractal models

Within the context of Euclidian geometry, objects (i.e. geometrical figures) are completely described by formulae and have a characteristic size or scale. Unfortunately, Euclidian geometry cannot model natural complex shapes. Fractal geometry was introduced by B. Mandelbrot in 1983 [79] in order to describe self-similar sets called fractals. In fractal geometry the objects are usually generated by a recursive algorithm and they cannot be described by one formula, and in addition do not have a specific size or scale. Fractal models proved to be of great importance and usefulness for computer graphics and digital image processing and analysis. However, all the existing approaches for fractal image analysis are defined for one dimensional signals or binary images, with extension to gray-scale images. In order to develop and validate new tools for color image analysis, it would be very useful to have synthetic color fractal images with known properties.

Fractal objects are self-similar and independent of scale. *Self similarity* is a central concept of the fractal geometry, being closely connected to the notion of dimension and implicitly to complexity. The fractal or similarity dimension is a quantitative measure of the *wiggleness* of a fractal object [93]. The irregularities of a fractal object determine a fractal dimension comprised in the interval $[E, E + 1]$, where E is the topological dimension of the object. The fractal dimension will be discussed in detail in Chapter 3. Fractals can be classified in two major categories: (i) *deterministic fractals*, which are composed of several scaled down and rotated copies of themselves (e.g. von Koch snowflakes, Sierpinski gaskets and Julia sets); and (ii) *random fractals*, for which an additional randomness is included and they are used to simulate natural phenomena. In this chapter we focus on various models of random fractals, which are of particular interest for the texture image analysis domain.

Fractal models are used for the generation of synthetic textures, shapes and landscapes in computer graphics or to model natural phenomena. Fractals are usually represented as black and white binary images, like gray-scale

images or pseudo-colored images. For the uniform fractals (also called *pure* fractals), the fractal dimension can be computed in a precise manner. The non-uniform random fractals are usually represented as 2D surfaces or gray-level images and the fractal dimension is estimated based on a distribution of increments. For the generation of fractal sets there exist several approaches. From the plethora of algorithms we embraced the one of random fractal generation, mainly Brownian fractional noise generation.

Random fractals can be modeled as Brownian noise or motion. By definition, Brownian motion is the integral of a Gaussian white noise $w(t)$:

$$v_B(t) = \int_{-\infty}^t w(s) ds \quad (2.1)$$

There are mainly three approaches for the generation of fractional Brownian motion: (i) random midpoint displacement—a recursive generating technique applied by N. Wiener in the 1920s; (ii) the Fourier Transform filtering approach and (iii) the random cut method. All these techniques are fully described in [93]. In this chapter we focus on the random midpoint displacement algorithm and its extension to the color image domain.

2.1 Midpoint displacement algorithm

The technique called *displacing interpolated points* of generating fractional Brownian motion was proposed by Saupe in [93] and it represents a generalization of the random midpoint displacement method, introduced by Fournier *et al* [42]. In the 1-dimensional case, a signal $X(t)$ is a fractional Brownian motion function if the increments $X(t_1) - X(t_2)$ represent Gaussian zero-mean random variables and the variance of the increments is directly proportional to the $|t_1 - t_2|$ distance:

$$\overline{|X(t_2) - X(t_1)|^2} \propto |t_2 - t_1|^{2H} \quad (2.2)$$

where $H \in [0, 1]$ is the Hurst coefficient controlling the complexity of the fractal being generated. The parameter H characterizes the scaling behavior and it's in the range $0 < H < 1$: a value close to 0 indicates a rough structure, while a value close to 1 indicates a smooth one [93]. The relationship between the fractal dimension D , the dimension of the space E and the parameter H is the following: $D = E + 1 - H$.

The idea of the random midpoint displacement algorithm is to construct the increments in an recursive process, such as the increment is reduced by a factor 2 at each level. In the algorithm described by Saupe, the signal is generated starting from $X(0) = 0$ and selecting $X(1)$ as a sample of a Gaussian random variable with mean 0 and variance σ^2 . Thus, the values

of the signal are generated in the $[0, 1]$ interval and they have to meet the condition:

$$\overline{|X(t_2) - X(t_1)|^2} = |t_2 - t_1|^{2H} \sigma^2, \quad \forall 0 \leq t_1 \leq t_2 \leq 1 \quad (2.3)$$

which is a particularization of (2.2). The name of midpoint displacement comes from the fact that at every iteration step a point is generated for every pair of existent consecutive points in the function, in the middle of the interval determined by them. Thus, at the first step, one point is generated at $t = \frac{1}{2}$, at the second step, two points are generated at $t = \frac{1}{4}$ and $t = \frac{3}{4}$ and so on (see Figure 2.1). The points are generated as the average of the generating points plus a sample of a Gaussian random variable D_i with mean zero and variance Δ_i^2 , where i is the iteration number.

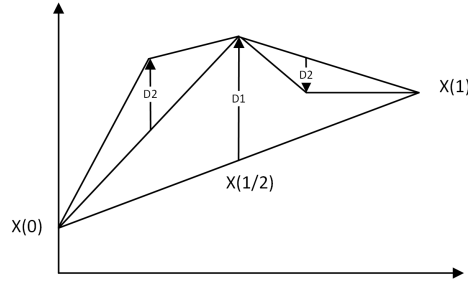


Fig. 2.1: Midpoint displacement algorithm illustration.

In the first iteration step, we have:

$$X\left(\frac{1}{2}\right) = \frac{1}{2}(X(0) + X(1)) + D_1 \quad (2.4)$$

where D_1 is a zero mean Gaussian random variable with variance Δ_1^2 . In order to compute Δ_1^2 , we use the equation (2.3):

$$\overline{\left|X\left(\frac{1}{2}\right) - X(0)\right|^2} = \left(\frac{1}{2}\right)^{2H} \sigma^2 \quad (2.5)$$

But

$$\begin{aligned} \overline{\left|X\left(\frac{1}{2}\right) - X(0)\right|^2} &= \overline{\left|\frac{1}{2}(X(1) - X(0)) + D_1\right|^2} \\ &= \frac{1}{4} \overline{|X(1) - X(0)|^2} + \overline{|D_1|^2} \\ &= \frac{1}{4} \sigma^2 + \Delta_1^2 \end{aligned}$$

because $X(1) - X(0)$ and D_1 are uncorrelated. Consequently,

$$\Delta_1^2 = \frac{\sigma^2}{2^{2H}} (1 - 2^{2H-2}) \quad (2.6)$$

In the second iteration step we obtain a random variable D_2 with the variance:

$$\Delta_2^2 = \frac{\sigma^2}{4^{2H}} (1 - 2^{2H-2}) \quad (2.7)$$

and as a general relation, we obtain:

$$\Delta_n^2 = \frac{\sigma^2}{(2^n)^{2H}} (1 - 2^{2H-2}) \quad (2.8)$$

The algorithm can be easily extended to higher dimensional signal generation, for $X(\mathbf{p})$ -type functions, where \mathbf{p} is an n -dimensional vector, by changing the domain of the X function and the interpolation operations from \mathbb{R} to \mathbb{R}^n . However, for a digital synthetic image generation, the domain is \mathbb{Z}^2 , and the co-domain consists of a bounded integer points set, so the normalization of the generated values and the integer quantization steps have to be taken into consideration in the fractal dimension estimation.

In the case of images, we start with the corners (marked with circles in Figure 2.2 left), then we compute the central pixel (marker with a square), then we continue with the points marked with triangles and iteratively or recursively as indicated in Figure 2.2 right until all pixel values are computed.

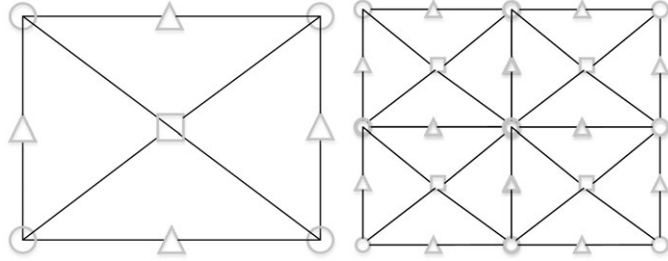


Fig. 2.2: 2D midpoint displacement algorithm illustration.

To control the texture complexity along the scale, the variance σ_i^2 of the increments must be proportional to $(r^n)^{2H}$ for a Gaussian random variable—the luminance in the case of a gray scale image [93]:

$$\sigma_i^2 = \overline{|X(t_1, t_2) - X(s_1, s_2)|^2} \propto \left(\sum_{i=1}^2 (t_i - s_i)^2 \right)^H \quad (2.9)$$

where $X(s_i, t_i)$ denotes a random process, a function of two spatial coordinates, s_i and t_i . For a gray scale image, $X(s_i, t_i)$ is the value of the luminance of each pixel of the image, while for a color image is the color of the pixel, thus a vectorial value.

2.2 Extension to color

A color image does not represent a 5D Euclidian form, as a pure or deterministic fractal with known properties does. In order to design a color fractal image generator, we extended in [63] the random midpoint displacement method from gray-scale [93] to color domain. We chose to work in the RGB color space because it exhibits a cubic organization coherent with the construction of the fractal object. In this way, we could reach the constraint of the expression in a five-dimensional Euclidian space. However, any other color space obtained through linear transformations could be used, and we also generated color fractal images using the HSV color space.

In the case of an RGB color image, the increments are differences between two 3D vectors, in the sense of the Euclidian distance. The variance of these increments is:

$$\sigma_i^2 = \overline{\left(\sqrt{\sum_{k=r,g,b} (X_k(t_1, t_2) - X_k(s_1, s_2))^2} \right)^2} \quad (2.10)$$

$$\sigma_i^2 = \frac{[X_r(t_1, t_2) - X_r(s_1, s_2)]^2 + [X_g(t_1, t_2) - X_g(s_1, s_2)]^2 + \dots}{\dots + [X_b(t_1, t_2) - X_b(s_1, s_2)]^2} \quad (2.11)$$

In the hypothesis that the increments in the three RGB planes are statistically independent, i.e. the color stimuli on the three channels are not correlated, we can distribute the statistical operation to each term:

$$\sigma_i^2 = \overline{[X_r(t_1, t_2) - X_r(s_1, s_2)]^2} + \overline{[X_g(t_1, t_2) - X_g(s_1, s_2)]^2} + \overline{[X_b(t_1, t_2) - X_b(s_1, s_2)]^2} \quad (2.12)$$

Because every of the three terms is proportional to $\left(\sum_{i=1}^2 (t_i - s_i)^2 \right)^H$, we can conclude that the sum will be also proportional to the space coordinate differences:

$$\sigma_i^2 \propto 3 \cdot \left(\sum_{i=1}^2 (t_i - s_i)^2 \right)^H \propto \left(\sum_{i=1}^2 (t_i - s_i)^2 \right)^H \quad \square \quad (2.13)$$

We therefore demonstrated that formula (2.9) stands for the color fractal images we generated using the RGB color space. The same conclusion holds in the case of the HSV color space, even if the transformation from the generation color space (HSV) to the image representation color space (RGB) might change the above statement.

For the implementation of the generation approach, we modified the algorithm presented in [93] in order to work with RGB and HSV triplets and we present here only the lines that differ from the original algorithm. In the initialization phase, we generate four RGB, or HSV, triplets for the corners of the color fractal image. All the functions were modified in order to work with three-dimensional vectors instead of scalar values.

In Figures 2.3 and 2.4 we show the color fractal images obtained by using the two versions of our generator. The complexity differs, as the Hurst factor is comprised between 0.1 and 0.9. The size of the images is 256 pixels, in order to deal with a five-dimensional Euclidian space that has the same dynamic range on all of its axes.

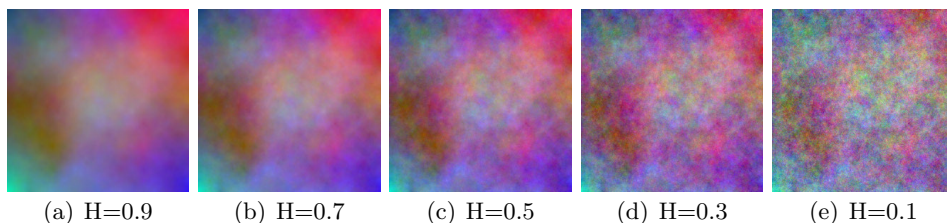


Fig. 2.3: Color fractal images generated in RGB.

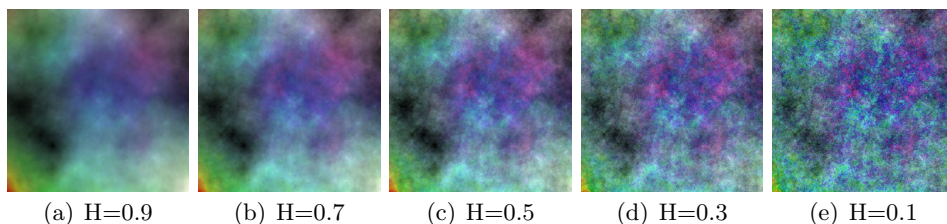


Fig. 2.4: Color fractal images generated in HSV.

In order to assess the performance of our generator, we analyze the spread of the vectors representing the colors in the RGB cube and implicitly the complexity of the generated fractal forms. We do this by (i) visually inspecting the 3D histograms of the color fractal images; (ii) by quantifying the variance of the co-occurrence matrices and (iii) by calculating the 3D histograms of the neighbor 3D increments. See [63] for more details.

For the color fractal images, both generated in RGB and HSV, we computed the 3D histograms, depicted in Figures 2.5 and 2.6. The diameter of each sphere is proportional to the number of pixels with the same color as the color of the sphere. The histograms are not able to completely characterize the fractal images, but they indicate in an intuitive way how much of the RGB space cube is occupied. One can see that for large values of H the histograms are coarse and not too spread, both for the RGB and HSV generated images. For small values the histogram tends to have the shape of a compact sphere in the case of RGB-generated images, and a compact

cone for the HSV-generated images. In both cases one can see that the RGB space is better filled: the larger the occupation of the RGB space, the higher the fractal dimension. The former histograms also show the limitations of the generator, which is not capable of filling the whole RGB space because, among various reasons, of the Gaussian distribution of the increments.

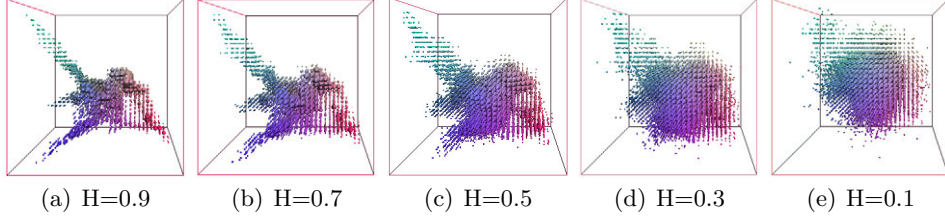


Fig. 2.5: 3D histograms for the color fractal images generated in RGB.

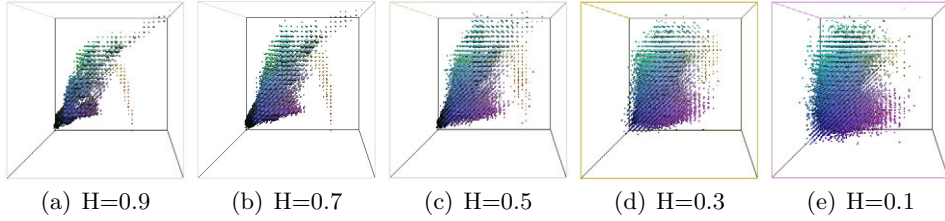


Fig. 2.6: 3D histograms for the color fractal images generated in HSV.

The co-occurrence matrices are used to characterize textures by computing the probability $\chi_{c_i, c_j}^{(d, \theta)}$ that a pixel p_1 of color c_i has a neighbor p_2 of color c_j , the position of the neighbor being defined by the distance d and the direction θ :

$$\chi_{c_i, c_j}^{(d, \theta)} \triangleq P [p_1 \in \mathbf{A}_{c_i}, p_2 \in \mathbf{A}_{c_j} / |p_1 - p_2| = d, (p_1, p_2) = \theta] \quad (2.14)$$

We computed the co-occurrence matrices for a neighborhood distance of one pixel for the horizontal direction¹. Our purpose is to analyze the repartition of the color increments for the RGB triplets. Theoretically, the co-occurrence matrices for a color image would require a 6-dimensional hyper-cube, and will be very difficult to depict. But in our case, as the color increments are uncorrelated between them, we could reduce the computation to the co-occurrence matrix on each color plane of the RGB space.

As a measure of variance, we plot in Figure 2.7 the exterior contour of the shape represented by the co-occurrence matrix for one component of the RGB space, for various H values between 0.1 and 0.9. One can see that for

¹In this case, the definition of the co-occurrence is very closed to the correlation except for the limitation imposed by the analysis of the data in a particular direction, which however greatly reduces the computation time.

the fractal with $H = 0.9$ the co-occurrence matrices exhibit a diagonal shape indicating the small variations between neighbor pixels, while for $H = 0.5$ and $H = 0.1$ the spread indicates a larger variation. The samples set shape in each plane is clearly a bi-dimensional Gaussian and, as expected, the width of this samples set distribution is proportional to the Hurst exponent, which proves the validity of the generator. The larger variance of the 2D Gaussians in the case of HSV generated images indicates the fact that higher fractal complexity can be achieved than in the case of RGB generated images.

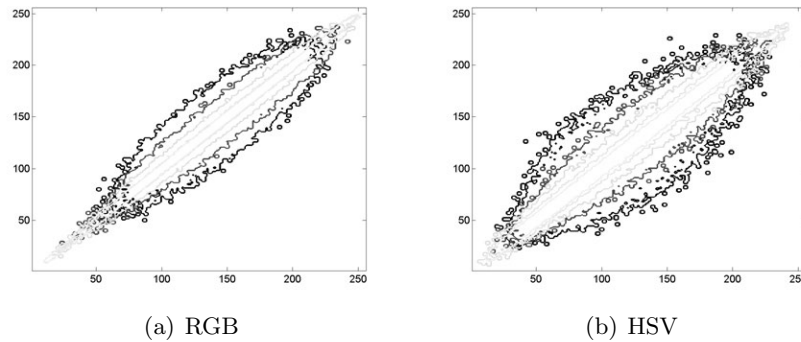


Fig. 2.7: The spread of co-occurrence matrices from $H = 0.1$ (black curve) to $H = 0.9$ (lightest gray curve).

Clearly enough, to write a new fractal estimator is not a great challenge, the more difficult task being to validate the approach on specific objects, for which the theoretical dimension is well known. Unfortunately, a color image does not represent a *standard* five Euclidian form, and a 5-dimensional Brownian fractional noise could not produce a direct stimulus to validate our measure. So to produce a generator not too far from the color texture, we chose to extend the random midpoint displacement method from gray scale [93] to color domain.

2.3 Vector color fractal generator

Our previous attempt for generating color images with fractal properties used the midpoint displacement algorithm to generate three independent random variables, one for each color plane. To go further in our pursuit, for the implementation of the midpoint displacement approach we used a tri-variate normal (Gaussian) generator. This allows us to improve the generation in two ways: (i) the three color components are not independent anymore and (ii) more interestingly, we can control the colors that are generated, by specifying the orientation of the cloud of colors in the 3D histogram. This can be achieved by specifying the covariance matrix Σ , the direction

of the principal axes of the cloud of points are given by the eigenvectors of the covariance matrix.

The probability density of a multi-variate normal distribution is:

$$w(\mathbf{x}) = \frac{1}{(2\pi)^{k/2} |\Sigma|^{1/2}} e^{-\frac{1}{2}(\mathbf{x}-\mu)'\Sigma^{-1}(\mathbf{x}-\mu)} \quad (2.15)$$

where $\mathbf{x} = (x_1, x_2, \dots, x_k)$, $k = \text{rank}(\Sigma)$ is the size of the vector space - 3 in our case for the RGB color space, $|\Sigma|$ is the determinant of the covariance matrix, and $\mu = (\mu_1, \mu_2, \dots, \mu_k)$ is the mean vector of the color set.

The covariance matrix (also called variance-covariance matrix, because of the fact that the values on the diagonal represent variances) we used for the results we present below has the following shape:

$$\Sigma = \begin{pmatrix} 1 & \sigma_{rg} & \sigma_{rb} \\ \sigma_{rg} & 1 & \sigma_{gb} \\ \sigma_{rb} & \sigma_{gb} & 1 \end{pmatrix} \quad (2.16)$$

where $\sigma_{\xi\eta}$ represents the centered moment of the pair (ξ, η) of random variables, i.e. a measure of the correlation between the two variables, where $\xi, \eta = r, g, b$.

Using this approach, now two parameters are available for the control of the multivariate fractal generation: the Hurst factor H , which controls the complexity of the landscape and the covariance matrix Σ , which controls the color content of the generated image.

In the following experiments we used the same correlation between color planes, i.e. the same same sigma values $\sigma = \sigma_{rg} = \sigma_{gb} = \sigma_{rb}$ and we varied the Hurst coefficient (i.e. the H values). For $\Sigma = \mathbf{0}_{3 \times 3}$ the three color planes are completely uncorrelated, but still not independent. Compared to the previous approach, we obtain the following color fractal images depicted in Figure 2.8 along with the corresponding 3D RGB histograms:

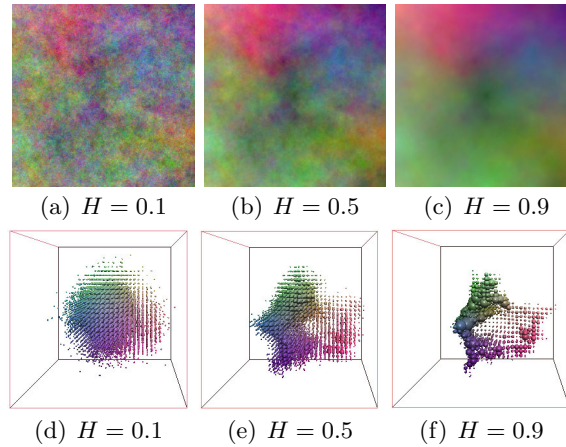


Fig. 2.8: Color fractal images with vector increments with $\Sigma = \mathbf{0}_{3 \times 3}$.

As the correlation between the three color components increases, the cloud of colors will change its shape from a sphere into an ellipsoid, therefore the color will finally turn into gray levels. The landscape remains the same, only the color gamut reduces gradually to the gray-level axis of the RGB cube. This behavior is emphasized for the color fractal images in Figure 2.9 for $H = 0.1$ and the σ varied between 0.1 and 0.9. The corresponding 3D RGB histograms of the images in Figure 2.9 are presented in Figure 2.10. The same behavior can be observed for $H = 0.5$ and $H = 0.9$ in Figure 2.11 and Figure 2.13.

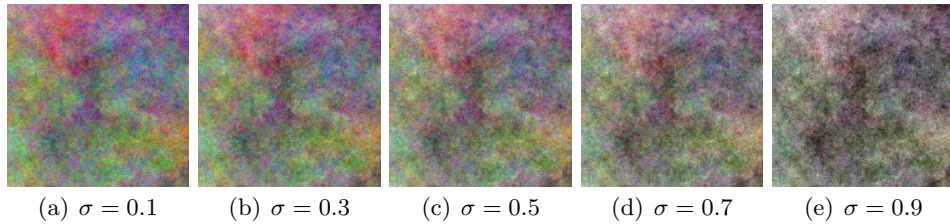


Fig. 2.9: Vector color fractal images with $H = 0.1$.

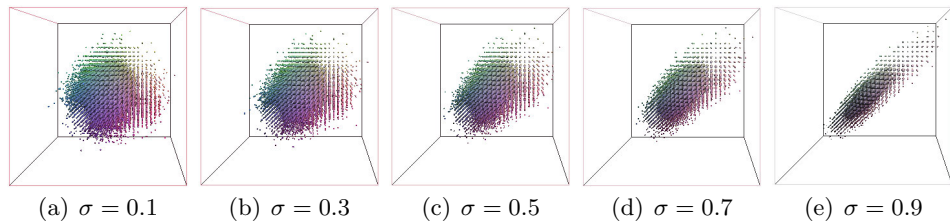


Fig. 2.10: 3D RGB histograms of images in Figure 2.9.

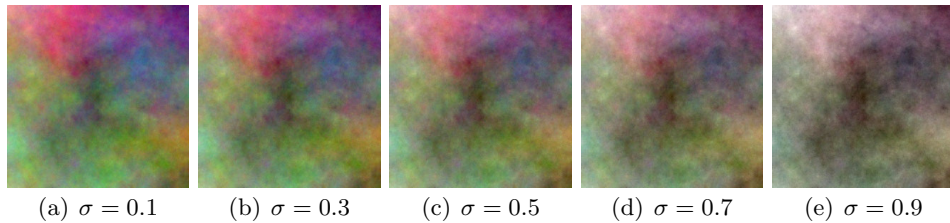


Fig. 2.11: Vector color fractal images with $H = 0.5$.

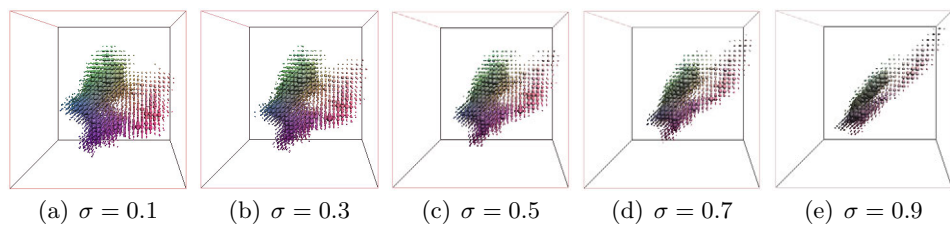


Fig. 2.12: 3D RGB histograms of images in Figure 2.11.

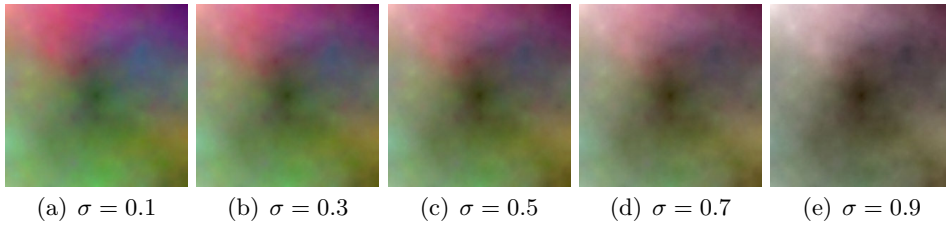


Fig. 2.13: Vector color fractal images with $H = 0.9$.

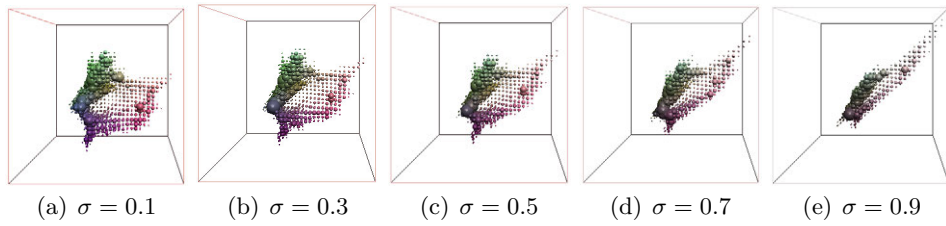


Fig. 2.14: 3D RGB histograms of images in Figure 2.13.

We performed the following comparison: for the same complexity of the landscape (e.g. the Hurst H coefficient) we imposed various correlations between the color components. See the results in Figure 2.15 for $H = 0.9$. The conclusion is the the complexity of the terrain is controlled by H , while the covariance matrix controls the color content of the resulting image.

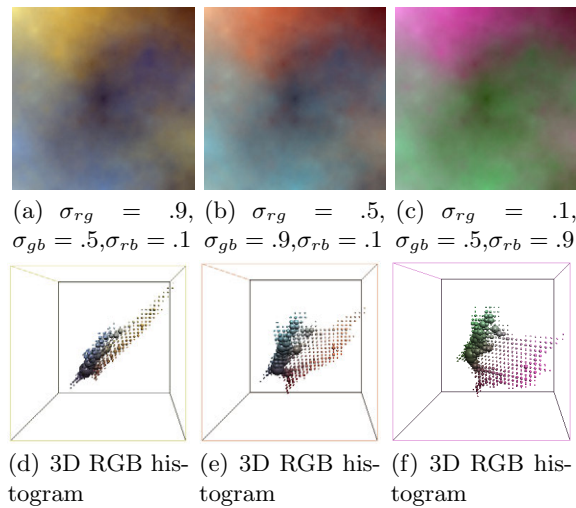


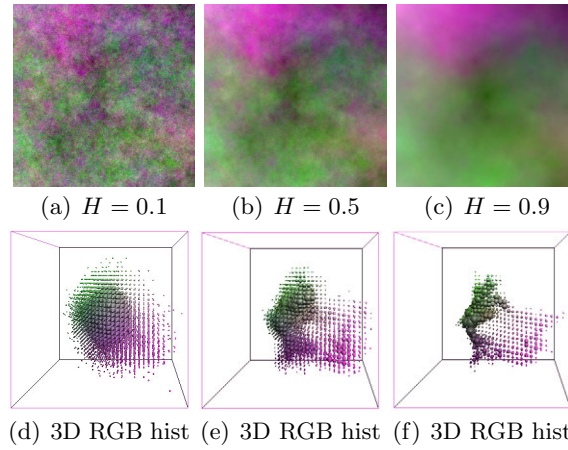
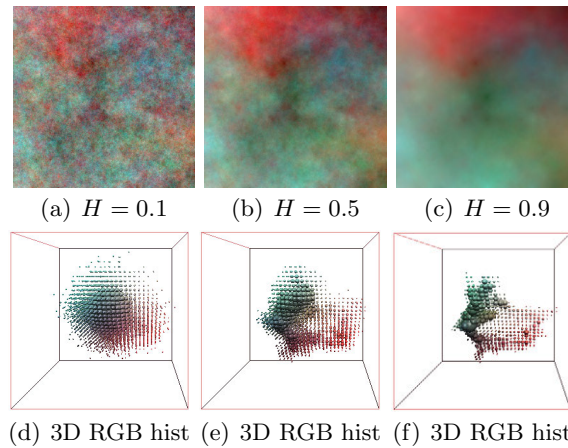
Fig. 2.15: Color fractal images of the same complexity, but different color content.

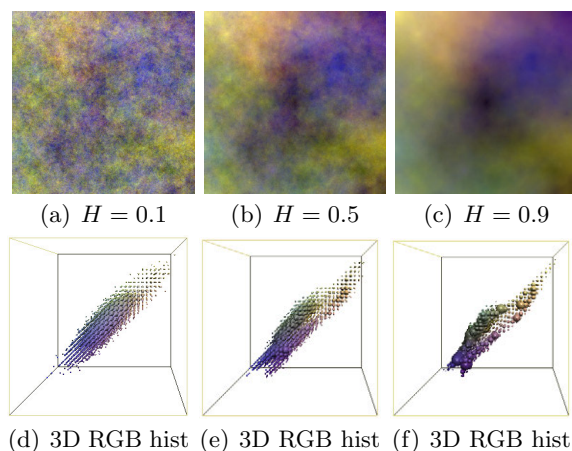
Using the fractal dimension estimation approaches - probabilistic box-counting and covering blanket - that will be presented in Chapter 2.2, we obtain the following results for the color fractal images in Figure 2.15, presented in Table 2.1.

dim_B	dim_{MB}
2.103 ± 0.004	2.308 ± 0.001
2.098 ± 0.004	2.295 ± 0.001
2.105 ± 0.004	2.321 ± 0.001

Table 2.1: Complexity for color fractal images with $H = 0.9$.

In the following experiment, we used different sigma values between the RGB color components and different H values. In Figures 2.16, 2.17 and 2.18 we chose $\sigma = 0.9$ for only two color components, while for the other two the correlation was zero.

Fig. 2.16: Vector color fractal images for $\sigma_{rb} = 0.9$.Fig. 2.17: Vector color fractal images for $\sigma_{gb} = 0.9$.

Fig. 2.18: Vector color fractal images for $\sigma_{rg} = 0.9$.

Performing the same complexity assessment, using probabilistic box-counting and covering blanket, we obtain the following results for the color fractal images in Figures 2.16, 2.17 and 2.18 presented in Table 2.2.

H	σ	dim_B	dim_{MB}
0.1	$\sigma_{rb} = 0.9$	3.762 ± 0.156	0.596 ± 0.001
0.5	$\sigma_{rb} = 0.9$	2.993 ± 0.024	1.280 ± 0.001
0.9	$\sigma_{rb} = 0.9$	2.114 ± 0.005	2.352 ± 0.001
0.1	$\sigma_{rb} = 0.9$	3.781 ± 0.145	0.600 ± 0.001
0.5	$\sigma_{rb} = 0.9$	2.981 ± 0.038	1.284 ± 0.001
0.9	$\sigma_{rb} = 0.9$	2.112 ± 0.005	2.310 ± 0.001
0.1	$\sigma_{rg} = 0.9$	3.852 ± 0.170	0.599 ± 0.001
0.5	$\sigma_{rg} = 0.9$	3.053 ± 0.008	1.253 ± 0.001
0.9	$\sigma_{rg} = 0.9$	2.128 ± 0.005	2.279 ± 0.001

Table 2.2: Complexity estimation for images in Figures 2.16, 2.17 and 2.18.

2.4 Visual impact of increment distribution

In this section we experiment with various distribution for the increments during the midpoint displacement color fractal image generation. For different instances of the random number generator used for Gaussian-distributed increments in the process of texture synthesis rather visually similar results are obtained (see Figure 2.19). However when the distribution of the increments is not Gaussian, various visual effects can be obtained. For instance, when using exponentially-distributed increments, the color fractal images in Figure 2.21 are obtained. When the increments are uniformly-distributed,

the color fractal images in Figure 2.23 are synthesized. The 3D RGB corresponding color histograms are presented as well in Figure 2.20, 2.22 and 2.24.

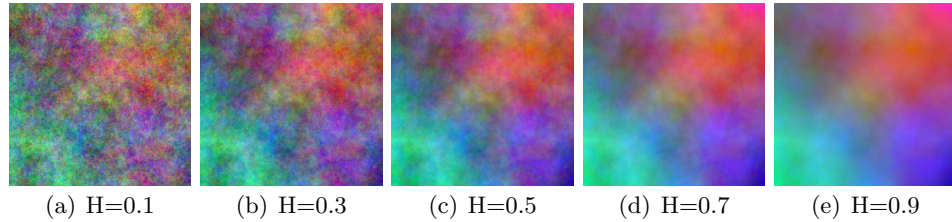


Fig. 2.19: Another instance of the Gaussian distribution.

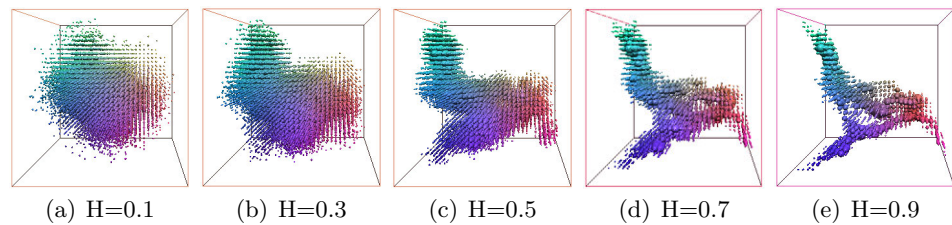


Fig. 2.20: 3D RGB histogram of color fractals images in 2.19.

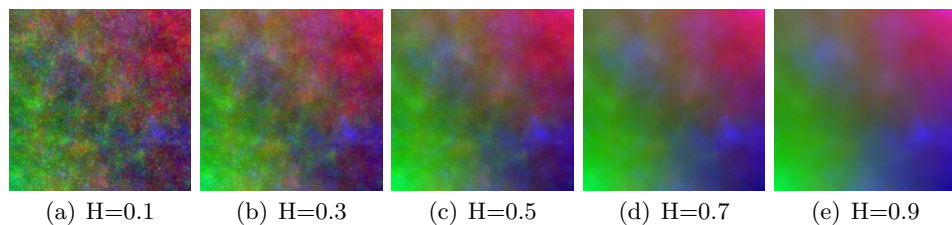


Fig. 2.21: Visual impact of exponentially-distributed increments ($\lambda = 2$).

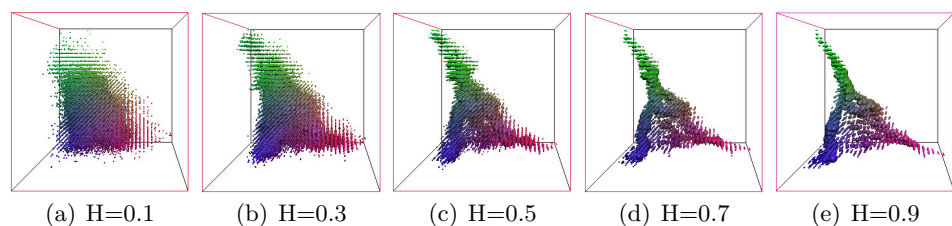


Fig. 2.22: 3D RGB histogram of color fractals images in 2.21.

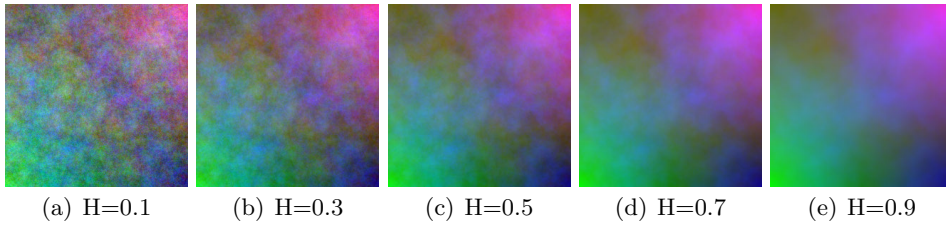


Fig. 2.23: Visual impact of uniformly-distributed increments.

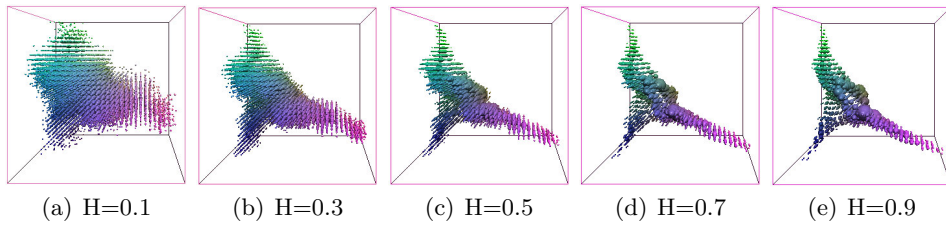


Fig. 2.24: 3D RGB histogram of color fractals images in 2.23.

2.5 Weierstrass function

The Weierstrass function is a particular type of fractal, being continuous everywhere, in every point, but differentiable nowhere. The class of functions which are continuous everywhere but nowhere differentiable had been introduced in the 19th century, before B. Mandelbrot made them popular through the name of *fractals*. The earliest known example is due to Czech mathematician B. Bolzano, who exhibited such a function in the years around 1830, but which was published only in 1922. C. Cell erier and B. Riemann also mentioned such functions in their papers, although they were also published later. K. Weierstrass was the first to publish a paper in which to exemplify functions which are continuous everywhere but nowhere differentiable, including also a proof of this assumption [124].

The function originally defined by Weirstrass is:

$$f(x) = \sum_{n=0}^{\infty} a^n \cos(b^n \pi x) \quad (2.17)$$

where $0 < a < 1$, b is a positive odd integer and $ab > 1 + \frac{3}{2}\pi$. G. H. Hardy expanded the range of possible values for a and b proving that the non-differentiability still holds for $ab > 1$ [56]. B. Mandelbrot pointed out that the Weierstrass function is a fractal and introduced a more general form for the equation (2.17), which is known as the Weierstrass-Mandelbrot function:

$$W(x) = \sum_{k=-\infty}^{\infty} \frac{(1 - e^{ib^k x})}{b^{k(2-D)}} \quad (2.18)$$

where $b > 1$ and $1 < D < 2$. The real part of (2.18) is the cosine fractal function:

$$C(x) = \operatorname{Re}(W(x)) = \sum_{k=-\infty}^{\infty} \frac{(1 - \cos(b^k x))}{b^{k(2-D)}} \quad (2.19)$$

For a detailed description of the Weierstrass-Mandelbrot function see [12]. According to [12], when D is close to 2, $W(x)$ is a model for $1/f$ noise and when $D < 1$, $W_2(x)$ is not a fractal. $W(x)$ has the box-dimension D [40].

In Figure 2.25 we show the Weierstrass function for $a = 0.5$ and $b = 3$, as well as our proposed extensions to grayscale and color image domains. For the color image we worked in RGB, based on the independence hypothesis between the color planes. This is still work in progress and the fractal dimension of these images has to be estimated and mathematically proved.

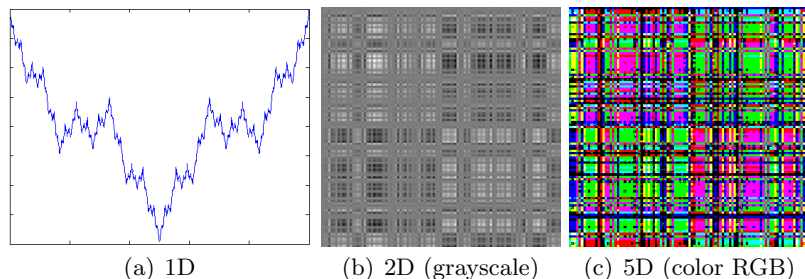


Fig. 2.25: Weierstrass function and fractal images.

2.6 Perlin noise

Another method used for fractional Brownian motion functions generation was proposed by Musgrave in [86] and [87] and by Saupe in [109] and is based on summing band-limited *base* signals. This algorithm also permits the adjustment of the lacunarity and fractal dimension parameters. The bidimensional base function, is the so-called Perlin noise function, introduced in [95], which is a band-limited signal of random amplitude variation (Fig. 2.26(a)). Albeit the fact that mathematically the link to fractals it is not proven, Perlin noise is successfully used to generate various textures in computer graphics.

The Perlin noise ($N : \mathbb{R}^n \rightarrow \mathbb{R}$) is implemented using a set of random gradient values defined at discrete points within the domain of the function.

In those discrete points the function value is zero and its rate of variation is given by the gradient value associated with that point. The function values at non-integer points is computed using an interpolation given by the cubic function (e.g. $y = 3x^2 - 2x^3$). The noise function may have at most one zero-crossing between two consecutive discrete points, so the highest frequency of the noise signal is f where f is also the spacing frequency of the integer points within the function domain; the lowest frequency is $\frac{f}{2}$. However we may add low frequency components to the signal by setting non-zero function values at integer points in the domain. In order to scale the frequency of N by a factor k , a scalar multiplication $k\mathbf{p}$ has to be performed on the domain vectors \mathbf{p} .

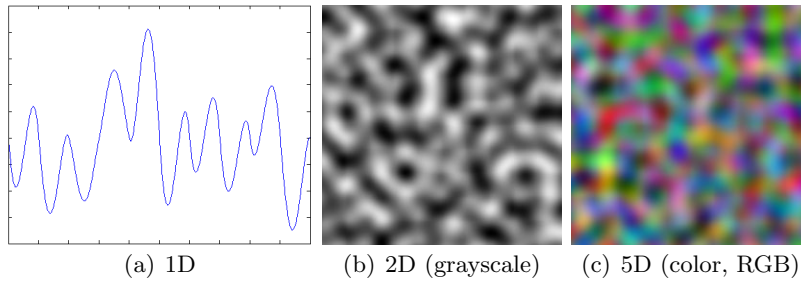


Fig. 2.26: Perlin noise.

Using the Perlin noise, the fractional Brownian motion function can be defined as [87]:

$$X(\mathbf{p}) = \sum_{i=1}^m N(\mathbf{p}\lambda^i)\lambda^{-Hi} \quad (2.20)$$

in which H is the Hurst exponent which is in connection with the fractal dimension, λ is the fractal lacunarity and m is the number of additions performed, which is typically comprised between 3 and 12. The randomness of the function is given by the random gradients within the Perlin noise definition.

In Figure 2.26(b) we show the grayscale image resulting from the extension of the presented approach to a two-dimensional support space. We present also in Figure 2.26(c) the result we obtained by preliminary investigation of possibilities of extending the Perlin noise to color images, using vector gradients expressed in RGB.

Chapter 3

Fractal features

The fractal analysis proved to be of a great interest for the digital image analysis, being widely used in applications such as finance and stock market prediction, malign/benign analysis in medicine, quality of food analysis, civil engineering and even art [115]. In this chapter we discuss two fractal features: fractal dimension and lacunarity. Fractal dimension is a measure that characterizes the complexity of a fractal, indicating the amount of irregularity and how much the available space is filled. Lacunarity is a complementary fractal measure which indicates how the space is filled, being similar to a distribution function. The two properties are usually used for discriminating between various signals exhibiting fractal properties, like texture images [26] [73]. The fractal dimension, for instance, is used to characterize, classify or to segment images or regions [24] [101] [85] [88].

The fractal features are perfectly suited for the multi-scale analysis of images and multi-dimensional signals, by observing the variation of a measure as a function of the analysis scale. For pure deterministic fractals, the measure is constant in a log-log bi-dimensional space and, by construction, invariant to scale transformation, rotation or translation of the object. These characteristics justify the choice of this operator in many texture analysis tools.

3.1 Fractal dimension

B. Mandelbrot defined the fractals as sets or objects with a Hausdorff dimension exceeding the topological dimension. The topological dimension is the smallest integer value n , so that if we cover the given set by a family of open sets, there are no more than $n + 1$ with common points [37]. The Hausdorff dimension is based on the definition of the Hausdorff measure \mathcal{H} . For a given set $F \subset \mathbb{R}^n$ and $s \in \mathbb{R}^+$, for any $\delta > 0$, by definition:

$$\mathcal{H}_\delta^s(F) = \bigwedge \left\{ \sum_{i=1}^{\infty} |U_i|^s : F \subset \bigcup_{i=1}^{\infty} U_i, |U_i| < \delta \right\} \quad (3.1)$$

where \bigwedge is the *infimum* of the set and $|U_i|$ represents the diameter of set U_i , given by the maximum distance between two points $a, b \in U_i$ [40]. Thus the initial set F is covered with a countable family of sets U_i with the diameter smaller than δ and minimizing the sum of the power of s of the diameters of the sets U_i . Then the measure

$$\mathcal{H}^s(F) = \lim_{\delta \rightarrow 0} \mathcal{H}_\delta^s(F) \quad (3.2)$$

is called the s -dimensional Hausdorff measure. It's demonstrated that $\mathcal{H}^s(F)$ is a decreasing function with respect to s . Moreover, there exists a value s_0 so that

$$\mathcal{H}^s(F) = \begin{cases} \infty & \text{if } 0 \leq s \leq s_0 \\ 0 & \text{if } s > s_0 \end{cases} \quad (3.3)$$

This critical value where the function skyfalls from infinity to zero is called Hausdorff dimension, denoted $\dim_H F$ and defined by:

$$\dim_H F = \inf \{s \geq 0 : \mathcal{H}^s(F) = 0\} = \sup \{s : \mathcal{H}^s(F) = \infty\} \quad (3.4)$$

Such a definition is difficult to use in practical implementations, consequently various approximations were proposed. One of them is the similarity dimension $\dim_S F$ which is defined as the ratio of the logarithm of the number of subsets composing a fractal object and its scaling factor r :

$$\dim_S F = -\frac{\log N}{\log r} \quad (3.5)$$

To illustrate, let's take the example of the Koch curve. In the construction process of this fractal, which repeats itself iteratively or recursively, the initial segment is divided in three equal parts and the middle part is replaced with an equilateral triangle missing the bottom. Thus the fractal is composed of four objects similar to the initial set, scaled by a factor of three. Then the similarity dimension of the Koch curve is:

$$\dim_S F_{Koch} = -\frac{\log 4}{\log \frac{1}{3}} = 1.26 \quad (3.6)$$

For non-deterministic or probabilistic fractals this dimension cannot be computed, because of the difficulty in determining the two measures N and r due to the randomness of the analyzed object. In order to overcome this issue, various methods for Hausdorff dimension estimations were proposed.

These methods take into account the intrinsic randomness of a fractal and are based on assessing a certain characteristic measure of the analyzed objects, like area or length. Consequently, various definitions of the fractal dimension emerged, depending on the proposed approach: (i) *box counting* dimension, (ii) correlation dimension, (iii) Minkowski-Bouligand dimension, their purpose being of estimating the Hausdorff dimension. All these dimensions, described in the following section, are called generically as fractal dimensions (DF) in the literature. According to B. Mandelbrot only the Hausdorff dimension is a fractal dimension.

3.2 Fractal dimension estimation

Albeit the fact that a plethora of algorithmic approaches exist for the *computation* or the estimation of the fractal dimension, only few of them offer the theoretical background that links them to the Hausdorff dimension. However, let us start with a simple and intuitive example, by considering the simple geometrical shapes in Figure 3.1. If we consider a segment, which is a one-dimensional object, divided in N equal parts, then each part is a scaled version of the original segment by a factor of $r = \frac{1}{N}$. To reconstruct the whole object we need N such scaled parts, which is $Nr^1 = 1$. If we take the square, which is a two-dimensional object, divided in N equal parts, scaled by a factor $r = \frac{1}{N^{\frac{1}{2}}}$, then the whole square is reconstructed as $Nr^2 = 1$. Furthermore, the cube is a three-dimensional object and if we divide it in N equal parts, each part is a cube scaled by a factor $r = \frac{1}{N^{\frac{1}{3}}}$ and thus its reconstruction is done as $Nr^3 = 1$. If we generalize, any object composed of N copies of it, scaled by a factor r , has the dimension $d = \frac{-\log N}{\log r}$.

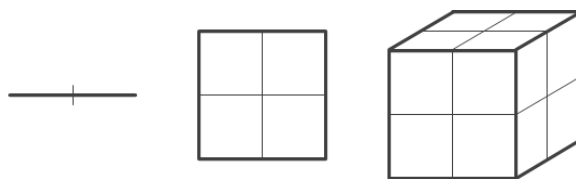


Fig. 3.1: Three simple Euclidian objects.

3.2.1 The box-counting dimension

From the different expressions directly linked to the theoretical one of the Minkowski-Bouligand [40], the box-counting dimension and estimation approach are the most popular due to the simplest algorithmic formulation, compared to the Hausdorff dimension. The algorithm for the estimation of the box-counting dimension was introduced in [45] and it aims at covering the space containing the fractal objects with sets of known dimension, called

boxes, and counting how many boxes cover the object. This process is repeated for various box sizes. For a fractal object F , the number of boxes $N(\delta)$ varies as a function of their dimension δ^1 according to the equation:

$$N_\delta(F) = \delta^{-\dim_B F} \quad (3.7)$$

where $\dim_B F$ is called the *box counting* dimension, an approximation of the Hausdorff dimension. Further on, we can write:

$$\log N_\delta(F) = -\dim_B F \log \delta \quad (3.8)$$

Consequently, the box counting dimension is:

$$\dim_B = -\frac{\log N_\delta}{\log \delta} \quad \delta \neq 1 \quad (3.9)$$

where $N(\delta)$ is the number of boxes of size δ needed to cover the fractal set.

Practically, it can be determined as the slope of the regression line through the measurement points (the number of boxes that cover the analyzed signal, as a function of box size) in logarithmic coordinates. Various approaches were proposed for the box-counting implementation. In [108] the definition domain is divided into boxes of variable size. We illustrate an example in Figure 3.2 for three measurement points: $\delta_1 = 3$, $\delta_2 = 5$ and $\delta_3 = 7$.

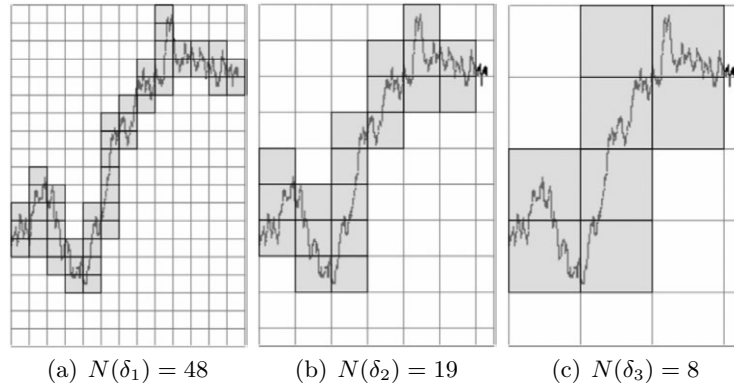


Fig. 3.2: Illustration of the box counting dimension estimation.

For the given example, the box-counting dimension of the analyzed signal is estimated as the slope of the regression line through the points $\langle \log(\delta), -\log(N_\delta) \rangle$:

¹Note that in this chapter δ denotes the size of analysis boxes or the diameter of the covering sets.

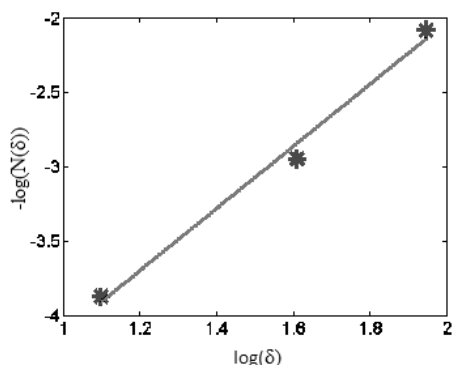


Fig. 3.3: Regression line slope as fractal dimension estimation.

We draw the attention on the impact of the regression line computation on the box-counting estimation method. The estimation procedure may induce an important variation, as it will be seen in the following section. Most of the articles on fractal dimension box counting estimation mention the least square method for the computation of the regression, the correct choice for theoretical fractal objects. But none of them mentions the large variation that may occur (sometimes up to 20%) depending on the weighting function used in the least-square line-fitting method for natural/real objects or synthetic fractals objects.

3.2.2 Probabilistic box-counting

The probabilistic algorithm proposed by Voss [123] based on the proposal of Mandelbrot [79] (see chapter 34), considers the image as a set of points in an Euclidian space. According to [70], the spatial arrangement of the set is characterized by the probability matrix $P(m, \delta)$, the probability of having m points included into a cube of size δ called a box, centered in an arbitrary point of the analyzed image. For each value of δ , the matrix is normalized so that:

$$\sum_{m=1}^Q P(m, \delta) = 1, \quad \forall \delta \quad (3.10)$$

where Q represents the number of points that can fall within a box of size δ . Given the total number of points in the image is M , the number of boxes that contain m points is $(M/m)P(m, \delta)$. Consequently, the total number of boxes needed to cover the image is:

$$\langle N(\delta) \rangle = \sum_{m=1}^N \frac{M}{m} P(m, \delta) = M \sum_{m=1}^N \frac{1}{m} P(m, \delta) \quad (3.11)$$

which is an estimate of $N(\delta)$, so the amount $\sum_{m=1}^Q \frac{1}{m} P(m, \delta)$ is directly proportional to $\delta^{-\dim_B F}$ and can be used for the computation of the box-counting dimension: $N(\delta) = \sum_{m=1}^N \frac{1}{m} P(m, \delta) \propto \delta^{-\dim_B}$.

If a gray-level image can be modelled as a discrete surface $z = f(x, y)$ in a three-dimensional space, where z is the luminance in every (x, y) point of the space, the model can be extended for color and multispectral images. However, until [63] there was no reference to a model and fractal dimension estimation approach dedicated to color images, despite the fact that the theoretical background for fractal analysis is based on the Borel set measure in an n -dimensional Euclidian space [40]. There are very few approaches that link the fractal dimension to color and multispectral images and the purpose is only restricted to marginal color analysis and transformation of a gray scale problem into a false color one [1].

We considered in [63] a color image as a hyper-surface in an RGB color space: $f(x, y) = (r, g, b)$. Therefore in the case of color images we deal with a 5-dimensional Euclidian hyper-space and each pixel can be seen as a 5-dimensional vector (x, y, r, g, b) . We have chosen to work in RGB space due to its cubic organisation coherent with the 2-dimensional spatial support of the image. Thus, we could meet the constraint of expression in a 5-dimensional space.

The classical algorithm of Voss defines cubes of size δ centered in the current pixel $(x, y, z = f(x, y))$ and counts the number of pixels that fall within a cube determined by the following two opposite corners: $(x - \frac{\delta}{2}, y - \frac{\delta}{2}, z - \frac{\delta}{2})$ and $(x + \frac{\delta}{2}, y + \frac{\delta}{2}, z + \frac{\delta}{2})$. A direct extension of the Voss approach to color images would count the pixels $F = f(x, y, r, g, b)$ for which the Euclidian distance to the center of the hyper-cube $F_c = f(x_c, y_c, r_c, g_c, b_c)$ would be smaller than δ :

$$|F - F_c| = \sqrt{\sum_{i=1}^5 |f_i - f_{ci}|^2} \leq \delta \quad (3.12)$$

Given that the Euclidian distance in RGB space does not correspond to the perceptual distance between colors, we prefer to use instead the Minkowski infinity norm:

$$|F - F_c| = \max(|f_i - f_{ci}|) \leq \delta \quad \forall i = \overline{1, 5} \quad (3.13)$$

Practically, for a certain square of size δ in the (x, y) support, we count the number of pixels that fall inside a 3-dimensional RGB cube of size δ , centered in the current pixel.

In Figure 3.4 we present four color texture images exhibiting fractal properties used in our experiments in this chapter: a flat orange plane, an industrial sponge (monochrome texture of low complexity), a psoriatic lesion

(a more complex texture with variations in color) and a lichen (higher complexity both in texture and color). For three of them we plot the evolution of $N(\delta)$ in Figure 3.5: for *orange* $N(\delta)$ is a straight line, corresponding to a fractal dimension of 2.0. For *psoriasis* and *cladonia*, the evolution is no longer linear, which makes the estimation of the regression line slope a more delicate issue. A correction has to be applied, which is proposed below.

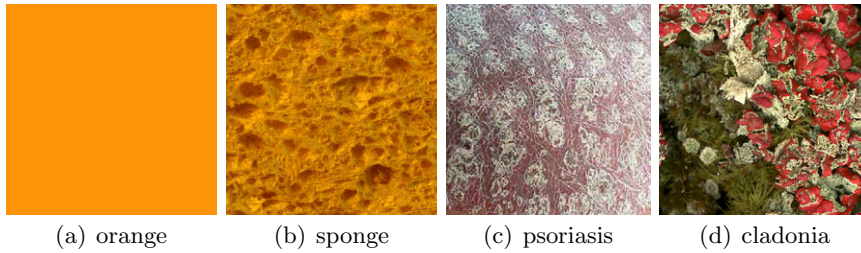


Fig. 3.4: Four color texture fractal images.

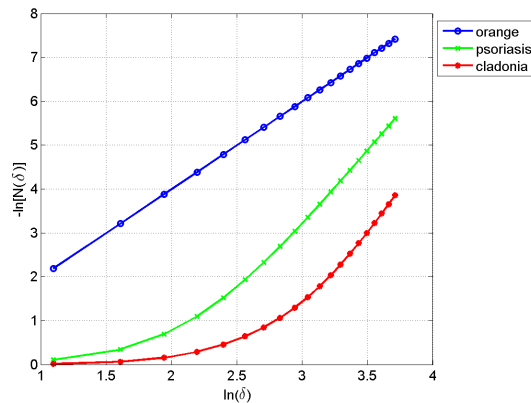


Fig. 3.5: The $N(\delta)$ curves in a log-log space for images in Figure 3.4.

For the validation of our proposed estimation method we used the synthetic color fractals images from the previous chapter of this book (see Figure 2.3), for which we demonstrated the correct ranking of the color texture complexity in the RGB color space. In Figure 3.6, we show the $N(\delta)$ curves in a log-log space, represented with a black thick starred line. On the same graphs we plot the regression lines obtained from different methods to estimate the probabilistic box-counting fractal dimension of three color fractal images, with $H = 0.9$, 0.5 and 0.1 , respectively. There exist several approaches to the linear regression computation, all based on an iteratively reweighted least-square algorithm. Since Mandelbrot, in all the cited articles, only the *ordinary* least squares method (*ols*) is mentioned for the

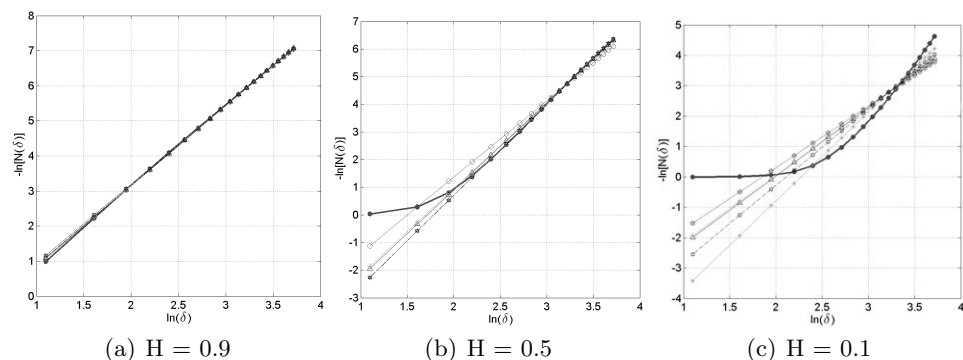


Fig. 3.6: $N(\delta)$ curves and the corresponding regression lines.

estimation of the slope of the $N(\delta)$ curves in a log-log space. We investigated the usage of nine methods for linear regression on noisy datasets available in the Matlab Statistics Toolbox. The difference between the nine methods consists mainly in the weighting function used for the computation of the residuals at each iteration, and implicitly to give lower importance to the points that do not fit *very well*.

At a first glance, the generated complexity in images is well captured by our color fractal measure, but the estimated fractal dimension is not well correlated to the one of the generated synthetic color fractal images for all linear regression approaches (see Table 3.4). The mismatch is clearly due to the poorly calculated slope of the regression line. Moreover, one may note that when the complexity of the fractal textures grows up, the $N(\delta)$ curve bends, diverting from a straight line. But still, for large scales, the $N(\delta)$ curves indicate the correct ranking.

A thorough introspective, presented in [63], indicates that for the generated fractals of middle and high complexity, the $N(\delta)$ measurements are altered for the small scales. Apparently, the fractal dimension *restricted* to those scales tends to be close to zero, which is clearly false. By investigating the $P(m, \delta)$ matrix, if $P(1, \delta)$ equals one or is very close to one, that is a clear indication that the hyper-cube of size δ is inappropriate for correctly measuring the fractal dimension, in other words is not able to capture the variations in the fractal image. Those points will lead to a small fractal dimension and will also introduce a larger variation in the estimation of the slope of the regression line. So the different linear regression approaches could not solve themselves this problem, which is more complex than a noise addition to the measure.

In order to overcome this situation, we chose to weight the sample values according to their expected accuracy. For the fractal image of high complexity the dimension measures are less affected by the quantization error for medium and large box sizes than for the small ones. Therefore, it seems

method	H = 0.9	H = 0.5	H = 0.1
ols	2.301	2.758	2.032
andrews	2.253	3.303	2.923
bisquare	2.253	3.303	2.923
cauchy	2.275	3.284	2.288
fair	2.287	3.119	2.222
huber	2.286	3.163	2.230
logistic	2.284	3.154	2.255
talwar	2.279	3.300	2.032
welsch	2.254	3.304	2.517
mean	2.275	3.187	2.380
variance	0.0003	0.0316	0.1153

Table 3.1: The fractal dimension for the three color fractal images as a function of the least-square method.

natural that the points corresponding to the medium and large boxes to be taken into account more than the ones corresponding to the small boxes. In case of a gray-scale image the maximum quantification error for a pixel is one given that the current value may have a correspondence in the continuous domain that varies within the interval ± 0.5 . For a cube of size $\delta = 3$, the maximum number of pixels that may fall within is $\delta^2 = 9$, thus the maximum error is 9. By extrapolation and normalization of the maximum error with respect to the volume of the cube, the maximum quantization error will be: $\varepsilon(\delta) = \frac{\delta^2}{\delta^3} = \frac{1}{\delta}$. For a color image, the error triples with the number of color coordinates. The dependency of the quantization error on the size of the boxes is depicted in Figure 3.7.

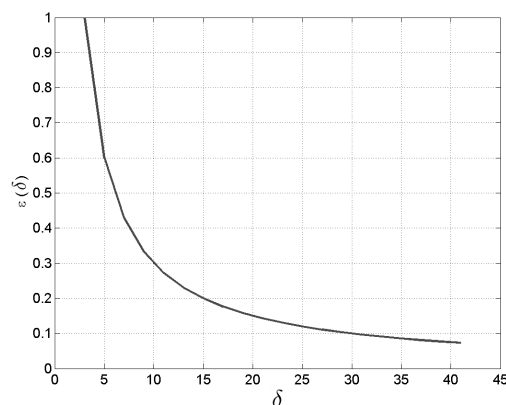


Fig. 3.7: The maximum quantization error as a function of box-size.

We therefore proposed three different weighting functions, but the most effective proved to be the following one:

$$w(\delta) = \frac{1}{\varepsilon^2(\delta)} \quad (3.14)$$

In Figure 3.8 one can see the impact of the weighting function in the estimation of the regression line (see also Table 3.2). As expected, the estimated slope is more linked to the middle and high scales of the fractal measure.

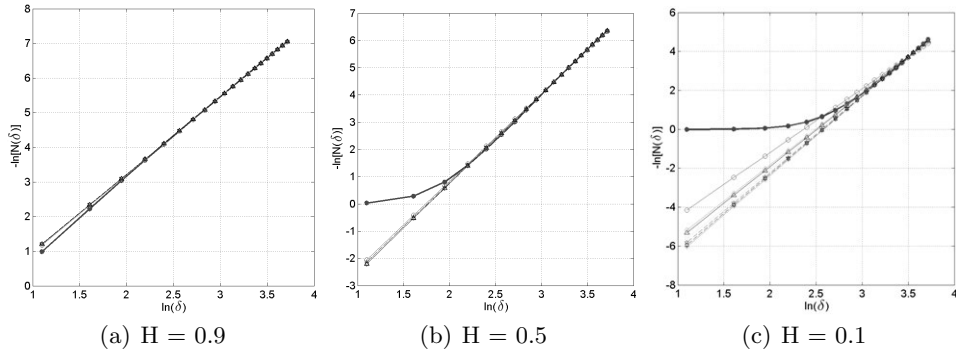


Fig. 3.8: $N(\delta)$ curves the regression lines using weighting function.

method	H = 0.9	H = 0.5	H = 0.1
ols	2.251	3.213	3.279
andrews	2.233	3.249	4.066
bisquare	2.233	3.251	4.066
cauchy	2.234	3.279	3.895
fair	2.239	3.274	3.712
huber	2.237	3.272	3.773
logistic	2.238	3.274	3.770
talwar	2.233	3.241	3.974
welsch	2.233	3.276	4.023
mean	2.237	3.258	3.840
variance	0.000035	0.00048	0.0621

Table 3.2: The fractal dimension for all the nine methods.

The fractal dimension obtained after weighting the measured data exhibits an increased range of values up to 4.066, as well as a smaller variance for the results of the nine estimation methods. For the images presented in Figure 3.4 we obtain the color fractal dimensions: 2.00, 3.39 and 3.71, respectively, using the weighting function and the andrews and the bisquare regression methods. For the same images, we present in Table 3.3 the results

of a marginal analysis, i.e. the fractal dimension computed for the gray-scale images, as well as for each of the three RGB planes. From an RGB color point of view, definitely *cladonia* is more complex than *psoriasis*, but this fact cannot be captured by a marginal analysis, which surprisingly enough indicates the contrary.

image	gray-scale	red	green	blue
“psoriasis”	2.707	2.713	2.700	2.706
“cladonia”	2.527	2.536	2.551	2.479

Table 3.3: Marginal fractal analysis for the images in Figure 3.4.

We show in Figure 3.9 the impact of the choice of the distance expression on the estimation of the fractal dimension for the synthetic color fractal images. We compared the Minkowski infinity norm (i.e. Chebyshev distance) against the Euclidian distance and one can see that the latter one leads to an incorrect ranking of the texture complexity.

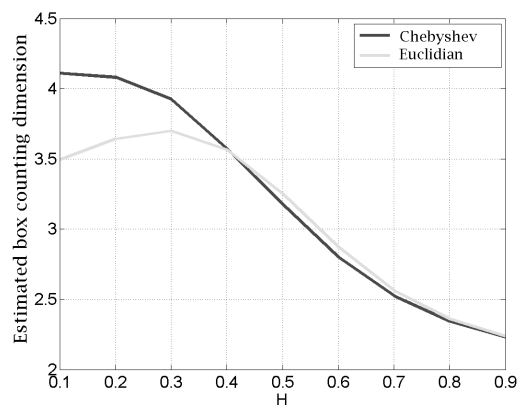


Fig. 3.9: Distance choice impact on fractal dimension estimation for the color texture images in Fig. 2.3.

In Figure 3.10 we show three color textures from the VisTex data base, with their estimated box-counting fractal dimensions, using the probabilistic box-counting approach presented in this chapter. The estimated fractal dimensions are in accordance with their perceived complexity.

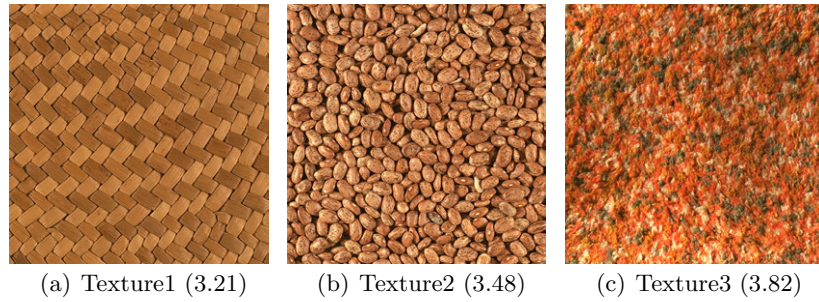


Fig. 3.10: Three color textures from the VisTex data base.

The corresponding $N(\delta)$ curves are presented in Figure 3.11. We stress out the fact that for certain scales where the curves are linear, these natural objects exhibit fractal properties.

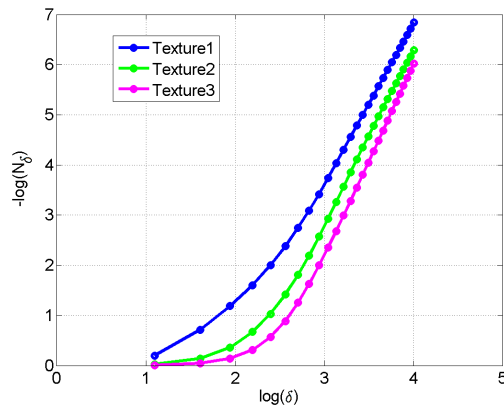


Fig. 3.11: The $N(\delta)$ curves for the textures in Fig. 3.10.

In [36] the authors are using only the linear part of the $\log N(\delta)$ for the estimation of the fractal dimension. In [59] it is argued that this approach does not always lead to a correct estimation. A solution is proposed in [94], by introducing the concept of *fractal signature* - a vector of locally estimated fractal dimensions. This opens the discussion to the multifractality nature of real objects.

3.2.3 Correlation dimension

In chaos theory, the correlation dimension—usually denoted by ν —is a measure of how much space is occupied by a set of random points [48]. It is intimately connected to the fractal dimension and even referred to as a type

of fractal dimension. We propose an extension to color images of the existing correlation dimension proposed by Grassberger & Procaccia.

The correlation dimension [48] is based on the computation of the correlation integral $C(\delta)$ for a set of points $\{x_1, x_2, \dots, x_N\}$, defined as:

$$C(\delta) = \lim_{N \rightarrow \infty} \frac{q}{\frac{N(N-1)}{2}} = \lim_{N \rightarrow \infty} \frac{2q}{N(N-1)} \quad (3.15)$$

where q is the number of pairs (x_i, x_j) for which the distance $|x_i - x_j|$ is less than δ , or more generally speaking $d(x_i, x_j) < \delta$. Then the correlation dimension $\dim_C F$ of a fractal object F is:

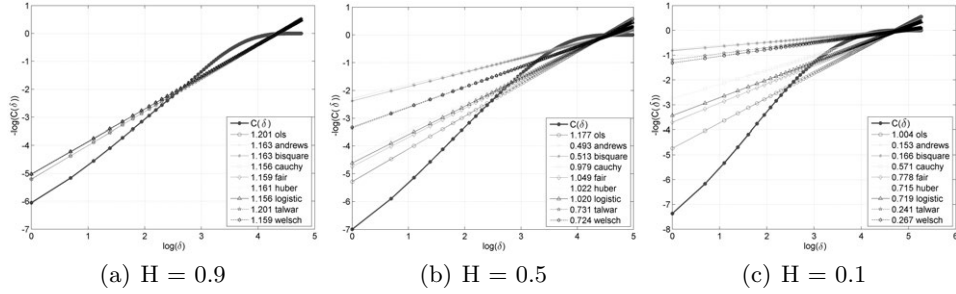
$$\dim_C F = \lim_{\delta \rightarrow 0} \frac{\log C(\delta)}{\log \delta} \quad (3.16)$$

and can be computed as the slope of the regression line through the points $\langle -\log[C(\delta)], \log(\delta) \rangle$.

In [10], Bardet proves the relationship between the local correlation dimension and the Hausdorff dimension of continuous random fields, then it uses it to analyze the complexity of fractional Brownian motion. For a \mathbb{R}^d -valued continuous (with respect to the \mathbb{R}^d -Lebesgue measure) random vector process the local correlation dimension ν —if it exists—is smaller than the Hausdorff dimension $\dim_H X$: $0 \leq \nu \leq \dim_H X \leq d$ and that in some particular situations the equality stands: $\nu = \dim_H X = d$.

The generalization to \mathbb{R}^d of the correlation dimension exists (see [10]), but there are no particular results for color images. In a first approach we use the ΔE color distance in the CIE Lab color space between colors of a given neighborhood. The reason is twofold: (i) the Euclidian distance makes sense in the CIE Lab color space and (ii) the distance is perceptually linear, being in accordance with the color difference perception of the human visual system. Thus the fractal complexity we estimate by the modified correlation dimension integrates naturally the human perception of the complexity of a given color texture. We validate our approach both on synthetic and natural images exhibiting fractal properties.

We used three of the images from Figure 2.4 [61], with different complexity, i.e. different values of the Hurst factor H . The following $C(\delta)$ curves are obtained, presented in a log-log space in Figure 3.12 together with the regression lines. The slope of the regression line given by the nine flavours available in Matlab of the least square regression line estimation approach is also presented in Table 3.4. The curves tend to bend for large values of δ – as the large color distances are not numerous, the correlation integral $C(\delta)$ reaches 1.

Fig. 3.12: The $C(\delta)$ curves in the log-log space.

method	H = 0.9	H = 0.5	H = 0.1
ols	1.201	1.177	1.004
andrews	1.163	0.493	0.153
bisquare	1.163	0.513	0.166
cauchy	1.156	0.979	0.571
fair	1.159	1.049	0.778
huber	1.161	1.022	0.715
logistic	1.156	1.020	0.719
talwar	1.201	0.731	0.241
welsch	1.159	0.724	0.267
mean	1.1688	0.856(4)	0.51267
variance	0.0003402	0.06154203	0.09780225

Table 3.4: The correlation dimension for the three color fractal images.

The estimated fractal complexity has a significant variance and for the high complexity image ($H=0.1$) the mean estimated slope is smaller than the one for a less complex image ($H=0.5$). In other words, the correct ranking of the synthetic color fractal images based on their complexity cannot be reached. The different linear regression approaches could not solve themselves this problem and a possible solution is to weight the $C(\delta)$ values according to their estimated accuracy. The proposed weighing function is designed to solve the lack of accuracy for large values of δ , based on the intrinsic properties of the fractal model used by the color fractal image generator [63, 61]. As the fractal complexity is linked to the statistical behavior between the spatial distance and the color distance in a power law [40], the weighing function must respect such a law. In the midpoint displacement fractal image generation algorithm the largest color distances are generated for the farthest spatial pixels in the image, i.e. the four corners. Then the image is divided in four squares and the process is re-iterated with half the initial topological distances, thus smaller color distances, according to a Brownian process. As the iteration number grows, the color distances are proportional to an ever decreasing topological Euclidian distance, therefore more smaller color distances are generated, and their number is a power of 4. We therefore propose to use the following weighing function:

$$w(\delta) = 4^{\delta_{max} - \delta} \quad (3.17)$$

where δ_{max} is the maximum value of δ (see Figure 3.13).

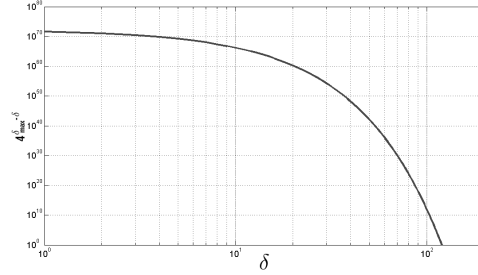


Fig. 3.13: The proposed weighting function.

In Figure 3.14 one can see the impact of the proposed weighting function in the estimation of the regression line (see also Table 3.5). As expected, the estimated slope is more linked to the middle and low scales of the measure, thus being able to reach the correct ranking according to the perceived complexity of the color fractal images.

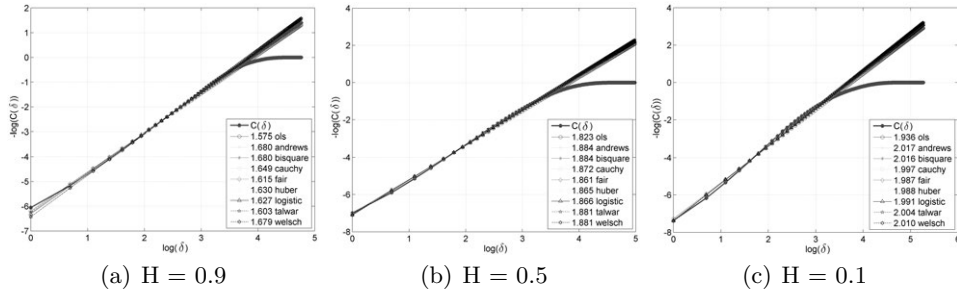


Fig. 3.14: The $C(\delta)$ curves in the log-log space using the $w(\delta)$ weighting.

method	H = 0.9	H = 0.5	H = 0.1
ols	1.575	1.823	1.936
andrews	1.680	1.884	2.017
bisquare	1.680	1.884	2.016
cauchy	1.649	1.872	1.997
fair	1.615	1.861	1.987
huber	1.630	1.865	1.988
logistic	1.627	1.866	1.991
talwar	1.603	1.881	2.004
welsch	1.679	1.881	2.010
mean	1.6376	1.8686	1.994
variance	0.0014	0.0003688	0.0006045

Table 3.5: The correlation dimension for all the nine methods and for the proposed weighting function.

Clearly, by computing strictly the distance between pixel colors in an image (or a given neighborhood) disregarding the spatial arrangement of pixels, the fractal dimension is underestimated. Moreover, the same correlation dimension may be estimated for images with the same color content but different topology (see the two signals illustrated in Figure 3.15).

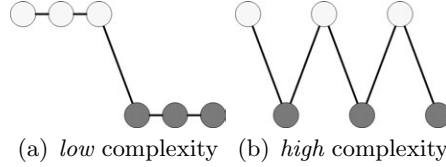


Fig. 3.15: Two different signals with the same correlation dimension.

Therefore we propose integrating of the spatial distance in the distance computed between colors. We consider each pixel as a 5D vector: $\mathbf{x} = \{x, y, r, g, b\}$ or $\mathbf{x} = \{x, y, L, a, b\}$ if the image is represented using RGB or CIE Lab spaces. The definition of the distance, however, is not straightforward, given the different nature of the components: (x, y) are spatial coordinates and (r, g, b) or (L, a, b) are color coordinates. For natural images, the dynamic range of spatial coordinate values can be extremely large (due to current image sensor resolution of tens of MPixels), compared to the color component dynamic range which remains in the range of $[0, 255]$. Given that for the synthetic images we used for validation so far, the color components are produced as linear combinations of spatial components, being directly proportional, and the size of the generated images is 256×256 pixels to match the available range of color component values, we use the Euclidian distance $d(\mathbf{x}_1, \mathbf{x}_2)$ between two pixels \mathbf{x}_1 and \mathbf{x}_2 :

$$\sqrt{(x_1 - x_2)^2 + (y_1 - y_2)^2 + (L_1 - L_2)^2 + (a_1 - a_2)^2 + (b_1 - b_2)^2} \quad (3.18)$$

Using this distance definition and the weighting function proposed we obtain the following results in Figure 3.16 and Table 3.6. One can see that the estimation is improved in the sense of increasing the dynamic range of values and getting closer to the ones given by the box-counting estimation.

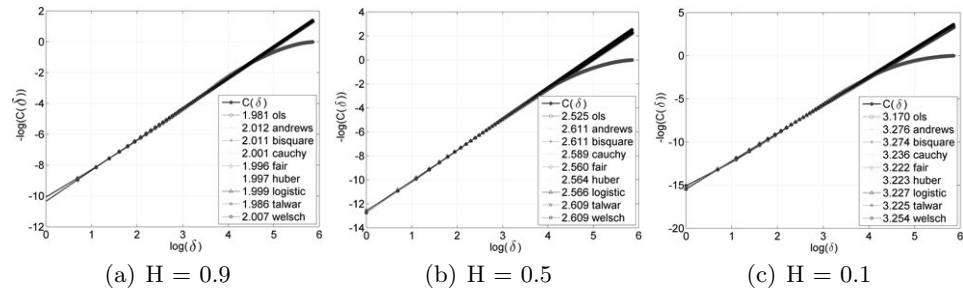


Fig. 3.16: The $C(\delta)$ curves using the 5-D distance and weighting function.

method	H = 0.9	H = 0.5	H = 0.1
ols	1.981	2.525	3.170
andrews	2.012	2.611	3.276
bisquare	2.011	2.611	3.274
cauchy	2.001	2.589	3.236
fair	1.996	2.560	3.222
huber	1.997	2.564	3.223
logistic	1.999	2.566	3.227
talwar	1.986	2.609	3.225
welsch	2.007	2.609	3.254
mean	1.9989	2.5826	3.2341
variance	0.00011086	0.00093725	0.001032361

Table 3.6: The correlation dimension for all the nine methods and for the proposed 5-D distance weighting function.

For the validation of the proposed approach on natural color images, we chose three natural color texture images from Figure 3.4. The obtained $C(\delta)$ curves are presented in Figure 3.17 in a log-log space, all three curves being well separated according to the perceived complexity of images and converging to the same upper limit, given that all (i, j) pairs obey $|X_i - X_j| \leq \delta$ for large values of δ .

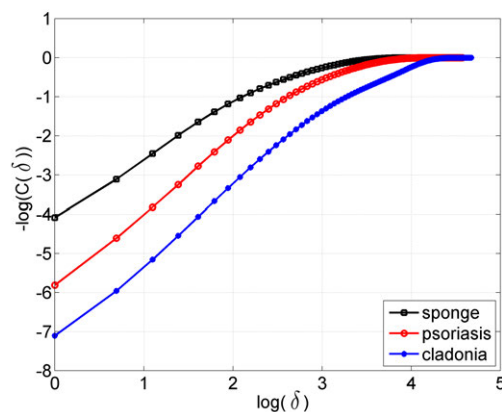


Fig. 3.17: The $C(\delta)$ curves for images in Fig. 3.4.

image	without weighting		with weighting	
	mean	variance	mean	variance
sponge	0.3910	0.0275	1.1096	0.000107
psoriasis	0.6326	0.0501	1.6094	0.000589
cladonia	1.1077	0.0279	1.8692	0.000502

Table 3.7: The mean and variance of correlation dimension for the three natural color images.

The impact on the estimated fractal dimension of the weighting function

can be seen in Table 3.7: once more the correct ranking is obtained, in accordance with the perceived complexity of these images. The impact of using the 5D distance can be seen in Table 3.8.

image	without weighting		with weighting	
	mean	variance	mean	variance
sponge	1.1988	0.1821	2.3440	0.0139
psoriasis	1.5023	0.1603	2.5007	0.0095
cladonia	1.7958	0.1207	2.6130	0.0070

Table 3.8: The mean and variance of correlation dimension for the 5D distance case.

For the future work, one may consider performing a comparison on the behaviour of the correlation dimension when different color distances, given the existence of ΔE_{94} and ΔE_{2000} with an improved behaviour for small color distances. And an extension to the multispectral domain.

3.2.4 Covering blanket

Another way to estimate the Hausdorff dimension is the *covering blanket* approach. This is based on the proposal of Minkowski of computing the length L of a curve F by dilating it using a disk of radius ε , followed by the computation of the area $A(\varepsilon)$ of the dilated set. The length will be equal to:

$$L(F) = \lim_{\varepsilon \searrow 0} \frac{A(\varepsilon)}{2\varepsilon}. \quad (3.19)$$

If the function F is a fractal, then the length varies as a function of ε :

$$L_\varepsilon(F) = c \lim_{\varepsilon \searrow 0} \varepsilon^{(1-\dim_{MB}F)} \quad (3.20)$$

where c is a constant and $\dim_{MB}F$ represents the Minkowski-Bouligand dimension of the object F . This can be computed by replacing the length $L_\varepsilon(F)$ from eq. (3.20) with the one given by eq. (3.19):

$$\lim_{\varepsilon \searrow 0} \frac{A(\varepsilon)}{2\varepsilon} = c \lim_{\varepsilon \searrow 0} \varepsilon^{(1-\dim_{MB}F)} \quad (3.21)$$

Without the limit, we obtain:

$$A(\varepsilon) = 2c\varepsilon^{(2-\dim_{MB}F)} \quad (3.22)$$

And by applying the logarithm, it gives:

$$\log A(\varepsilon) = \log(2c) + (2 - \dim_{MB}F) \log \varepsilon \quad (3.23)$$

$$\dim_{MB}F = \frac{\log(2c)}{\log \varepsilon} + 2 - \frac{\log A(\varepsilon)}{\log \varepsilon} \quad (3.24)$$

But $\varepsilon \searrow 0$ and therefore $\frac{\log(2c)}{\log \varepsilon} \nearrow 0$. Consequently, the definition of the dimension proposed by Bouligand [15] is:

$$\dim_{MB} F = \lim_{\varepsilon \searrow 0} \left(2 - \frac{\log A(\varepsilon)}{\log \varepsilon} \right) \quad (3.25)$$

The notion was extended to the computation of the fractal dimension of fractal objects in \mathbb{R}^n [79]:

$$\dim_{MB} F = \lim_{\varepsilon \searrow 0} \left(\dim_T F + 1 - \frac{\log V(\varepsilon)}{\log \varepsilon} \right) \quad (3.26)$$

where $\dim_T F$ represents the topological dimension of the fractal object $F \in \mathbb{R}^n$ and $V(\varepsilon)$ is the hypervolume envelopping the fractal object at a distance ε .

For the analysis of signal and images, this technique was formalized using mathematical morphology, thus resulting the covering blanket approach [94] [81]. In the Chapter 4, section 4.3 we present our approach of covering blanket for color images and results of fractal dimension estimation.

3.3 Lacunarity

Lacunarity is fractal measure very useful for the multi-scale analysis of the images that exhibit fractal properties, being complementary to the fractal dimension. Mandelbrot realized that the fractal dimension itself is not enough to completely describe the complexity of fractal sets [79]. Therefore, he introduced the concept of lacunarity, as a complementary metric. Lacunarity is a measure that characterizes the way in which the fractal set occupies the available topological space. It is a mass distribution function by definition. Historically, after the definition of Mandelbrot, the definition of Voss soon followed [123] [26].

Together with the fractal dimension, the lacunarity is usually used as a metric for the discrimination between images exhibiting fractal properties, like textures [26] [43]. They are mainly used to characterize, classify or to segment images or regions. For the computation of lacunarity there exist several approaches, the probabilistic algorithm being accepted as the most elegant approach. However, all the existing methods are defined for one dimensional signals or binary images with extension to gray-scale images. We present a color expression of the lacunarity based on the probabilistic algorithm for the computation of the fractal dimension.

According to the definition of Voss, lacunarity is the *entropy* of the points of the discrete surface representing the image, in other words the *dance* of the luminosity on the z axis. In our color approach, lacunarity characterizes the spread of vectors in the RGB space and represents a measure of the correlation between colors represented in the RGB color model. In most of

the approaches, including the probabilistic algorithm defined by Voss [123] the image is considered to be a set of points in a Euclidian space. The spacial arrangement of the pixels of the image is characterized by the probability matrix $P(m, \delta)$ of having m points included into a box of size δ centered in an arbitrary point of the image, as previously defined in eq. (3.11) regarding the number of boxes in the context of the probabilistic box-counting estimation (Section 3.2.2).

The lacunarity, as defined by Voss, is based on the first and second order moments computed using the probabilities $P(m, \delta)$:

$$M(\delta) = \sum_{m=1}^N mP(m, \delta) \quad M^2(\delta) = \sum_{m=1}^N m^2P(m, \delta) \quad (3.27)$$

$$\Lambda(\delta) = \frac{M^2(\delta) - (M(\delta))^2}{(M(\delta))^2} \quad (3.28)$$

We model the color images in the same way we showed in Section 3.2.2, thus we deal with a 5-dimensional Euclidian hyper-space and each pixel is a vector (x, y, r, g, b) . The classical algorithm of Voss defines cubes of size δ centered in the current pixel and counts the number of pixels that fall inside a cube of size δ . We generalize this by counting the pixels for which the Minkowski infinity norm distance is smaller than δ (see eq. 3.13). Practically, for a certain square of size δ in the (x, y) plane, we count the number of pixels that fall inside a 3-dimensional RGB cube of size δ , centered in the current pixel.

We show in Figure 3.18 the lacunarity curves we obtain for three kind of color texture images: three synthetic color fractal images from Figure 2.3, three natural fractal images from Figure 3.4 and three color texture images from VisTex in Figure 3.10.

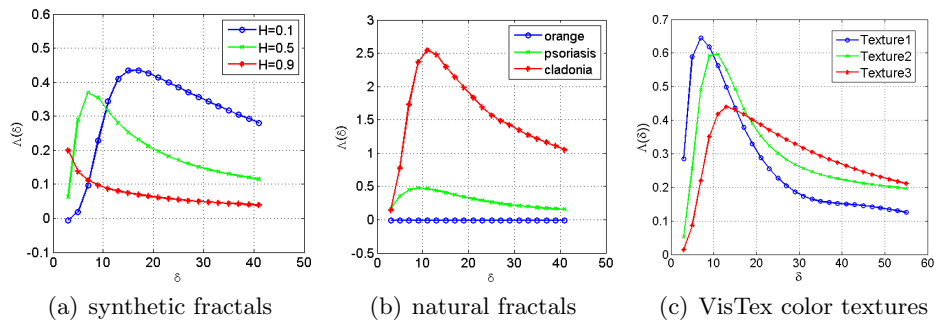


Fig. 3.18: Lacunarity curves.

As the fractal dimension is linked to the texture complexity, the lacunarity is correlated to the surface evolution which *supports* the signal evolution.

As expressed by Mandelbrot, the lacunarity is relative to the perception of *mounts* and *valleys* in the texture complexity. For instance, even if the color fractal image with $H = 0.9$ may seem complex visually due to its color content, its lacunarity is small due to low frequency variations. For the uniform color image *orange*, the dimension is 2.0 and the lacunarity is zero. For *psoriasis* the complexity is relatively small ($dim_B = 3.39$) and the lacunarity reveals the fact that the heterogeneity is exhibited for hyper-cubes of size between 7 and 21 pixels. For a more complex color image like *cladonia*, the lacunarity expresses the differences in spatial organization between different color zones (red, green, white). The examples show the additive property of the lacunarity and also explain the level difference in the lacunarity curves. For more details on validation and interpretation of the lacunarity see [62].

3.4 Limitations of current estimation techniques

We analyzed the evolution of the color fractal measures of the synthetic images in Figure 2.3 as a function of image resolution. Let us consider the color fractal image of middle complexity ($H = 0.5$) generated at various spatial resolutions: 256×256 , 512×512 , 1024×1024 , 2048×2048 and 4096×4096 presented in Figure 3.19.

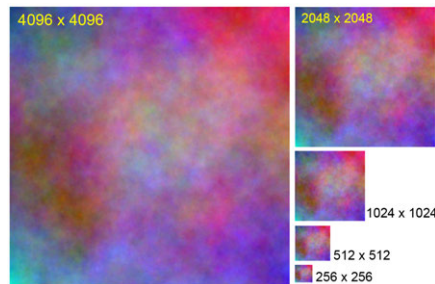


Fig. 3.19: Color fractal images of the same complexity, but different spatial resolutions.

All five images are correctly perceived by the human eye as being of the same complexity. Moreover, the normalized 3D RGB histograms from Figure 3.20 indicate that the color content is basically the same.

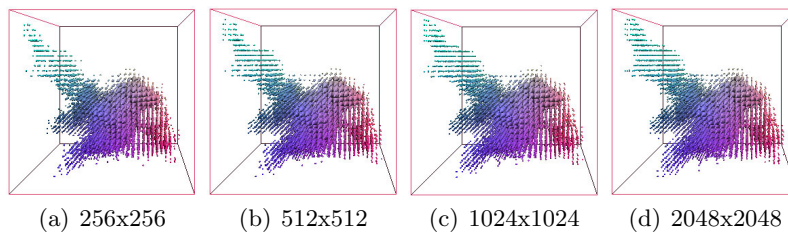


Fig. 3.20: 3D RGB histograms of images in Figure 3.19.

In Figure 3.21 we show the evolution of the color fractal dimension and the color lacunarity curves for the images in Figure 3.19 as a function of image resolution.

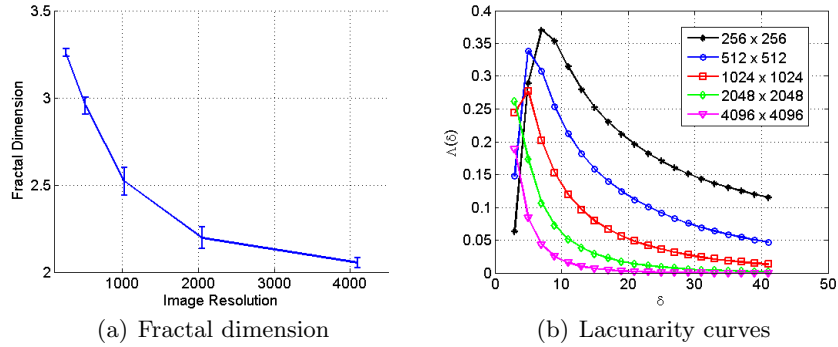


Fig. 3.21: Fractal dimension and lacunarity vs. image resolution.

One can notice that the estimated fractal dimension decreases with the increased resolution and the standard deviation indicates a bigger discrepancy between the results given by the nine estimation algorithms available in Matlab. Except for the 4096×4096 image resolution for which the standard deviation is very small, but this is the consequence of the fact that the estimated fractal dimension is close to 2.0—corresponding to a plane—i.e. the grasped fractal complexity is very low with the *standard* boxes (cubes). Clearly, the highest resolution image doesn't not have a complexity close to 2.0, fact misindicated also by the lacunarity curves.

In Figure 3.22 we plot the corresponding $N(\delta)$ curves which clearly show that the estimation of the texture complexity differs as a function of image resolution.

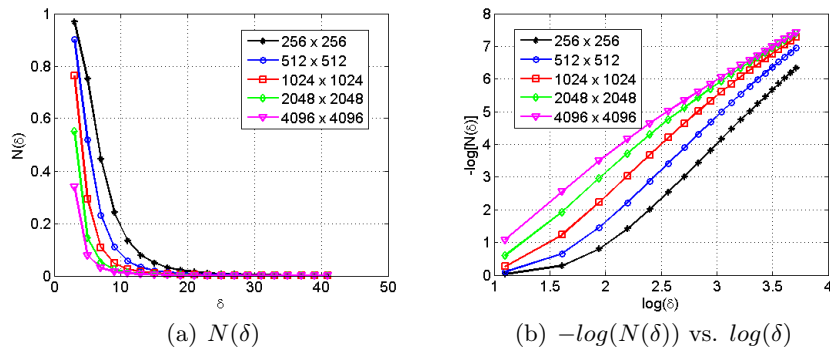


Fig. 3.22: $N(\delta)$ curves for different resolutions of the same fractal image.

The underestimation is confirmed by the texture complexity analysis performed using cooccurrence matrices. We performed a marginal analysis, per

each color plane. In Figure 3.23 we show the overlaid cooccurrence matrices computed on each color plane in RGB for pairs of adjacent pixels. As the image resolution increases, the cooccurrence matrices indicate a decreasing complexity.

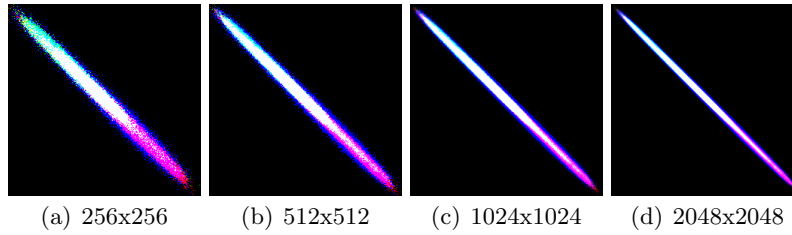


Fig. 3.23: Overlaid RGB cooccurrence matrices.

For the fractional Brownian motion – the underlying model used for the generation of the color fractal images in Figure 3.20 – it is known that the pixel values $V_H(t)$ exhibit a statistical scaling behaviour: if the time scale t is changed by a factor r , then the increments ΔV_H change by a factor r^H , where H is the Hurst factor used to control the complexity:

$$\langle \Delta V_H(rt)^2 \rangle \propto r^{2H} \langle \Delta V_H(t)^2 \rangle \quad (3.29)$$

If we consider the 256×256 fractal image as the original image, then the 2048×2048 can be considered to be scaled by a factor $r = 8$, and given that $H = 0.5$, the resulting scaling factor for the values is $\sqrt{8} \approx 3$. The scaling factor is used to adapt the size of the analysis boxes which become parallepipeds of size $r\delta$. In Figure 3.24 we show how the fractal dimension estimation improves on three of the scaled images as a function of the scaling / zoom factor.

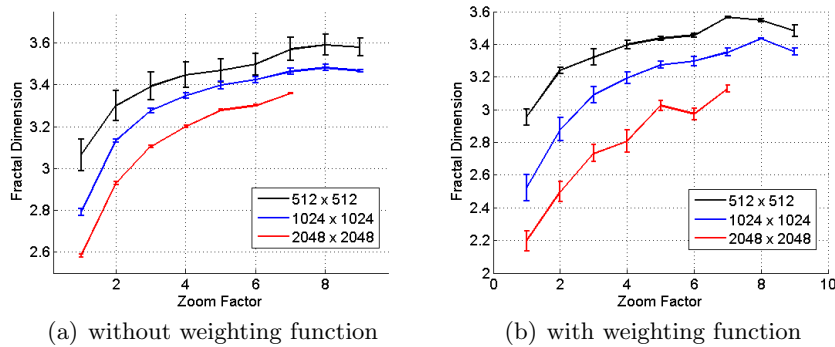


Fig. 3.24: Estimated fractal dimension for various scaling/zoom factors.

The adaptation is mandatory in order to correctly estimate the fractal dimension and to overcome the underestimation of the image complexity. If

we knew the zoom factor, than we could adapt the complexity assessment tools in order to correctly measure the image complexity. Unfortunately, for a given image we don't know the scale factor, and in addition, we don't know H which is the parameter we actually want to estimate!

3.5 An equivalent estimation approach

For the synthetic color fractal images we analyzed the vectorial (r, g, b) increments by computing the 3D RGB histograms of the differences between a pixel and its adjacent right neighbour. These histograms show the dependancy of the color increments on the Hurst coefficient, and the Gaussian shape of the represented distribution. This kind of statistical analysis is in fact another way to estimate the Hurst factor H for fractal objects. For a fractional Brownian motion, the increments obey the following relation [96]:

$$\overline{|X(t_i + \Delta_i) - X(t_i)|^2} = C^2 |\Delta_i|^{2H} \quad (3.30)$$

where C is a positive constant different from zero.

The 3D RGB histograms of the increments for the color fractal images allow to grasp the complexity of the color texture, i.e. the statistical complexity between the RGB planes. If visually, in a qualitative manner, there is a relationship between the size of the cloud in the 3D histogram, there must be a quantitative relationship as well. We propose the following approach: to compute the 3D RGB difference histogram (e.g. for the right neighbor), then use PCA (Principle Component Analysis) in order to determine the main direction of the cloud of points, then compute the volume of the cloud of points in two ways: $\Delta x \times \Delta y \times \Delta z$ to take into consideration the whole cloud or $\sigma_x \times \sigma_y \times \sigma_z$ for the core of the cloud, as illustrated in Figure 3.25.

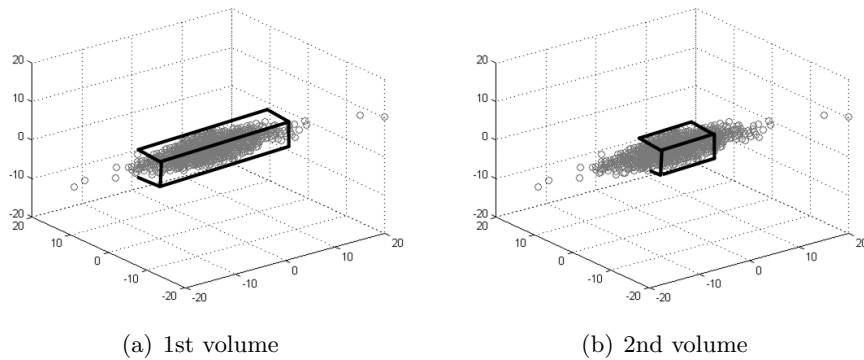


Fig. 3.25: Volume definitions.

The algorithm is illustrated in Figure 3.26 for a color texture image representing a human skin sample.

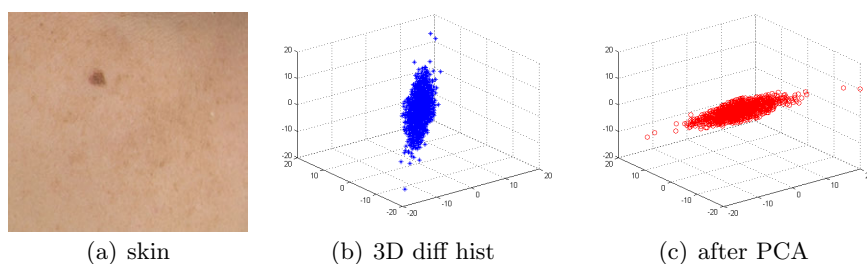


Fig. 3.26: Algorithm illustration.

For synthetic color fractal images in Figure 2.3, the *clouds* of points of the 3D RGB histogram are presented in Figure 3.27.

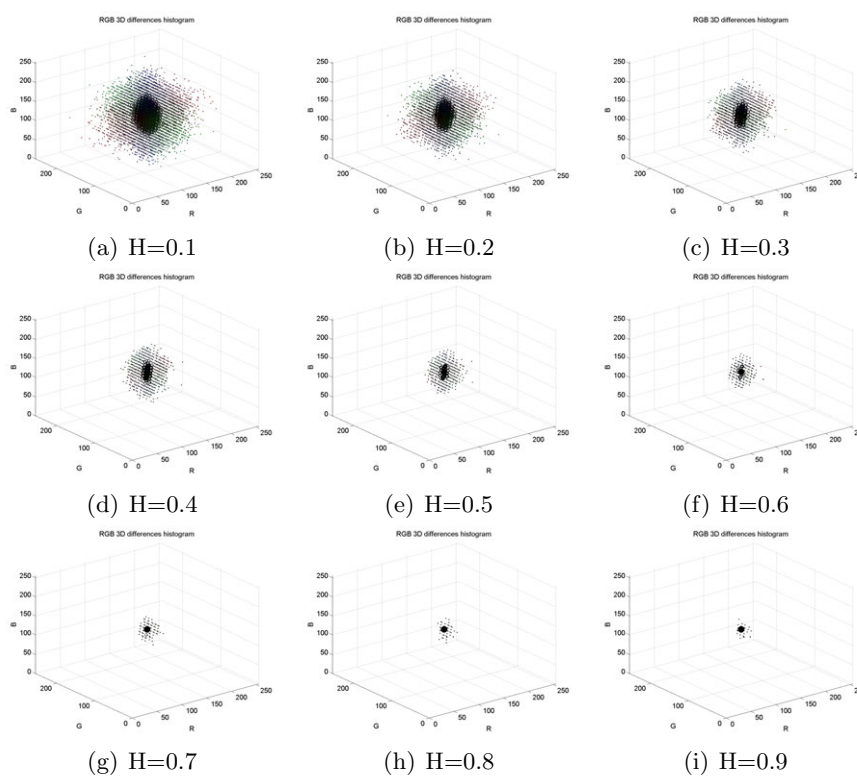


Fig. 3.27: Results synthetic color fractals.

The relationship between the computed volume and the estimated probabilistic box-counting color fractal dimension is presented in Figure 3.28.

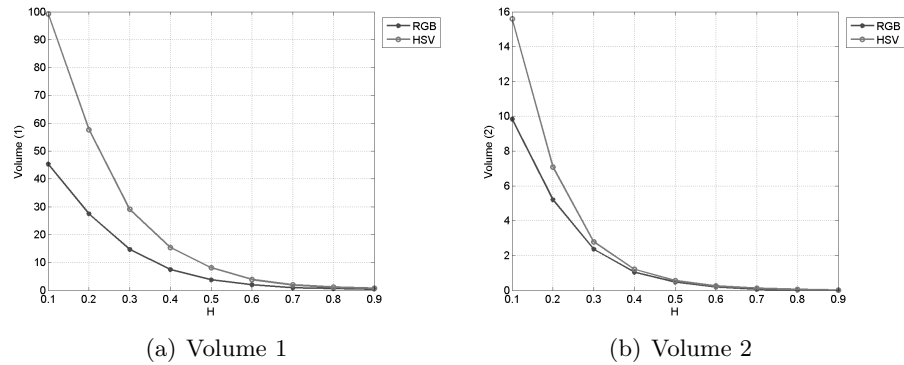


Fig. 3.28: Results synthetic color fractals.

For a set of 72 texture representing skin samples the following dependency between the estimated color fractal dimension using the probabilistic box-counting approach and the computed volumes. The curves are not linear, as one can see in Figure 3.29, but their analytic expression can be inferred.

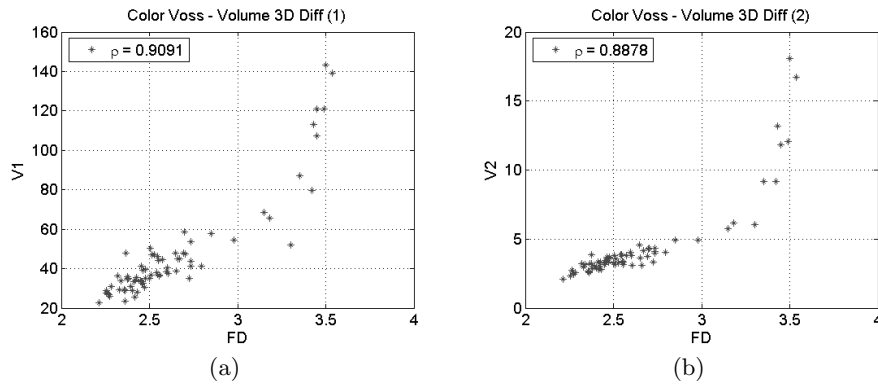


Fig. 3.29: Results on the set of 72 skin images.

The estimation based on the volume of vector increments is faster than the probabilistic box-counting approach, despite the PCA. However, PCA is mandatory for correctly estimating the volume of the clouds. Without the PCA, the complexity may seem larger than it is. The approach we present works for various color textures, both synthetic or natural, and in general for any color image for which the 3D difference histograms exhibit an elipsoidal shape (i.e. only one mode) - which is the hypothesis in our experiments.

Chapter 4

Morphological features

The features presented in this chapter fall within the framework of mathematical morphology (MM). This domain of mathematics was founded by Matheron [83] and Serra [110] and constitutes a popular non-linear image processing and analysis framework. MM was introduced for binary images, the basic morphological operators being based on set theory [47]. The MM extension to grayscale images is based on lattice theory, which implies a partial ordering of the image data, such that an *infimum* and a *supremum* exist for any subset of pixel values. The lattice structure perfectly fits the natural ordering of real numbers, offering the possibility to define the morphological operators for grayscale images. The extension to grayscale opened the doors to more complex operations like filtering, segmentation or texture analysis [114].

The extension of MM to color and multispectral images is not straightforward because of the vector image data, and consequently because of the need to define a suitable ordering for vector data. Ordering schemes for vector data have been classified in four groups [11]: marginal, reduced, conditional and partial, each having its advantages and disadvantages, depending on their outcome with respect to application. For example, marginal ordering introduces false colors and conditional ordering generates visual non-linearities from a perceptual point of view [60]; reduced and partial orderings are either relying on pre-orderings, thus lacking anti-symmetry, or have a behavior similar to conditional orderings, generating perceptual non-linearities. Various approaches have been proposed for color and multivariate MM [5], but none of them has been generally accepted as the *standard* approach. A series of morphological frameworks for vector data have been proposed recently: one using the color data distribution in a partial ordering based on depth functions [122], a reduced ordering through a graph-based approach using the Laplacian eigenmaps as a method for non-linear dimensionality reduction [75], or a geometrical method based on the Loewner order [16].

On a parallel scientific path to the morphological approaches, where the operators respect all the mathematical properties of the classical MM, various *pseudo-morphologies* have also been proposed. These frameworks do not require an underlying ordering of the image data, instead they focus on computing the two extrema of a given set [51] [4] [17]. These approaches do not require a complete lattice structure, thus avoiding the definition of a binary partial ordering relation on the vectorial data. Consequently, the resulting operators do not respect the properties of the classical morphological operators. However, they could be of practical interest in various applications, such as texture classification, noise reduction or multispectral data processing [97] [7].

4.1 Mathematical morphology tools

4.1.1 Mathematical morphology for binary images

We recall briefly the basic operators used in binary MM. For their definition, we need to define the concept of *structuring element*. This represents a set, usually much smaller compared to the image, used to extract information out of the analyzed image. The structuring element (SE) has an origin, size and shape, and it can be placed anywhere within the image support by using the translation. For a binary image F and the structuring element B , two fundamental operations for MM, the *erosion* $\varepsilon_B(F)$ and the *dilation* $\delta_B(F)$, are defined as follows:

$$\varepsilon_B(F) = \{x \mid B_x \subseteq F\} \quad (4.1)$$

$$\delta_B(F) = \{x \mid B_x \cap F \neq \emptyset\} \quad (4.2)$$

where B_x represents the structuring element B translated in the pixel x of the original image. In Figure 4.1 we show an example for a disk SE having a size larger than the size of the smallest elements in the original image. One may notice how the erosion eliminates the image elements which are smaller than the SE, while the dilation enlarges the objects and eliminates the spaces which are smaller than the SE. The two operations obey the property of *duality* [58]:

$$\varepsilon_B(F) = (\delta_B(F^C))^C \quad \text{and} \quad \delta_B(F) = (\varepsilon_B(F^C))^C \quad (4.3)$$

where F^C is the complement of image F .

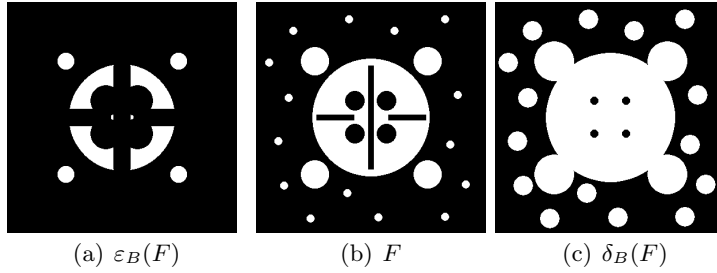


Fig. 4.1: Examples of erosion (left) and dilation (right) for a binary image.

The meaning of morphological erosion is that it removes all structures or objects that cannot contain the SE [114]. However, the erosion also shrinks the other objects within the image. Therefore, an operation that recovers most of the structures lost after erosion has been defined as the dilation of the previously eroded image; and vice-versa. The two resulting operations are called morphological *opening* $\gamma_B(F)$ and *closing* $\phi_B(F)$:

$$\gamma_B(F) = \delta_{\tilde{B}} [\varepsilon_B(F)] \quad (4.4)$$

$$\phi_B(F) = \varepsilon_{\tilde{B}} [\delta_B(F)] \quad (4.5)$$

where \tilde{B} represents the symmetric of B with respect to its origin. In Figure 4.2 we show the results of opening and closing for a binary image: the elements which were eliminated previously by the erosion or dilation cannot be recovered. Moreover, the narrow channels are removed by opening, while object which are closer will be joined by closing - as a function of SE size. For the large objects which are usually of interest within the image, the two operation will recover the initial size, together with smoothing the edges.

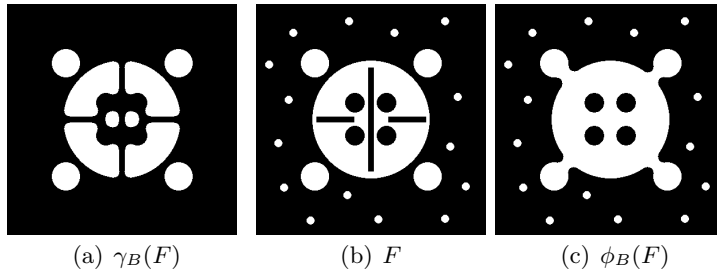


Fig. 4.2: Examples of opening (left) and closing (right) for a binary image.

The opening and closing are also dual operations:

$$\gamma_B(F) = (\phi_B(F^C))^C \quad \text{and} \quad \phi_B(F) = (\gamma_B(F^C))^C \quad (4.6)$$

In addition, they obey the property of *idempotency*, of extremely high importance for the signal processing context:

$$\gamma_B(\gamma_B(F)) = \gamma_B(F) \text{ and } \phi_B(\phi_B(F)) = \phi_B(F) \quad (4.7)$$

which means that applying one of the operation successively on the same image, using the same SE gives the same result as applying the operation just once. This property is most important for filtering, for example, because it guarantees that the goal of the operation was reached.

4.1.2 Mathematical morphology for gray-scale images

The extension to gray-scale of the operations previously defined was performed using the concept of *umbră* of a real function, which allows converting a function into a set and vice-versa [80] [55]. Let the following function f be $f : \mathcal{D}_f \rightarrow \mathbb{R}$, with $\mathcal{D}_f \subset \mathbb{R}^n$, then the *umbra* is defined as:

$$U(f) = \{(x, y) \in \mathbb{R}^{n+1} \mid x \in \mathcal{D}_f \text{ and } y \leq f(x)\} \quad (4.8)$$

$U(f)$ becomes thus a set of points in \mathbb{R}^{n+1} . In order to retrieve the function f , the *top* transform was defined for an $(n + 1)$ -dimensional set A :

$$T(A)(x) = \max \{y \mid (x, y) \in A, x \in A_{n-1}\} \quad (4.9)$$

where A_{n-1} represents the projection of A on its first $(n - 1)$ coordinates. The relationship between the two transforms, *top* and *umbra*, is: $T(U(f)) = f$. In Figure 4.3 the two transforms are illustrated for an arbitrary real function.

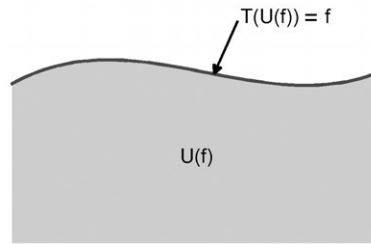


Fig. 4.3: The *umbra* and *top* transforms of a real function.

Extending the morphological operations to gray-scale image domain was done by transforming both the real function f representing the image and the structuring element (or function) g into sets:

$$\varepsilon_g(f) = \varepsilon_{U(g)}(U(f)) \quad (4.10)$$

$$\delta_g(f) = \delta_{U(g)}(U(f)) \quad (4.11)$$

A formalism for this operation was proposed by using the lattice theory [105]. A lattice \mathcal{L} is a set with a partial ordering where every non-empty subset $\mathcal{P} \subset \mathcal{L}$ has an *infimum* $\bigwedge \mathcal{P}$, and a *supremum* $\bigvee \mathcal{P}$ [34]. The *infimum* of a set is the largest element, smaller or equal to every element of that set, while the *supremum* is the smallest element which is larger or equal to the elements of that set. A binary relation \mathcal{R} is a *partial ordering* of the set \mathcal{S} if it respects the following properties [104]:

- reflexivity: $x\mathcal{R}x, \forall x \in \mathcal{S}$,
- transitivity: $x\mathcal{R}y$ and $y\mathcal{R}w \Rightarrow x\mathcal{R}w, \forall x, y, w \in \mathcal{S}$,
- antisymmetry: $x\mathcal{R}y$ and $y\mathcal{R}x \Rightarrow x = y, \forall x, y \in \mathcal{S}$.

If only the first two properties are obeyed then \mathcal{R} is called a *partial pre-ordering*. If additionally the total property is respected, i.e. every two elements can be compared, then the order is called a *total order*. There exist *total pre-orderings* which respect the reflexivity, transitivity and total properties.

One can associate to the set of real numbers \mathbb{R} a partial order \leq , with an *infimum*, $\bigwedge \mathcal{P}$ and a *supremum*, $\bigvee \mathcal{P}$, for any subset $\mathcal{P} \subset \mathbb{R}$. Consequently \mathbb{R} is a lattice and therefore the mathematical morphology operators can be applied to gray-scale images modelled with real functions $f : \mathcal{D}_f \rightarrow \mathcal{S} \subset \mathbb{R}$. For $f : \mathcal{D}_f \rightarrow \mathcal{S}$ and $g : \mathcal{D}_g \rightarrow \mathcal{S}$ where \mathcal{S} is a lattice, the erosion and dilation operations were defined as follows [58]:

$$[\varepsilon_g(f)](x) = \bigwedge_{z \in \mathcal{D}_g} (f(x+z) - g(z)), \quad \forall x \in \mathcal{D}_f \quad (4.12)$$

$$[\delta_g(f)](x) = \bigvee_{z \in \mathcal{D}_g} (f(x-z) + g(z)), \quad \forall x \in \mathcal{D}_f \quad (4.13)$$

where \bigwedge and \bigvee are the operators for computing the *infimum* and *supremum*. Very often *flat* structuring elements are used, which are defined as $g(x) = 0, \forall x \in \mathcal{D}_g$; these SEs are characterized only by origin, shape and size of the definition domain. In this case, the erosion and dilation operations become:

$$[\varepsilon_g(f)](x) = \bigwedge_{z \in \mathcal{D}_g} f(x+z), \quad \forall x \in \mathcal{D}_f \quad (4.14)$$

$$[\delta_g(f)](x) = \bigvee_{z \in \mathcal{D}_g} f(x-z), \quad \forall x \in \mathcal{D}_f \quad (4.15)$$

For the gray-scale images, the erosions and dilations with flat SE are equivalent to minimum and maximum rank filters. The opening and closing operations can also be defined for functions using equations (4.4) and (4.5). These operations are usually used for image filtering.

4.1.3 Applications and texture feature extraction

Starting from the four fundamental morphological operations, complex image analysis and feature extraction operations can be defined. The morphological gradient [102] was defined and is being used for edge detection in the context of image segmentation. Its definition is the following:

$$\rho_g(f) = \delta_g(f) - \varepsilon_g(f) \quad (4.16)$$

In Figure 4.4 we show its application on a gray-scale image, using a 3×3 square shaped SE.

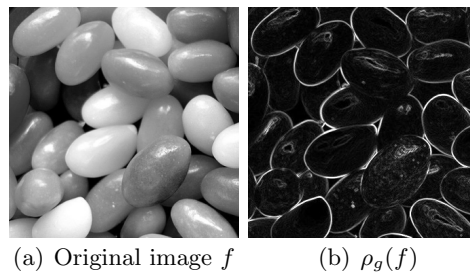


Fig. 4.4: Edge detection using morphological gradient.

Another application is the *covering blanket* approach. Serra proposed in [110] the usage of morphological erosion and dilation for producing envelopes for fractal objects, and implicitly for fractal images, with the purpose of estimating the Minkowski-Bouligand dimension. This idea was further developed in [94] and [81]. The goal of the covering blanket approach is to compute the volume of surfaces representing gray-scale images by using various sizes for the SE used to obtain the envelopes. The volume, computed for the SE g , is given by:

$$V_g(f) = \sum_{x \in \mathcal{D}_f} \{[\delta_g(f)](x) - [\varepsilon_g(f)](x)\} \quad (4.17)$$

By varying the size of SE, we can apply the equation 3.26 for the computation of the Minkowski-Bouligand dimension. In Figure 4.5 we show three fractal images of various complexity and the estimated Minkowski-Bouligand dimension. One can notice that a correct ranking of texture complexity can be obtained by estimation the MB dimension, allowing thus for further applications like classification and segmentation.

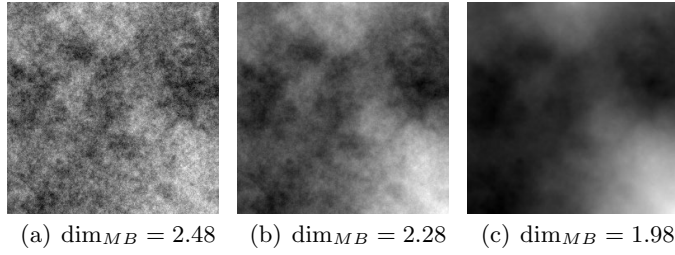


Fig. 4.5: Fractal images and their estimated MB dimension.

Two approaches of texture feature extraction, based on MM, have been also introduced by Serra: granulometry (or pattern spectrum) and morphological covariance [110]. Both approaches are based on the computation of the volume of images. We can consider gray-scale images as surfaces $z = f(x, y)$ in a 3D space. Consequently the volume of such surface, for the continuous case, can be computed as the integral over the definition domain:

$$V(f) = \iint_{\mathcal{D}_f} f(x, y) dx dy \quad (4.18)$$

For digital images represented as discrete surfaces, the volume becomes:

$$V(f) = \sum_{(i,j) \in \mathcal{D}_f} \sum f(i, j) \times 1 \times 1 = \sum_{(i,j) \in \mathcal{D}_f} f(i, j) \quad (4.19)$$

where $1 \times 1 = dx \times dy$ represents the size of one pixel. Therefore the volume of an image is the sum of all pixels.

By definition, the granulometry of an image f , using the SE g , is the function $[\Gamma_g(f)](n) = V_{\gamma_{ng}(f)}$, where ng represents the SE g magnified n times. In other words, the granulometry of an image is given by the evolution of the image volume after applying the opening operation, as a function of the SE size [114]. See Figure 4.6 for an example: the granulometry function is directly linked to the size distribution of the objects within images. This is why granulometry is also called *pattern spectrum*.

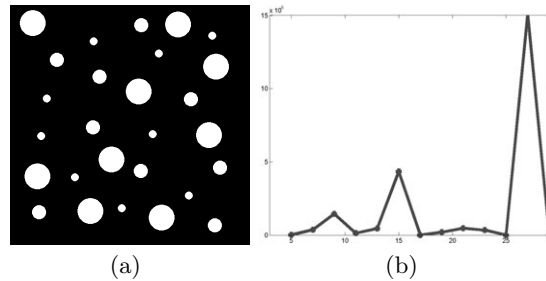


Fig. 4.6: Granulometry of a binary image.

Figure 4.7 shows three gray-scale texture images with the corresponding granulometry functions. The computed volumes are normed by the volume of the initial image, to enable a fair comparison. In [113] the notion of pseudo-granulometry was proposed, by using the morphological erosion instead of morphological opening: $[\Gamma'_g(f)](n) = V_{\varepsilon_{n,g}}(f)$.

The morphological covariance $K(f)$ of an image f is defined as the variation of the volume of the image after erosion using a SE of the form $P_{2,\vec{v}}$, representing a pair of points separated by a vector \vec{d} : $[K(f)][\vec{d}] = V_{\varepsilon_{P_{2,\vec{d}}}}$. Morphological covariance is a function of two variables: the vector's direction and its length. The classical approach in computing this function is to fix a direction for \vec{d} and to vary its length. Similar as for the definition of the cooccurrence matrix, the vector $\vec{d} = (dx, dy)$ determines the spatial relationship between the two points forming the SE. Computing this function for various orientation of the vector \vec{d} , one can obtain texture features that can be used for classification, indexing or segmentation. Figure 4.7(e) shows the morphological covariance vectors computed on the horizontal direction, using 20 values for the module of vector \vec{d} (from 1 to 20). Morphological covariance reflects the contrast on the analyzed direction, its variation being larger for Bark compared to Floor, while for Textil one may notice a certain periodicity. The same variation could be seen for Bark, if larger values for the vector size would be used.

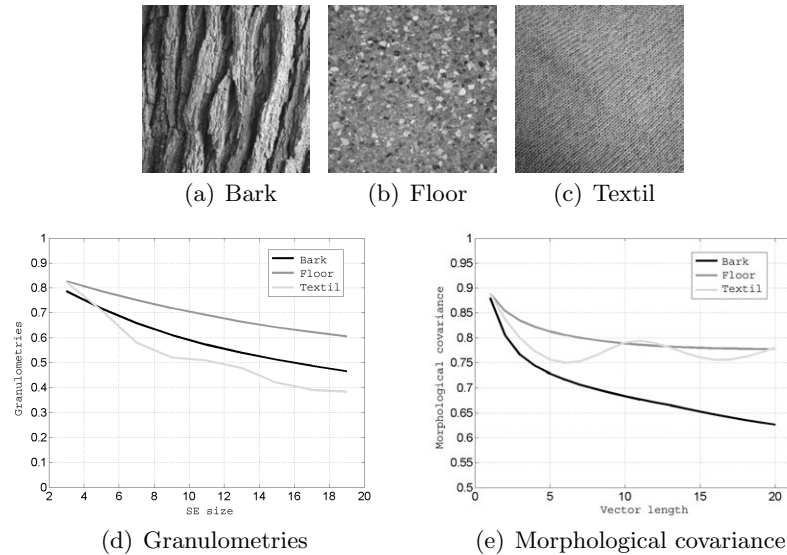


Fig. 4.7: Three textures (a, b, c) and their granulometries (d) and morphological covariance (e).

Defined within the grayscale framework, all these morphological tools may be applied locally in a straightforward manner, using a sliding window,

resulting in two feature vectors for each pixel (one for granulometry and the other for morphological covariance), which may be used in texture classification. Image segmentation, for instance, can be performed by taking into consideration such local texture features [114]. However, the application of these approaches to multivariate images is not straightforward, since erosion and dilation are based on pixel ordering, which is not a trivial problem for vector data.

4.1.4 Mathematical morphology for color images

Color images are vector functions $\mathcal{S} \subset \mathbb{R}^3$ and in order to use mathematical morphology it is mandatory to define a partial order for vector data. In [11] the vector orders were classified in four classes: type M (marginal), type R (reduced), type P (partial) and type C (conditional).

Type M ordering is performed on every component of the vectors:

$$\forall \mathbf{v}, \mathbf{v}' \in \mathbb{R}^n, \mathbf{v} < \mathbf{v}' \Leftrightarrow v_i < v'_i, \forall i \in \{1, \dots, n\} \quad (4.20)$$

where v_i is the i^{th} component of vector \mathbf{v} . There exist situations when vectors cannot be compared, for instance the vectors $\mathbf{u}, \mathbf{w} \in \mathbb{R}^n$, for which it exist $u_i < w_i$ and $w_j < u_j$ with $i, j \in \{1, \dots, n\}$. If one wishes to construct an *infimum* and a *supremum* for a set using this type of ordering, the two extrema may not belong to the initial set. For instance, for the set of two vectors $\mathcal{P} = \{[1, 2]; [2, 1]\}$, the extrema are $\bigwedge \mathcal{P} = [1, 1]$ and $\bigvee \mathcal{P} = [2, 2]$, none of them belonging to the initial set \mathcal{P} . In the context of color images, this issue is referred to as *false colors* – colors which do not belong to the initial image. However, this type of order is used for various approaches of MM for color images, the resulting operators being used for segmentation or object tracking [49].

Type R ordering . In this case, vectors are reduced to scalar values and then ordered. The reduction is usually performed through a transformation $h : \mathbb{R}^n \rightarrow \mathbb{R}$, used for ordering two vectors \mathbf{v} and \mathbf{v}' as follows:

$$\forall \mathbf{v}, \mathbf{v}' \in \mathbb{R}^n, \mathbf{v} < \mathbf{v}' \Leftrightarrow h(\mathbf{v}) < h(\mathbf{v}'). \quad (4.21)$$

Very often the transformation h is not injective. For instance, [30] uses a linear combination of the vector components and [39] proposes the sum of distances between a vector and the rest of the set. The disadvantage of this approach relies in the fact that for different vectors the same scalar value may result, which implies that the two vectors are considered identical. Consequently the antisymmetry property is not obeyed, therefore the R type orderings are pre-orderings. In order to obtain an order which can be used for MM operations an additional condition is required. For instance, in [30]

the position of vectors within the SE is used, while in [39] another type of order is used (type C) to avoid any ambiguity. If the h transform is injective, then all the aforementioned issues are overcome.

Type P ordering consists of partitioning the vector set into equivalent subsets that can be ordered according to a certain criterion. An example is given by splitting the probability density function of the vector data into convex hulls: the rank of each vector is given by the position of the convex hull to which it belongs, with respect to the center of the distribution. Such an approach was proposed in [121] by using a depth function.

Type C ordering is based on certain components of the vector, chosen and prioritized as a function of pre-determined criteria. The ordering of vector data is performed based on the first chosen component - if the value is the same for the vectors to be ordered, the next component is considered and so on:

$$\forall \mathbf{v}, \mathbf{v}' \in \mathbb{R}^n, \mathbf{v} < \mathbf{v}' \Leftrightarrow \exists i \in \{1, \dots, m\}, m \leq n, \text{ so that} \quad (4.22)$$

$$\forall j < i, v_j = v'_j, \text{ and } v_i < v'_i$$

If $m < n$ then a pre-ordering is generated when two or more vectors can be considered equal if they have the first m component equal [120]. If $m = n$, the ordering is called *lexicographic* and is a total ordering. The lexicographic order is very popular for extending the morphological operations to the color image domain [78] [50] [52]. One of the disadvantages is the need to impose a priority between the vector components, which is inappropriate for various color spaces. For example, in RGB all three components have the same importance and difficult to establish a priority between them.

This type of ordering is considered when between the components of the color space one can establish an evident priority: such color spaces are the ones with one luminance and two chrominance components (e.g. HLS, CIELAB), for which the luminance can have the highest importance, since the human visual system is more sensitive to changes in intensity, rather than in chrominance. An example of such use case is [3].

Another disadvantage is that it generates perceptual nonlinearities [119]. Consider the following example (RGB, 8 bits per channel): if R has the highest priority, followed by G and B, the following order will be generated for three colors: $(0, 0, 255)$  $< (0, 255, 0)$  $< (1, 0, 255)$ , which evidently exhibits a nonlinearity from human perception point of view, the two shades of blue being almost identical.

4.2 Pseudo-morphologies

Besides the attempts to extend the morphological operations to the color domain by using the order relations between vectors previously presented, there exist approaches that aim at computing the *infimum* and *supremum* of a given set without imposing an order. Such an approach is called *pseudo-morphology* because it doesn't fit into the classical framework of mathematical morphology, by not using the lattice structure. Consequently, some properties are not respected. For example, if one uses only the statistical distribution for defining an order, that order may lack transitivity. Generally speaking, pseudo-morphologies do not obey all the properties of the classical gray-scale mathematical morphology, like duality between erosion and dilation or idempotence. Despite that fact, pseudo-morphologies may have practical application: in [51] authors propose a pseudo-morphology based on the Hue component from the HLS color space which is used for texture analysis. In [7] vectors are ordered based on one of their component and a parameter called $\alpha \in (0, 1)$ is used to determine the percentage of vectors being selected, then the selected vectors are ordered based on the second component and so on so forth. This approach is called α -*trimmed* and it is used for image filtering and texture classification.

4.2.1 Probabilistic pseudo-morphology

In [60] we proposed the estimation of *infimum* and *supremum* by using the Chebyshev inequality, which allows estimating the probability of a subset of vectors to belong to an interval centered around the mean of the distribution [25]. Let ξ be a random variable with mean μ_ξ and standard deviation σ_ξ , then the Chebyshev inequality states that:

$$P\{|\xi - \mu_\xi| \geq k\sigma_\xi\} \leq \frac{1}{k^2} \quad (4.23)$$

Eq. (4.23) stands for any distribution with finite mean and standard deviation [91]. Using the k parameter, one may generate symmetric intervals around the mean, with the two extrema being closed to the minimum or maximum value as a function of value k . The two extrema that give the limits of those intervals are specified by eq. (4.24). Consequently we define the probabilistic pseudo-extrema of a distribution, \mathcal{E}^+ and \mathcal{E}^- , as specified by Chebyshev inequality:

$$\begin{cases} \mathcal{E}^+ \triangleq \mu_\xi + k\sigma_\xi \\ \mathcal{E}^- \triangleq \mu_\xi - k\sigma_\xi \end{cases} \quad (4.24)$$

By choosing an appropriate value for k , the error between the probabilistic extrema and the real extrema of a distribution can be reduced as desired.

This error, however, cannot be zero due to the fact that the real minimum and maximum are not symmetric with respect to the mean.

In [17] we used this approach to propose a probabilistic pseudo-morphology (PPM) for grayscale images. Given an image $f : \mathcal{D}_f \rightarrow \mathcal{S} \subset \mathbb{R}$, and a flat SE g having the support \mathcal{D}_g , we defined the pseudo-erosion and pseudo-dilation operations as follows:

$$[\varepsilon_g(f)](x) = \bigwedge_{z \in \mathcal{D}_g} f(x+z) \triangleq \mu_\xi - k\sigma_\xi, \quad \forall x \in \mathcal{D}_f \quad (4.25)$$

$$[\delta_g(f)](x) = \bigvee_{z \in \mathcal{D}_g} f(x-z) \triangleq \mu_\xi + k\sigma_\xi, \quad \forall x \in \mathcal{D}_f \quad (4.26)$$

where ξ represents a random variable which models the gray level of pixels falling within $\mathcal{D}_f \cap \mathcal{D}_g$. Thus the mean μ_ξ and standard deviation σ_ξ are computed locally, within a neighborhood given by the size and position of the SE. The value of parameter k can be determined globally, for example based on image histogram, which is an estimate of the probability density function of the random variable ξ . For instance, for Lena image, a k value around 2 gives the smallest extrema estimation error [17] and the probabilistic extrema are closest to the real extrema computed within the framework of the classical gray-level mathematical morphology (GLMM). According to Chebyshev inequality, for $k = 2$, there exists a probability smaller than 25% that any pixel value can be outside the interval determined by the probabilistic extrema. However, the shape of the distribution may have an impact to the estimation of the probabilistic extrema: if the 3rd order moment, the *skewness*, is large, then one the extrema falls within the interval of interest, while the other may be far away considerably. In what follows, we present a qualitative evaluation of the results for three different values of k .

$k = 0.2$ The probabilistic pseudo-extrema are close to the mean value and consequently the behaviour of the PPM operations is similar to a smoothing filter (see Figures 4.8(a) and 4.9(a)), thus being close to linear filters rather than non-linear morphological ones.

$k = 2$ This is an optimum value for Lena image: by comparing the images in Figures 4.8(b) and 4.9(b) with the ones from Figures 4.8(d) and 4.9(d) one may observe the results are similar for PPM and GLMM. Some differences occur, naturally: the classical morphology introduces artefacts (e.g. top of the hat in Fig. 4.8(d)). Due to the intrinsic statistical filtering of PPM, the resulting pseudo-eroded image does not exhibit such artefacts, the shape of the SE not being visible. In addition, PPM is capable of preserving morphological details (e.g. nose and eyebrows in Figure 4.8(b)) and texture (e.g. hat feathers in Figure 4.9(b)). All these prove that PPM is less influenced

by the local noise, the morphological or textural structures being preserved better than GLMM.

$k = 4$ When k has such a large value, the probabilistic extrema are far away from the local mean, being pushed towards black and white, the extrema of gray-scale (Figures 4.8(c) and 4.9(c)). This case can be similar to classical MM using *non-flat* SE.

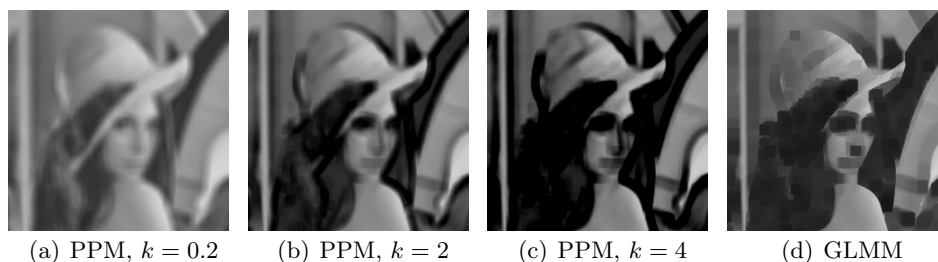


Fig. 4.8: PPM erosions for various values of k compared to GLMM, both using a flat SE of size 11×11 .

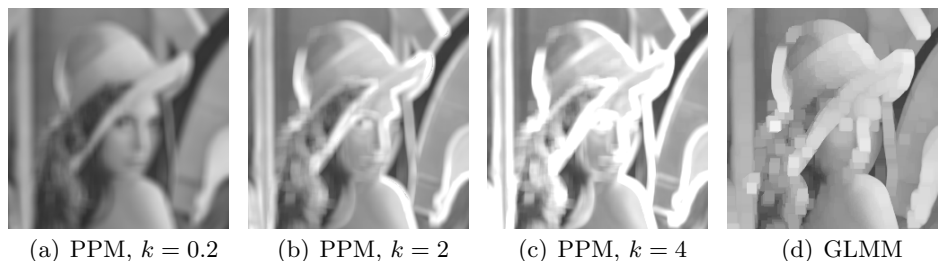


Fig. 4.9: PPM dilations for various values of k compared to GLMM, both using a flat SE of size 11×11 .

4.2.2 Probabilistic color pseudo-morphology

For color images the pixel values are vectors, the images being modeled as $f : \mathcal{D}_f \rightarrow \mathcal{S} \subset \mathbb{R}^3$. In order to extend PPM to color domain, we need to correctly evaluate the variance of the data, for the purpose of using the same Chebyshev inequality. In [17] we used the *Principal Component Analysis* (PCA) applied on the initial set of vectors representing pixel colors. PCA is a linear transformation of the data set which identifies a new space, i.e. a set of orthogonal directions, so that the variance is maximized on one of those directions [92]. The directions of the transformed space are the eigenvectors of the covariance matrix. The new coordinate system consists of new axes called principal components - the variance of data is maximum along the first component, smaller along the second, and so on so forth, the

variance being the smallest on the last principal component. For the RGB color space there is high correlation between components and consequently PCA is appropriate for assessing the variance of the data along the first principal components. Moreover, the probabilistic pseudo-extrema can be estimated along this first component using the Chebyshev inequality (4.24).

This approach is similar to using PCA for lossy data compression, when only the components with high variance are retained, ignoring the rest [66]. In addition, if one uses more components with relatively high variance of the data, the number of probabilistic pseudo-extrema increases, introducing ambiguity: if the first two components are used, then using the Chebyshev inequality, four pseudo-extrema will be generated. In Figure 4.10 this case is illustrated.

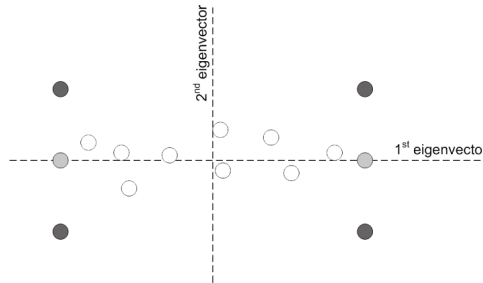


Fig. 4.10: Computing probabilistic pseudo-extrema of a bi-dimensional data set (white dots): using the first principal component (light gray dots) or using the first two principal components (dark gray dots).

However, this approach cannot be used straightforward, because after applying PCA there is still an issue to solve, due to the vector nature of data: the two extrema have to be ordered and labeled as minimum and maximum. For the gray-scale images, the two probabilistic extrema are implicitly ordered, based on the order of real values. PCA determines only the direction of the principal components without associating a sense to them. However, we still can establish an order between two points on a certain direction, if that directions has associated a sense. When PCA is used this sense cannot be associated automatically to every eigenvector because PCA is a linear transformation based on a rotation of the space and the rotation can be performed in two ways along a given axis. In [17] we ordered the pseudo-extrema constructed on the first principal component using 3 pairs of 3-dimensional reference points with an *a priori* order imposed or chosen for each pair. The same approach can be used for n -dimensional spaces and thus applied for multi- or hyper-spectral images as well. The ordering process is the following: the first pair of references determines an ordered direction from the smaller reference to the larger reference; the pseudo-extrema are projected on this direction and are being ordered based on the order of their

projections; if the two projections coincide (when the direction determined by the pseudo-extrema is perpendicular on the direction determined by the references) the next pair of reference points are used and so on so forth. The process is illustrated in Figure 4.11, where an *a priori* ordering is considered between the reference points $R^+ > R^-$ therefore the pseudo-extrema E_α and E_β obey the order $E_\alpha > E_\beta$.

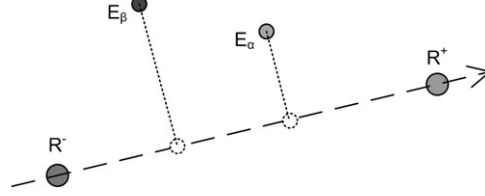


Fig. 4.11: Ordering E_α and E_β using the ordered references R^- and R^+ .

Using the same rationale, the probabilistic pseudo-morphology can be extended to multispectral images as well. The only issue is choosing the appropriate pairs of ordered references depending on application. In [18], the references were automatically computed as the global pseudo-extrema on each principal component determined on the entire color distribution of the image. In this way, three pairs of references were obtained: $(\mathcal{R}_1^-, \mathcal{R}_1^+)$, $(\mathcal{R}_2^-, \mathcal{R}_2^+)$, $(\mathcal{R}_3^-, \mathcal{R}_3^+)$, with $\mathcal{R}_i^- < \mathcal{R}_i^+$. The ordering of the references was performed by using their projections on the black-white axis. Using these references, the two pseudo-morphological operations, dilation and erosion, can be defined for color images (denoted f), for a structuring element g having the support \mathcal{D}_g , as follows:

$$\begin{aligned}
 [\varepsilon_g(f)](x) &= \bigwedge_{\substack{z \in \mathcal{D}_g \\ x \in \mathcal{D}_f}} f(x+z) \triangleq \\
 &= \begin{cases} \arg \min_i [\overrightarrow{\mathcal{R}_0^- \mathcal{R}_0^+} \cdot \overrightarrow{\mathcal{R}_0^- i}], i \in \{\mathcal{E}_\alpha, \mathcal{E}_\beta\} \\ \arg \min_i [\overrightarrow{\mathcal{R}_1^- \mathcal{R}_1^+} \cdot \overrightarrow{\mathcal{R}_1^- i}], i \in \{\mathcal{E}_\alpha, \mathcal{E}_\beta\} \text{ if } \overrightarrow{\mathcal{R}_0^- \mathcal{R}_0^+} \cdot \overrightarrow{\mathcal{E}_\alpha \mathcal{E}_\beta} = 0 \\ \arg \min_i [\overrightarrow{\mathcal{R}_2^- \mathcal{R}_2^+} \cdot \overrightarrow{\mathcal{R}_1^- i}], i \in \{\mathcal{E}_\alpha, \mathcal{E}_\beta\} \text{ if } \overrightarrow{\mathcal{R}_0^- \mathcal{R}_0^+} \cdot \overrightarrow{\mathcal{E}_\alpha \mathcal{E}_\beta} = \overrightarrow{\mathcal{R}_1^- \mathcal{R}_1^+} \cdot \overrightarrow{\mathcal{E}_\alpha \mathcal{E}_\beta} = 0 \end{cases} \quad (4.27)
 \end{aligned}$$

$$\begin{aligned}
 [\delta_g(f)](x) &= \bigvee_{\substack{z \in \mathcal{D}_g \\ x \in \mathcal{D}_f}} f(x-z) \triangleq \\
 &= \begin{cases} \arg \max_i [\overrightarrow{\mathcal{R}_0^- \mathcal{R}_0^+} \cdot \overrightarrow{\mathcal{R}_0^- i}], i \in \{\mathcal{E}_\alpha, \mathcal{E}_\beta\} \\ \arg \max_i [\overrightarrow{\mathcal{R}_1^- \mathcal{R}_1^+} \cdot \overrightarrow{\mathcal{R}_1^- i}], i \in \{\mathcal{E}_\alpha, \mathcal{E}_\beta\} \text{ if } \overrightarrow{\mathcal{R}_0^- \mathcal{R}_0^+} \cdot \overrightarrow{\mathcal{E}_\alpha \mathcal{E}_\beta} = 0 \\ \arg \max_i [\overrightarrow{\mathcal{R}_2^- \mathcal{R}_2^+} \cdot \overrightarrow{\mathcal{R}_1^- i}], i \in \{\mathcal{E}_\alpha, \mathcal{E}_\beta\} \text{ if } \overrightarrow{\mathcal{R}_0^- \mathcal{R}_0^+} \cdot \overrightarrow{\mathcal{E}_\alpha \mathcal{E}_\beta} = \overrightarrow{\mathcal{R}_1^- \mathcal{R}_1^+} \cdot \overrightarrow{\mathcal{E}_\alpha \mathcal{E}_\beta} = 0 \end{cases} \quad (4.28)
 \end{aligned}$$

where $\overrightarrow{\mathcal{R}_i^- \mathcal{R}_i^+}$ is the ordered direction determined the references \mathcal{R}_i^- and \mathcal{R}_i^+ , and \mathcal{E}_α and \mathcal{E}_β represent the local pseudo-extrema of the colors within the support of the structuring element. The steps of the algorithm are:

- step 1: determining the three pairs of references $(\mathcal{R}_{1\alpha}, \mathcal{R}_{1\beta})$, $(\mathcal{R}_{2\alpha}, \mathcal{R}_{2\beta})$, $(\mathcal{R}_{3\alpha}, \mathcal{R}_{3\beta})$ as the global pseudo-extrema generated for the entire image color distribution, using the Chebyshev inequality on each principal components;
- step 2: ordering the three pairs of references based on their projections on the back-white¹ direction (denoted \overrightarrow{BW}):

$$\mathcal{R}_{i\alpha} < \mathcal{R}_{i\beta} \text{ if } \overrightarrow{\mathcal{R}_{i\alpha} \mathcal{R}_{i\beta}} \cdot \overrightarrow{BW} \geq 0 \quad (4.29)$$

- step 3: estimating the local pseudo-extrema \mathcal{E}_α and \mathcal{E}_β using Chebyshev inequality applied on the first principal component (or the next ones, if the case) computed locally within the structuring element support;
- step 4: ordering the local pseudo-extrema and computation of the pseudo-dilation and erosion.

In Figure 4.12 few results using the PPM approach on the "Miro" image are presented. All operations were applied in RGB color space, since its components are highly correlated and thus using PCA makes sense.

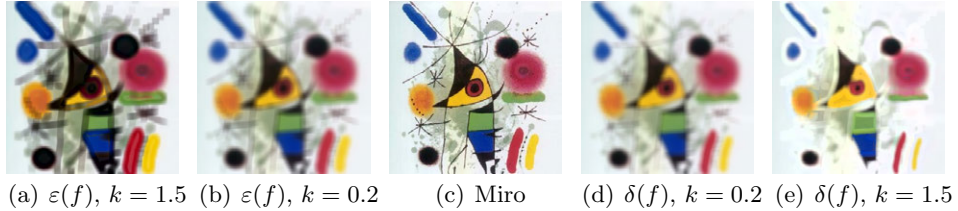


Fig. 4.12: Pseudo-erosion and dilation for "Miro" image using a flat SE size 11×11 and two values for the parameter k .

A similarity between the color and gray-scale approaches can be noticed:

- The pseudo-dilations make the image lighter, while pseudo-erosions make it darker, as a consequence of using the black-white axis for ordering the reference colors;
- A low-pass filtering effect is introduced, intrinsic to the statistical process being used; in addition, the local pseudo-extrema do not vary significantly for consecutive pixels while sweeping the structuring element over the image;

¹Depending on application, any other two colors can be chosen.

- The influence of the parameter k value of the Chebyshev inequality is similar: a small value determines a results similar to a smoothing filter, while a large value determines a non-linear behaviour; very large values can determine vectors outside the local distribution, or even outside the color space.

The defined pseudo-morphological operations can be used for edge detection, by computing the Beucher morphological gradient as the difference between the dilation and erosion. Figure 4.13 shows the results obtained in two cases: the marginal subtraction between pseudo-dilation and pseudo-erosion, thus the result is a color image 4.13(a)) and the Euclidian distance between pseudo-dilation and pseudo-erosion, thus the result is a grey-scale image 4.13(b)).

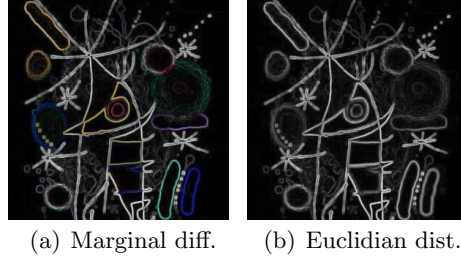


Fig. 4.13: Beucher gradient: marginal subtraction (a) and Euclidian distance (b) between pseudo-dilation and pseudo-erosion with a 3×3 SE.

Due to the estimation of pseudo-extrema using the Chebyshev inequality, the two vector values may not belong to the initial set, therefore *false colors* may appear. As k is larger, so the probability of introducing false colors. However, the two pseudo probabilistic operations obey the property of duality (see [60] for the demonstration). The opening and closing operations that could be constructed using the pseudo operators do not obey the idempotence (eq. 4.7).

4.2.3 Maximum distance pseudo-morphology

Given an image represented in the CIE Lab color space, $f : \mathcal{D}_f \rightarrow \mathbb{R}^3$, with the support $\mathcal{D}_f \subset \mathbb{Z}^2$, we define the two pseudo-extrema in the support \mathcal{D}_g of the flat structuring element (SE) g , as:

$$\{\mathbf{e}_a, \mathbf{e}_b\} = \arg \max_{f(i), f(j)} d(f(i), f(j)), \quad \forall i, j \in \mathcal{D}_f \cap \mathcal{D}_g \quad (4.30)$$

where $d(\cdot, \cdot)$ represents the CIE Lab ΔE distance [112]. The approach involves computing $\frac{N(N+1)}{2}$ distances between the pixels covered by the SE, where $N = \text{card}(\mathcal{D}_g)$.

After choosing the two pseudo-extrema for the local window, the issue of labeling them can be solved in various ways, as a function of the desired outcome of the pseudo-morphological operators. Labeling can be done based on distances to the black-white axis or to reference or convergence colors [17] [18]. In the present work, lexicographic ordering $<_\ell$ is used in order to label the two obtained values and define the pseudo-morphological operators:

$$\forall \mathbf{v}, \mathbf{v}' \in \mathbb{R}^n, \mathbf{v} <_\ell \mathbf{v}' \Leftrightarrow \exists i \in \{1, \dots, n\}, (\forall j < i, v_j = v'_j) \wedge (v_i < v'_i) \quad (4.31)$$

We define the *pseudo-erosion* as the minimum, in the lexicographical sense, of the two previously computed pseudo-extrema:

$$[\varepsilon_g(f)](k) = \min_\ell \{\mathbf{e}_a, \mathbf{e}_b\} \quad \forall k \in \mathcal{D}_f \quad (4.32)$$

The *pseudo-dilation* is defined as the lexicographic maximum of the pseudo-extrema:

$$[\delta_g(f)](k) = \max_\ell \{\mathbf{e}_a, \mathbf{e}_b\} \quad \forall k \in \mathcal{D}_f \quad (4.33)$$

The choice of using the CIE Lab color space instead of RGB for the definition of the pseudo-morphological operators is justified first of all by the visually similar results to classical morphology. Secondly, by the linearity of the space with respect to the ΔE distance, which ensures a low probability of encountering more than two points locally that satisfy condition (4.30).

For the practical implementation using the CIE Lab color space, in the lexicographic ordering of the pseudo-extrema, the order of the channels is L, a, b ; the L channel is prioritized, thus, generally, the minimum is *darker* and the maximum is *brighter*. Consequently, the behavior of the defined pseudo-morphological operators is similar to the classical fundamental operators (erosion darkens the image, dilation brightens it).

For multispectral images $f : \mathcal{D}_f \rightarrow \mathbb{R}^n$, we use the same definition for the pseudo-extrema, with the distance measure now representing the Euclidean distance in \mathbb{R}^n . The results of using lexicographic ordering to label the pseudo-extrema would have no relevance, thus we use a total pre-ordering $<_e$ based on pixel energy:

$$\forall \mathbf{v}, \mathbf{v}' \in \mathbb{R}^n, \mathbf{v} <_e \mathbf{v}' \Leftrightarrow \sum_{i=1}^n v_i^2 < \sum_{i=1}^n v'_i{}^2 \quad (4.34)$$

Thus we define the pseudo-erosion and pseudo-dilation for multispectral images as the minimum and the maximum, respectively, in the energy sense, of the two pseudo-extrema.

Figures 4.15 and 4.16 present the results of applying the color pseudo-erosion and pseudo-dilation operators with various SE sizes on the two color texture images from Figure 4.14 from CAVE² data-base, Columbia Univer-

²<http://www.cs.columbia.edu/CAVE/databases/multispectral/>

sity, New York. One may notice that the lighter features are increasing in size for the pseudo-dilation, as is the case with the darker features for the pseudo-erosion, this behavior being similar to the effect obtained through classical morphological operators.

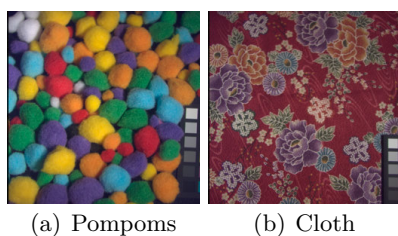


Fig. 4.14: Original multispectral images (rendered as RGB).

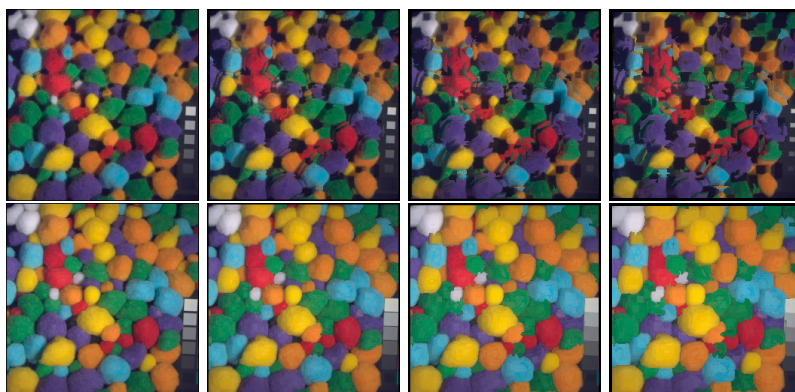


Fig. 4.15: Pompoms pseudo-erosions (top) and pseudo-dilations (bottom) for various SE sizes: 3×3 , 5×5 , 7×7 , 9×9 (left to right).



Fig. 4.16: Cloth pseudo-erosions (top) and pseudo-dilations (bottom) for various SE sizes: 3×3 , 5×5 , 7×7 , 9×9 (left to right).

The two images were also used for a qualitative assessment of pseudo-granulometry (4.36) and morphological covariance (4.39). We used three versions of the test images: grayscale, color and multispectral (31 channels). The length of the pseudo-granulometry vector is equal to the number of SE sizes used; morphological covariance was applied for 4 orientations of \vec{v} (0° , 45° , 90° and 135°), resulting in a feature vector with a length of four times the number of iterations for a given direction. Before plotting the images, the vectors were normed with the sum of all values in the vector.

4.3 Covering blanket

In Section 3.2.4 we presented the *covering-blanket* approach for fractal dimension estimation. The upper and lower covers can be obtained by morphological dilations and erosions. This expression is a reduced form of the complete expression from Maragos [81] and used by Soille in a first implementation of the algorithm [102]. This approach is used for the estimation of the Minkowski-Bouligand fractal dimension (eq. 3.26) of textures for the purpose of classification based on their estimated complexity. As previously shown in Section 3.2.2, color images can be modeled as 5-dimensional objects. Therefore the covering blanket approach raises the issue of computing the variation of the volume between the hyper-surfaces determined by the dilations and erosions of a color image for various sizes of the structuring element.

We compared the following morphology and pseudo-morphology frameworks to estimate the color fractal dimension of the color fractal images from Figure 2.3 using the covering blanket approach: (i) the probabilistic pseudo-morphology (PPM) described in Section 4.2.2; (ii) the pseudo-morphology based on the computation pseudo-extrema along the first principal component (PM.1PCA) [17] [18]; (iii) a morphology based on the lexicographic order (eq. 4.22) applied in HSV color space, with V having the largest priority, followed by S and H [78] and (iv) the α -trimmed pseudo-morphology [7] in RGB, with R having the largest priority, followed by G and B. The results are presented in Figure 4.17. Covering blanket using PPM gives the highest dynamic range, allowing for a better discrimination of textures based on their estimated complexity.

In Figure 4.18 (a) we compare the results we obtain for the gray-scale fractal images against the results we obtain by using covering blanket based on the classical morphology. The theoretical fractal dimension is plotted for reference. The fractal dimension is slightly over-estimated but the slope is almost the correct one when using our probabilistic approach, while for the classical morphology the fractal dimension is well under-estimated and the slope is different. We also performed the comparison (in Figure 4.18 (b)) between color covering blanket using PPM and the probabilistic box-

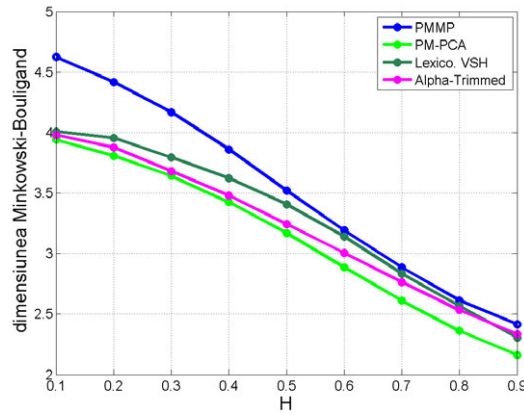


Fig. 4.17: Estimated Minkowski-Bouligand fractal dimension using covering blanket for color fractal images in Fig. 2.3.

counting estimation based on Voss’ expression. The comparison, plotted as mean values and standard deviation for a set of repeated experiments, shows the linearity of the behavior obtained by the color covering blanket approach, in particular for images of high complexity (small Hurst coefficient values). This property is clearly highly important to validate our approach for color image processing. More results of comparison can be found in [61].

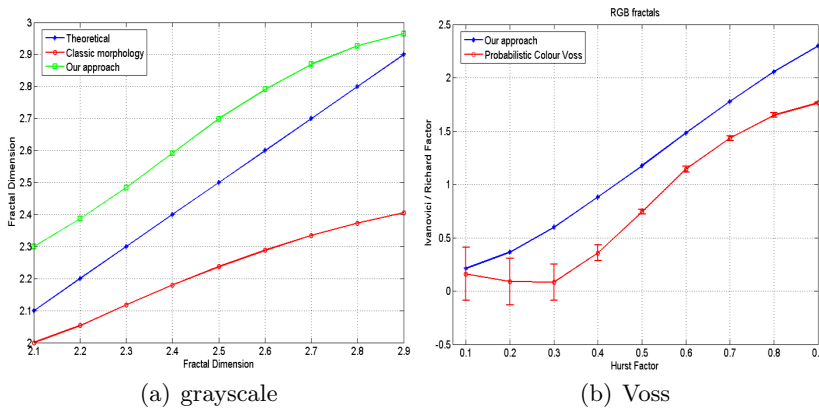


Fig. 4.18: Comparison against various estimation methods.

The approach based on PPM is not subject to the non linearity effects of vector ordering. Moreover, from a human visual perception point of view, the main issue of such an approach is the appearance of false colors, the consequence of the fact that the maximum and the minimum may not belong to the initial set, due to the way they are constructed. Further more, sometimes the extrema are outside the RGB color space, therefore

they cannot be rendered for display or print. Last but not least, we showed that color complexity can be measured in the RGB color space. Clearly enough, a bias is introduced by the color fractal generator, but nevertheless we used the color fractal images to validate the theoretical approach and the experimental implementation. The results showed that the statistical model embedded in the expression added robustness to the metrological process and this feature is extremely useful in the case of natural or noisy images.

4.4 Granulometry or pattern spectrum

The granulometry is an important feature based on opening and computing the volume of the image after applying the opening operator, as a function of the size of the structuring element. In [19] we showed that the morphological operation for color images, as defined so far in the literature, cannot be properly used to define a granulometry function. Moreover, for the pseudo-morphologies we proposed the opening does not obey the idempotence property, therefore we proposed in [19] the usage of pseudo-granulometry (eq. 4.36) for texture discrimination. Its definition used erosion instead of opening.

In Figure 4.19 we show the pseudo-granulometry for 15 sizes of the structuring element, from 3×3 to 31×31 for the color texture images in Figure 3.10. The results are obtained using two pseudo-morphologies: PPM and PM1PCA. One may note that these features do not allow an interpretation directly connected to the pattern spectrum of the image. However, they can be used for texture discrimination.

The volume of a color image was modelled as a hyper-surface in a 5-dimensional space determined by two spatial and three chromatic coordinates (for instance RGB). Thus, extending eq. 4.19 to such a model, the

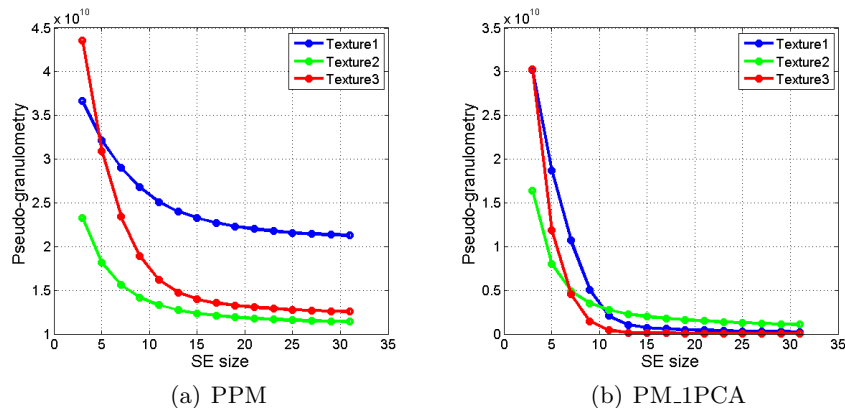


Fig. 4.19: Pseudo-granulometries for images in Figure 3.10.

volume becomes:

$$V(f) = \sum_{(i,j) \in \mathcal{D}_f} f_R(i,j) \times f_G(i,j) \times f_B(i,j) \quad (4.35)$$

where f_R , f_G and f_B represent the color coordinates of the pixel at spatial position (i, j) . Based on this definition of the volume, in [19] a new expression of the pseudo-granulometry was proposed, based on the evaluation of the difference between the volume of the initial image f and the eroded with the structuring element g :

$$[\Gamma_g''(f)](n) = \Delta V_{\varepsilon_{ng}(f)} \quad (4.36)$$

The difference $\Delta V_{\varepsilon(f)}$ between the two volumes is defined as:

$$\Delta V_{\varepsilon(f)} = V(f) - V(\varepsilon(f)) = \sum_{(i,j) \in \mathcal{D}_f} d(f(i,j), \varepsilon(f)(i,j)) \quad (4.37)$$

where $d(f(i,j), \varepsilon(f)(i,j))$ is the distance between the pixel values from the original image and the eroded one. This distance has to be appropriately chosen for grayscale, color or multispectral images.

By using this definition of the pseudo-granulometries for the images in Figure 3.10, the results presented in Figure 4.20 are obtained.

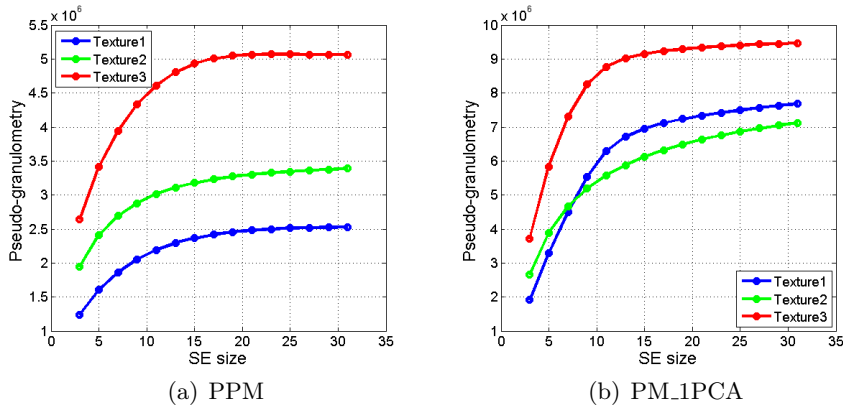


Fig. 4.20: Pseudo-granulometries based on erosion for images in Figure 3.10 using 15 sizes of the structuring element.

Another version of granulometry was introduced by [113] based on erosions instead of openings. Using the maximum distance-based pseudo-morphology, we obtain the results in Figures 4.15 and 4.16 which indicate that erosion would be unhelpful in situations when the background tends to distort objects for large SE sizes. Consequently, another definition we

proposed in [29] uses dilation as the underlying operator for the pseudo-granulometry: $[\Gamma_g(f)](n) = V_{\delta_{ng}(f)}$.

Figure 4.21 depicts the pseudo-granulometries for three versions of the Pompons and Cloth images: grayscale, color and multispectral. There are 10 measurement points corresponding to SE sizes from 3×3 to 21×21 S. All the three curves have a similar evolution, they only diverge slightly for large SE sizes.

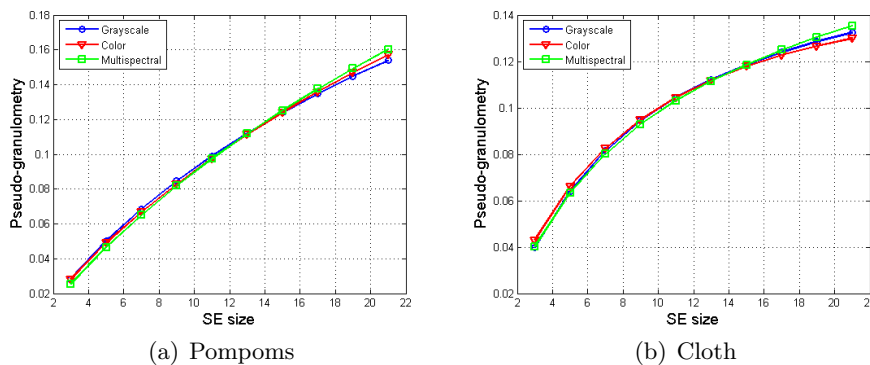


Fig. 4.21: Pseudo-granulometries based on maximum distance.

4.5 Morphological covariance

Morphological covariance is another texture characterisation technique based on morphological operations, which is defined as the variation of the volume of an image as a function of successive erosions using a structuring element composed of two points with a given spatial distance between them (see section 4.1.3). In [17] we proposed the extension of this texture feature to color images using PPM. Due to the fact that the underlying pseudo-morphologies usually require a set of data to compute the two pseudo extrema, in [7] the usage of a composite structuring element was proposed instead of just two points. The results are presented in Figure 4.22 using two SEs of size 3×3 and the distance between them varied in 25 steps on four directions ($0^\circ, 45^\circ, 90^\circ, 135^\circ$).

The same issue of image volume computation stands both for color and multivariate images. We showed already how a first approach is to compute marginal volumes on each channel, with the volume of the image resulting as the sum of the marginal volumes. Another approach would be to compute the difference between the volume of the original image f and the volume of the morphologically processed image f_{mp} [17]:

$$\Delta V_{f,f_{mp}} = \sum_{i \in \mathcal{D}_f} d(f(i), f_{mp}(i)) \quad (4.38)$$

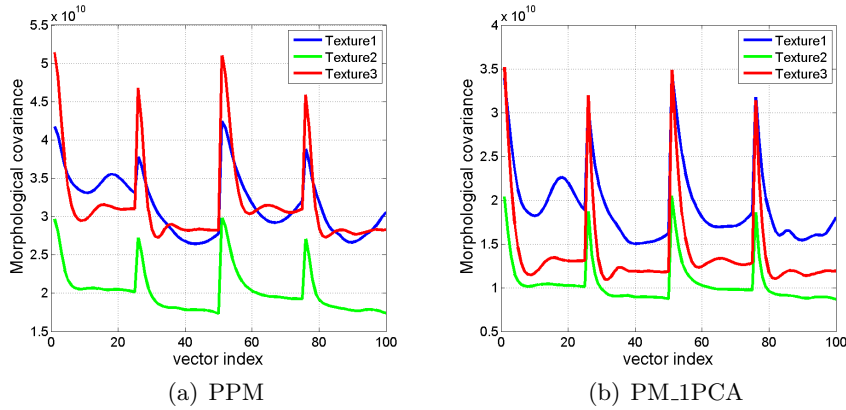


Fig. 4.22: Morphological covariance based on pseudo-morphologies for the texture images in Figure 3.10.

where $d(\cdot, \cdot)$ is the absolute value of the difference in the case of grayscale images, the CIELAB ΔE distance in the case of color images and the Euclidean distance for multispectral images. The results are presented in Figure 4.23 using two SEs of size 3×3 and the distance between them varied in 25 steps on four directions ($0^\circ, 45^\circ, 90^\circ, 135^\circ$)

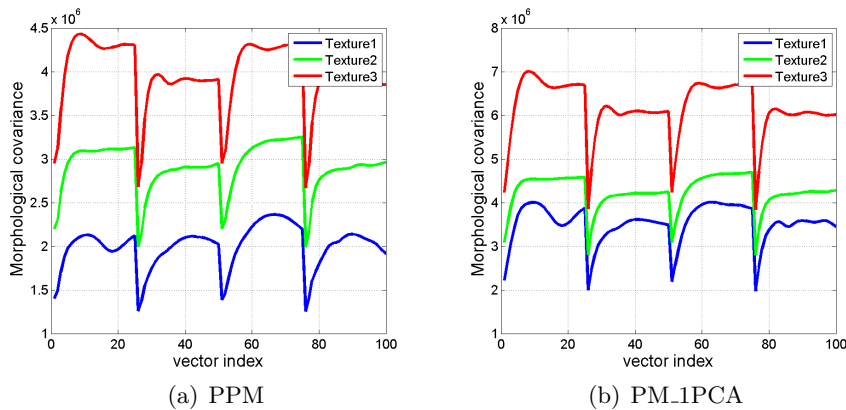


Fig. 4.23: Morphological covariance based on pseudo-morphologies for the texture images in Figure 3.10 using the volume difference in eq. 4.38.

If we consider the maximum distance-based pseudo-morphology, the original definition of the morphological covariance using just a pair of points would not be useful either: for the color images case, pseudo-erosion would simply be the lexicographic minimum in the CIELAB space between the two points covered by the SE. Consequently, we chose again for the computation of the morphological covariance a composite SE like in [6], composed of two

subsets of points separated by a vector \vec{v} . We also use pseudo-dilation instead of pseudo-erosion, for the reasons mentioned above and the definition becomes:

$$[K(f)][\vec{v}] = V_{\delta_{P_2, \vec{v}}}(f) \quad (4.39)$$

The results are presented in Figure 4.24, illustrating the morphological covariance computed using 10 iterations for each orientation, exhibiting a great similarity for the three types of images. The volume computation is based on eq. 4.38.

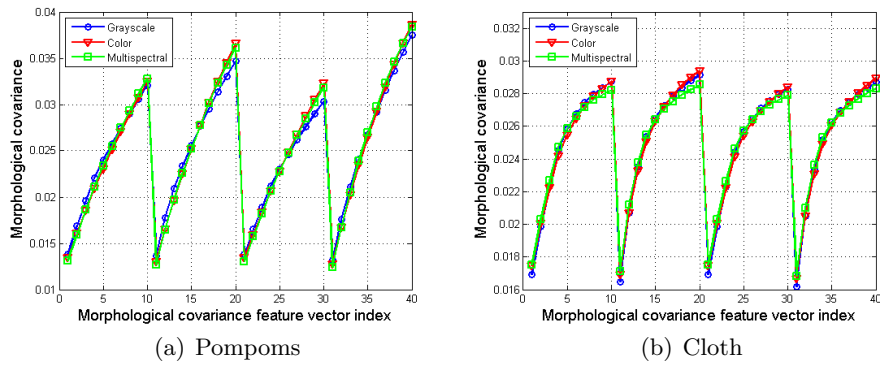


Fig. 4.24: Morphological covariance curves.

Chapter 5

Applications

In this chapter we focus on image segmentation both for color and multi-spectral images. We discuss also about texture classification in this context of image segmentation. Since the world of image became colored, the segmentation approaches became more sophisticated. In many publications, approaches for gray-level image segmentation are presented by authors who afterwards claim that most of the techniques can be extended to color or multi-spectral images as well. However, the extension of scalar operations to vectors is not straight-forward, therefore the same approaches for gray-scale images should not be applied *as they are* to the color domain, but they should rather be adapted accordingly.

The purpose of the current chapter is to present the several image segmentation frameworks that are built on features and tools presented in the previous chapters. The reader is advised to read the chapters on segmentation from a couple of classical books in image processing, i.e. [66] and [46] for a complete understanding of the basics on image segmentation. The theoretical concepts that form the ground for all segmentation approaches, e.g. similarity, discontinuity and pixel connectivity [44], [46] [131], constitute the prerequisites for the easy-reading of this chapter.

5.1 Image segmentation

Image segmentation is the process of dividing an image into *regions* according to predefined *criteria*. The resulting regions are called *segments*. Segmentation is often followed by further image analysis, like object detection or recognition. Errors in the segmentation process may lead to inaccuracies in any subsequent analysis [127]. It is thus worthwhile to produce an image segmentation, that is as *accurate* as possible with respect to application requirements. The initial hypothesis is that each resulting region or segment represents an object in the original image, in other words each segment is semantically meaningful, which greatly facilitates the image content analy-

sis and interpretation. A learning phase or classification can follow in order to associate the segments to terms describing the content of the image, like annotations, or, in other words to map the *pixelic* content to the *semantic* image description. Historically, image segmentation was the center point of computer vision – the processing and the analysis procedures aimed at helping the robots to detect simple geometrical objects based on line and circle detection.

For gray-scale images the segmentation techniques were always divided in two major classes: contour- and region-oriented, followed recently by more elaborated techniques based on features. Sometimes, depending on application, segmentation may not be required as certain points of interest, like corners are detected [84] [57]. According to Fu [44], the segmentation techniques can be categorized into three classes: (i) characteristic feature thresholding or clustering, (ii) edge detection and (iii) region extraction. In [90] there are six categories identified, which are finally reduced to the same three already mentioned. We shall focus on region-segmentation, without considering edge detection in the context of color and multispectral images as it was partially addressed in Chapter 4. Moreover, the widely-used technique of edge detection [20] is nowadays performed on the feature images, in order to detect ruptures in the color texture, for instance.

Segmentation evolved in the last two decades, from the initial exploratory approaches mostly in the pixel value space to feature-space-based techniques, and in addition it became multi-resolution and multi-stage. The image is analyzed at various resolutions, from a rough or coarse view, to a fine and detailed one (see Fig. 5.1). In addition, the image segmentation process is performed in several stages, starting with a pre-processing phase whose purpose is to reduce noise (e.g. smoothing), thus reducing the complexity of the color information in the image, followed by a computation of a local descriptor, a *feature* – a characterization of the color/spectral information and texture.

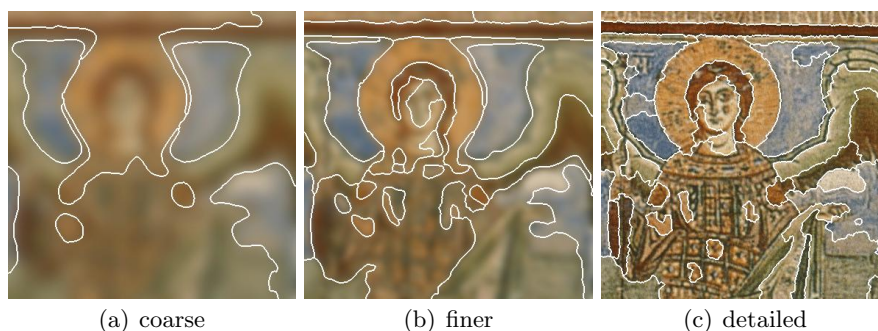


Fig. 5.1: Images at various resolutions and a possible segmentation using JSEG [35]. *Angel* image is courtesy of Centre d'Etudes Supérieures de Civilisation Médiévale (CESCM), UMR 6223, Poitiers, France.

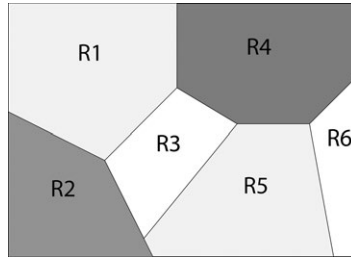


Fig. 5.2: Theoretical example of segmentation.

A digital image I is modelled from a mathematical point of view as a function $I(x, y)$ which maps the locations (x, y) in space to the pixel value $I(x, y) = v$. Traditionally, images were black and white or gray and values were discrete from 0 to 255; in this case v will be a scalar. Since the world of images became colored, color images are used everywhere and RGB images are very common. In both cases, v will be a vector (r, g, b) . For multispectral images v will be an n -dimensional vector (b_1, b_2, \dots, b_n) .

A discrete *image* I is a function $I : \mathbb{N}^2 \rightarrow \mathbb{V}$. *Locations* P belong to the image support, i.e. a finite rectangular grid, i.e. $D = [0, \dots, M] \times [0, \dots, N] \subseteq \mathbb{N}^2$. For *gray-scale* images $\mathbb{V} = [0, \dots, 255] \subseteq \mathbb{N}$; for *color images* we (usually) have $\mathbb{V} = [0, \dots, 255]^3 \subseteq \mathbb{N}^3$. An image element X is called a *pixel* which has a *pixel location* $\Lambda(X) = P$ and a *pixel value* $\Upsilon(X) = I(\Lambda(X)) = v \in \mathbb{V}$.

If we enumerate the pixels in an image as $\{X_1, \dots, X_{N_P}\}$, we use $N_P = M \cdot N$ as the number of pixels in an image.

From a mathematical point of view, for an image I , the segmentation operation formalism states that the image is decomposed into a number N_R of regions R_i , with $i = 1..N_R$, which are disjoint non-empty sections of I , like in Fig. 5.2. Regions are connected sets of pixel locations that exhibit some similarity in the pixel values which can be defined in various ways.

The result of segmentation is a set of regions $\{R_i\}, i \in \{1, \dots, N_R\}$ which can be represented in several ways. The simple solution used frequently is to create a so-called *region label image* (I_R) which is a feature image where each location contains the index of the region that this location is assigned to, i.e. $I_R : \mathbb{N}^2 \rightarrow \{1, \dots, N_R\}$. This label image is also called a *segmentation map*.

Haralick and Shapiro state in [54] the guidelines for achieving a *good* segmentation: (i) regions of an image segmentation should be uniform and homogeneous with respect to some characteristic such as gray tone or texture; (ii) region interiors should be simple and without many small holes; (iii) adjacent regions of a segmentation should have significantly different values with respect to the characteristic on which they are uniform and (iv)

boundaries of each segment should be simple, not ragged, and must be spatially accurate. Partially, these guidelines are met by the formal properties below.

The segmentation of an image I into regions R_i is called *complete*, if the regions exhibit the properties listed in [44] which we formalize in the following:

- $\bigcup_{i=1}^{N_R} R_i = D$, i.e. the union of all regions should give the entire image, or in other words, all the pixels should belong to a region at the end of segmentation;
- $R_i \cap R_j = \emptyset \quad \forall i \neq j$, i.e. the regions should not overlap;
- each segment R_i is a connected component or compact, i.e. the pixel locations $P \in R_i$ in a region R_i are connected; we will define different notions of connectivity in the following paragraphs;
- $\forall i$, a certain criterion of uniformity $\gamma(R_i)$ is satisfied, ($\gamma(R_i) = TRUE$), i.e. pixels belonging to the same region have similar properties;
- $\forall i \neq j$, the uniformity criterion for $R_i \cup R_j$ is not satisfied ($\gamma(R_i \cup R_j) = FALSE$), i.e. pixels belonging to different regions should exhibit different properties.

If a segmentation is complete, the result of segmentation is a partitioning of the input image, corresponding to the choice of homogeneity criterion γ for the segmentation. There are usually two distinguished cases: *oversegmentation* and *undersegmentation*. The oversegmentation means that the number of regions is larger than the number of objects in the images, or it is simply larger than desired. This case is usually preferred because it can be fixed by a post-processing stage called *region merging*.

The authors of [127] emphasize the concept of *pixel connectivity* as fundamental within the context of image segmentation. The pixels are adjacent [106] and there are mainly two types of connectivity: *4-connectivity* and *8-connectivity*, the latter one being mostly used. Variants like the *6-connectivity* which is used in segmentation approach proposed by [99] do exist. The three types of pixel connectivity are illustrated in Fig. 5.3.

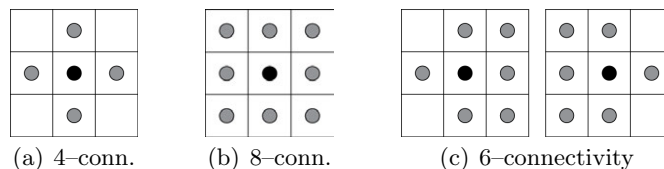


Fig. 5.3: Pixel connectivity.

Rectangular or squared tessellation of digital images induce the problem of how to define a neighborhood of a pixel for a discrete set, as an approximation for the case of continuous metric space, when the neighborhood usually represents an open ball with a certain centre and radius [38]. The choice of the neighborhood is of extreme importance for region-growing-based segmentation methods. Each version has advantages and disadvantages, when sets of similar pixels are searched in segmentation that should result in a connected region.

Since Haralick [54], the notion of homogeneity is inseparable from the segmentation purpose. Apparently, content homogeneity seems to describe a simple concept: that visual content is visually and physically into an inseparable whole. And right behind this definition, authors simplify the purpose as a problem concerning only the distribution of a variable. If we assume that we could define one information feature which explain this phenomena, we need to define the measure that could indicate if the content is homogeneous or heterogeneous upon this feature. In a context of landscape complexity analysis, Feagin lists several possible criteria [41], upon the fact that the variables are distributed in a qualitatively patchy form [118] or quantitatively defined [76] by an index such as lacunarity [98]. Very often authors define a binary criterion for the homogeneity of a region R_i , based on a threshold empirically determined.

This describes regions where no pixel differs from the mean of the pixel values inside the region by more than a threshold. This measure requires that the range \mathbb{V} is an algebra that supports addition and a norm. Such definitions do not necessarily lead to a unique segmentation, different processing strategies and algorithms will thus yield different regions. Classically in image processing, variables are chosen from gray-level or color distribution, more rarely from color texture.

Such approach is too simple for the actual challenge of segmentation, with the increase of spatial and spectral resolution of images. In order to improve segmentation, Feagin defines the homogeneity criteria from the shape of the distribution by several parameters like the relative richness, entropy, difference, scale-dependent variance [41]. It is interesting to note that texture definition used by Feagin is defined as a multiscale one, for which the homogeneity is linked to the stationarity of the distribution along the scale. But the more interesting conclusion of this work dedicated to the notion of homogeneity and heterogeneity is around the fact that the homogeneity perception depends on the perceived scale and could be homogeneous for large scales and heterogeneous for fine scales for the same feature. In [77] the authors explored the heterogeneity definition as the complexity of a property in space with two further questions: the structural heterogeneity that is the complexity measured without reference and the heterogeneity as a function of scale [71]. As it is for the definition of homogeneity or heterogeneity, the purpose is clearly expressed as a multi-scale complexity and as a result,

the question of the uniqueness of the analysis parameter along the scale is asked. And by extension, as features are specialized in color distribution, texture parameters or wavelets analysis, the true question becomes for the next years: how to merge dynamically several features as a function of the analysis scale.

5.2 Watershed segmentation

The watershed segmentation technique is a region-based segmentation approach, in which the image is regarded as a landscape [13] [103]. Historically and by definition, watershed is the approach of the mathematical morphology. Since its first appearance several improvements followed [32]. The segmentation process is similar modelled as to the rain falling on that landscape which will gradually flood the *basins* [14]. The watersheds or dams are determined as the lines between two different flooded basins that will merge. When the topographical relief is flooded step by step, three situations can be observed: (i) a new object is registered if the water reaches a new local minimum. The corresponding pixel location is tagged with a new region label; (ii) if a basin extends without merging to another, the new borders have to be assigned to this basin; and (iii) if two basins are about to unite, a dam has to be built in between.

Unsupervised approaches of watershed use local minima of the gradient or heterogeneity image as markers and flood the relief from these sources. To separate the different basins, dams are built when flooded zones are meeting. In the end, when the entire relief becomes completely flooded, the resulting set of dams constitutes the *watershed* (see Fig. 5.4 for an illustration of the approach): a) the considered basins begin to flood, then basin V_3 floods a local minimum and basin V_1 floods another local minimum; b) a dam is built between valleys V_1 and V_2 and another one between V_2 and V_3 and then followed by the final step of the algorithm.

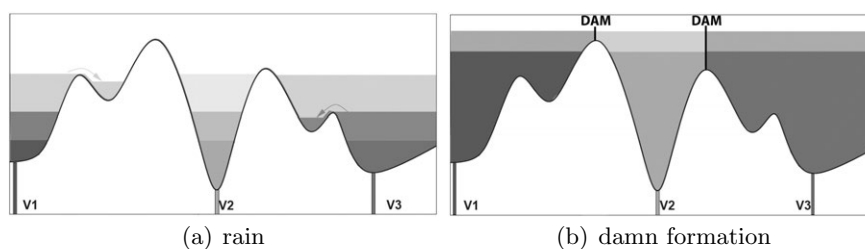


Fig. 5.4: Illustration of basin flooding in the watershed approach.

The watershed approach is traditionally applied in the original image domain, but it has a major disadvantage since it fails to capture the global information about the color content of the image. Therefore in Chapter X

of [131] an approach that uses the watershed to find clusters in the feature space is proposed. An alternative, the gradient or heterogeneity information does not produce closed contours and hence do not necessarily provide a partition of the image into regions. As this information could be used as scalar information – classically the norm of the gradient vector – they are well adapted to watershed processing. Having this point of view, the gradient images can be seen as a topographical relief: the gray level of a pixel becomes the elevation of a point, the basins and valleys of the relief correspond to the dark areas, whereas the mountains and crest lines correspond to the light areas. The watershed line may be intuitively introduced as the set of points where a drop of water, falling there, may flow down towards several catchment basins of the relief [31]. In Figure 5.5 the evolution of the watershed along the scale is illustrated. Usually a merging phase follows.

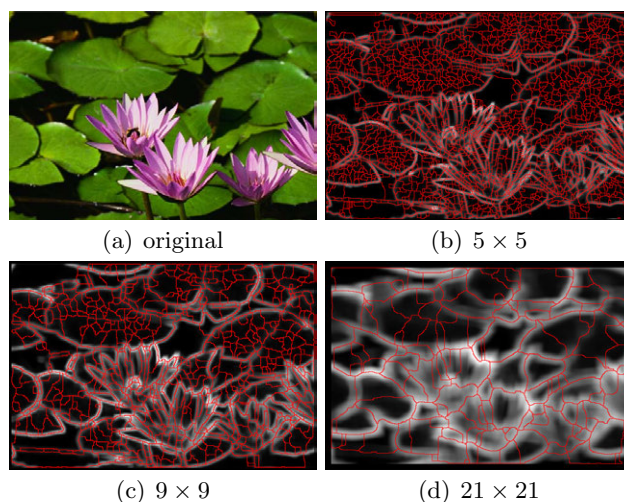


Fig. 5.5: The evolution of the watershed segmentation along the scale.

Several watershed approaches for color images exist [107] [23] [27]. Chanussot et al. extended the watershed approach to the color domain by using the bit mixing technique for multivalued morphology [22]. In [27] the authors use a perceptual color contrast defined in the HSV color space, after a Gaussian low pass filter and a uniform color quantization to reduce the number of colors in the image.

5.3 Active contours

Active contours, colloquially called *snakes*, were introduced by Kass, Witkin, and Terzopoulos in 1988 [69] and defined as energy-minimizing splines guided by external constraint forces and influenced by image forces that pull it toward features such as lines or edges. The active contours are successfully

used for image segmentation in various applications.

The initial contour is incrementally deformed according to several specified energies. According to the original definition, an active contour is a spline $c(s) = [x(s), y(s)]$, with $s \in [0, 1]$, that minimizes the following energy functional [116]:

$$\varepsilon(c) = \varepsilon_{\text{int}}(c) + \varepsilon_{\text{ext}}(c) = \int_0^1 [E_{\text{int}}(c(s)) + E_{\text{ext}}(c(s))] ds \quad (5.1)$$

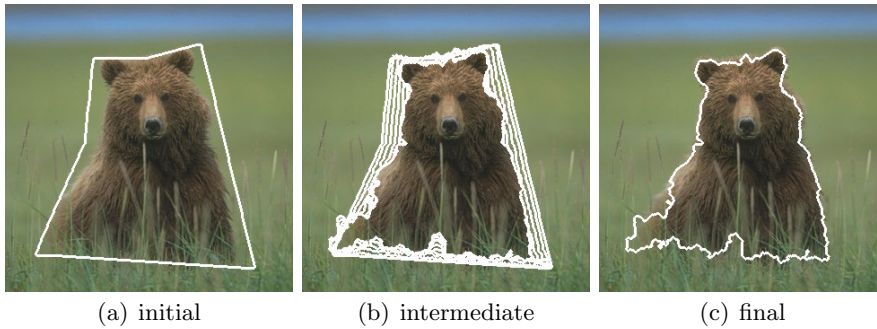
where $\varepsilon_{\text{int}}(c)$ represents the *internal* energy and $\varepsilon_{\text{ext}}(c)$ represents the *external* energy. The internal energy is intrinsic to the spline and the external energies come either from the image or specified by the user, usually as external constraints. The internal energy ε_{int} is usually written as:

$$\varepsilon_{\text{int}}(c) = \int_0^1 \frac{1}{2} [\alpha(s) |c'(s)|^2 + \beta(s) |c''(s)|^2] ds \quad (5.2)$$

where $c'(s)$ and $c''(s)$ are the first and the second derivatives, weighted by $\alpha(s)$ and $\beta(s)$, which are usually considered to be constants in most of the implementations.

Xu [130] identifies several issues of the original model [69]: (i) the initialization of the snake has to be close to the edge and (ii) the convergence to concave boundaries is poor. These were partially addressed in the original article [69] by using the propagation in the scale space described in [126] [125]. The *balloon model* [28] introduced supplementary external forces for stopping the snakes in the case when the contour was not *visible* enough. The drawbacks of this approach were corrected by the approach of Tina Kapur [68]. Later on, the Gradient Vector Flow (GVF) was introduced by Xu, as well as the Generalized Gradient Vector Flow (GGVF) [128][130][129], the two methods being widely used, despite the fact that they are complex and time consuming. Active contours have been extended to the so-called *level-set* segmentation which has also been extended to color images in [67]. We used the first-order moment of the correlation integral to define a diffusion model for color images [64].

We present the results of a multi-resolution approach extended to the color domain on a color textured image from the Berkely image data-base exhibiting one central salient object (see Figure 5.6). The hypothesis that is made is that in such images there are two types of textures, exhibiting different complexities: one corresponding to the salient object and the other to the background (the complexity of the latter one being usually smaller).

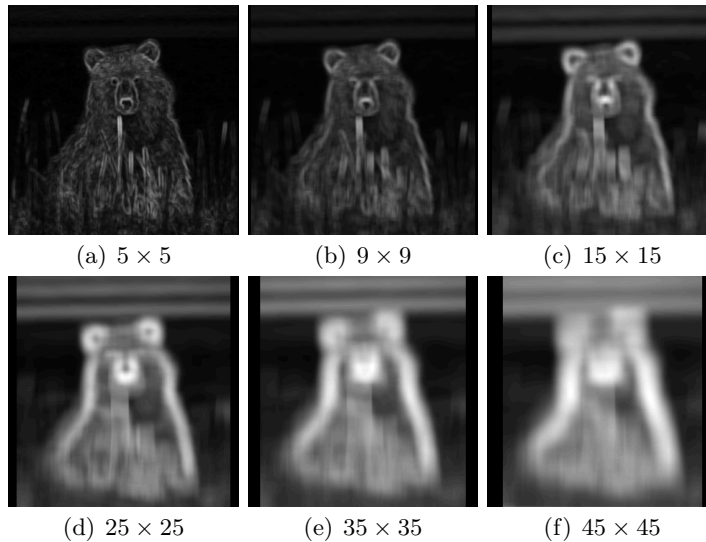


(a) initial (b) intermediate (c) final

Fig. 5.6: Example Berkely image 100080 (color).

The external energy is linked to the correlation dimension (practically being the mean value of the $C(\delta)$ distribution) and also related to the J factor (JSEG) given that it represents a measure of the heterogeneity in a certain neighborhood, at a given resolution. The external energy forces that drive the active contours are given by the average CIE Lab ΔE distance computed locally at different resolutions, based on the original image (see Figure 5.7). For a certain resolution, the value of one point (x, y) in the energetic surfaces is given by the average CIE Lab ΔE distance computed in a neighborhood of size $n \times n$ centered in that specific point. One has to compute the average value of $\frac{n^2(n^2-1)}{2}$ distances:

$$E_{\text{ext}}(x, y)|_{n \times n} = \frac{2}{n^2(n^2-1)} \sum_{i=1}^{n^2} \sum_{j=i+1}^{n^2} \Delta E(v_i, v_j) \quad (5.3)$$



(a) 5×5 (b) 9×9 (c) 15×15
(d) 25×25 (e) 35×35 (f) 45×45

Fig. 5.7: Diffusion pseudo-images for Berkely image 100080 (crop).

5.4 Feature-based textured image segmentation

Very often segmentation is performed in a feature space, not directly on the pixel data. Such a feature space can be represented by any features from the set of features presented in the previous two chapters of this book. Usually a clustering technique (e.g. k -means) is used to classify the pixels of an image as a function of their local feature. This approach is illustrated in Figure 5.8: the feature extraction is performed locally, followed by a classification of features. The advantage of this approach is that the number of desired regions can be specified through the number of classes.

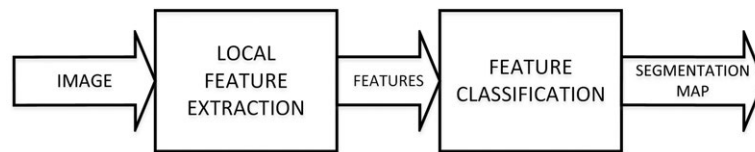


Fig. 5.8: Feature-based textured image segmentation using feature classification.

In Figure 5.9 we show the segmentation results for a color textured image from the Berkely image data-base when using as local features the two morphological features presented in Chapter 4: granulometry and the morphological covariance. The classification was unsupervised (k -means). The value of $k = 2$ was chosen based on the hypothesis that there are only two regions in the image, from the point of view of texture characterization: the object of interest and the background. The two morphological features were computed using 10 iterations. For the granulometry we used square SE from 3×3 to 21×21 and for the morphological covariance the distance between the ES was varied from 0 to 9.

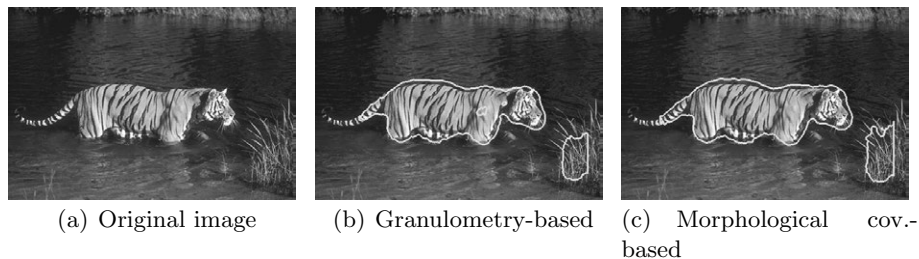


Fig. 5.9: Image segmentation using the approach depicted in Figure 5.8.

To illustrate this color textured image segmentation technique, we used as local texture feature the vector of volumes computed between pseudo-dilation and pseudo-erosion, for varying sizes of the SE. The two pseudo-morphological operations are presented in Chapter 4. We present our results

regarding the quantitative evaluation of the impact of the PPM approach in such a segmentation framework. We compare our approach with two pseudo-morphological approaches: the α -trimmed pseudo-morphology, computed in RGB color space and with the lexicographical morphological approach, using the HSV color space with (V,S,H) component priority. We performed image segmentation based on local texture features. We used this feature due to the fact that it reflects the texture complexity, since in the log-log space, it allows the estimation of the FD of the given texture. However, as for real textures the fractal hypothesis does not stand, we chose to use the entire vector, which comprises more information than the FD by itself. We used textured images from the Berkeley database [82], in which there is a salient object and the background. Our first attempt is to discriminate between *simple* (out of focus regions) and *complex* (in focus object). Thus, we computed the vectors for local regions within the images, using sliding window, followed by a k -means classification in two classes. We computed the segmentations using PPM, α -trimmed and (V,S,H) lexicographical ordering. We also generated a ground-truth segmentation, performed by a human, which is used as a reference for a quantitative comparison among the three approaches. The results are depicted in Fig. 5.10.

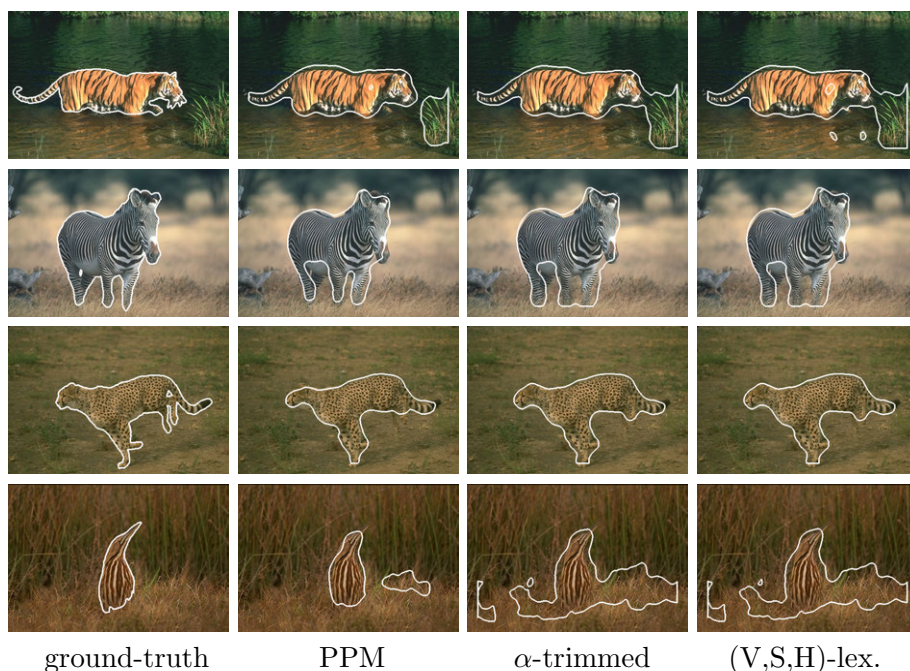


Fig. 5.10: Segmentations based on local texture features obtained using PPM, α -trimmed pseudo-morphology and (V,S,H) lexicographical morphology for Berkeley 108073 (1st row), 130066 (2nd row), 134008 (3rd row), 43033 (4th row) images.

As a quantitative comparison, we computed the percentage of correctly-classified pixels as a segmentation evaluation criterion, as in [21]. The results are presented in Table 5.1. One may notice that in the most of the cases, PPM leads to a better segmentation, proving the increased ability to capture the complexity of textures and variation along scales. Segmentation could be further improved, by considering the window size used for local feature computation.

	PPM	α -trimmed	(V,S,H) lex.
Berkeley108073	92.37%	91.41%	90.57%
Berkeley130066	96.06%	95.37%	95.40%
Berkeley134008	96.53%	96.86%	96.90%
Berkeley43033	96.35%	86.01%	86.19%

Table 5.1: Percentage of correctly classified pixels for images in Fig. 5.10.

5.5 Color texture classification

In order to demonstrate the usefulness of our pseudo-morphological approach for texture description and classification we chose the normalized morphological covariance [114], recently extended to color images [8]. By definition, the morphological covariance is the volume of an eroded image, using a pair of points $P_{2,\vec{v}}$ separated by a vector \vec{v} , as SE: $[K(f)][\vec{v}] = V_{\varepsilon_{P_{2,\vec{v}}}}$. However, since in PPM we need a distribution of a set in order to estimate the two pseudo-extrema, we embrace the approach proposed by [8], in which a pair of SEs separated by a vector \vec{v} is used instead of just two points. In addition, K is normalized according to the volume of the initial image. For the volume computation we propose to use the volume between the initial image and the pseudo-eroded image, in order to better capture the differences between the initial and the resulted colors, after pseudo-erosion. We compute the normalized covariance using the following four orientations for \vec{v} ($0^\circ, 45^\circ, 90^\circ, 135^\circ$) and 25 iterations on each orientation, varying the module of \vec{v} with a step of two pixels, thus resulting a K vector of size 100. We performed the following two experiments.

We performed the classification on the Outex13 color texture database, which consists of 68 textures, each divided into 20 non-overlapping sub-images of 128×128 pixels, thus resulting 1360 images to be classified [89]. We computed the normalized covariance for each of the 1360 sub-images, using three pseudo-morphology approaches: PPM, α -trimmed and (V,S,H) lexicographical morphology. We use half of the resulted vectors as training samples and half of them as test samples, within the out-of-the-box discriminant analysis available in MATLAB, obtaining approximately the same

good classification rates for all the three used approaches (76.76% for PPM, 76.32% for α -trimmed and 76.47% for (V,S,H) lexicographical morphology). This experiment showed that our PPM approach generates a comparable result with the ones given by the other two approaches.

In order to focus on the extracted morphological features rather than on the classification process itself, we embraced the protocol proposed by [9]. In addition, taking into consideration that in the Outex13 database there are many visually similar images which are considered as different textures (e.g. the sandpaper or the barley-rice textures) we performed another experiment in which we chose nine classes of color textures from the Outex database (barleyrice, canvas, carpet, chips, fur, granite, plastic, seeds and wood), with 8 images from each class. These images were split into 20 sub-images of size 128×128 , thus resulting 1440 samples. We computed the morphological covariance for each of these samples and we used half of the resulted vectors as training set and half of them as test set. Using this set of textured images and the generalized co-occurrence matrix along with the classification protocol described in [9] we obtained a good classification rate of 88.27%, which we further use as reference. The good classification rate obtained using PPM is 81.38%, while the result obtained using α -trimmed pseudo-morphology is 68.5%. However, given that our morphological covariance is based only on color differences, being invariant to the actual colors within the textures, we added the first and the second probabilistic moments of each color channel within the feature vector. The obtained results for good classification rates are 92.36% for PPM and 78.47% for α -trimmed. In conclusion, the morphological covariance obtained using our PPM leads to a worse result than the one obtained using the generalized co-occurrence matrix, but by adding the color information, we are able to obtain a higher good classification rate. In this particular context, our approach shows a better contribution to textural feature extraction than the α -trimmed pseudo-morphology.

5.6 Discussion

The segmentation process requires addressing three issues: (i) the features capturing the homogeneity of regions, (ii) the similarity measures or distance functions between features content and (iii) the segmentation framework which optimizes the segmentation map as a function of the feature-metric pair. We presented the color segmentation frameworks separately, but very often there is only a fine frontier between them and quite often hybrid techniques emerge, that combine for instance pyramids and watersheds [2] and the approach proposed by Serra [111]. However, the segmentation approaches evolved towards unanimously-accepted frameworks. Several segmentation frameworks imposed themselves as *standard* techniques: pyramidal approaches, watershed, JSEG, graph cuts, normalized cuts, active con-

tours, or more recently, TurboPixels. Recently, a new trend is oversegmentation followed by region merging *TurboPixel* segmentation or *SuperPixels* [74].

Nowadays the question still remains since Haralick: which is the best value for the parameters of the homogeneity criteria? There are no recommended recipes. New perspectives come from psychophysics with perceptual theory, in particular Gestalt theory. As the homogeneity/heterogeneity definition have been expressed as complexity of a feature distribution, these perceptual theories search to explain what are the physical parameters that are taken into account by the human visual system. An open question is given by the relationship between the similarity law from Gestalt theory and the homogeneity. Randall in [100] links the similarity law to grouping into homogeneous regions of color or texture. Several works in physiology and in human vision have explored this process with stochastic or regular patterns, but nowadays this work is in progress for color patterns as well. Nevertheless, the definition of homogeneity is still imperfect, often reduced to basic moments available for particular scales of the image. The future trends should be around these questions.

Subpart II.2

The evolution and development plans for career development (in Romanian)

Planul de dezvoltare a carierii universitare

Motto-ul planului de dezvoltare a carierei universitare aparține filosofului chinez Confucius, care spunea că: dacă strategia ta este pe un an, atunci plantează orez; dacă strategia ta este pe zece ani, atunci plantează un copac; dacă strategia ta este pe o sută de ani, atunci educă copii.

Planul de dezvoltare a carierei universitare este inspirat de paradigmele oferite de profesorii pe care am avut onoarea și plăcerea să-i cunosc de-a lungul studiilor și carierei mele, cărora le datorez, în mare parte, ceea ce sunt și gândesc. În mod special aș dori să subliniez contribuția esențială la formarea mea personală și profesională a mentorului meu, regretatul prof. dr. ing. Vasile Buzuloiu, de la Universitatea Politehnica din București.

Cariera profesională are câteva coordonate importante în 2015, esențiale pentru evoluția ulterioară:

- **iunie** 2015: Universitatea Transilvania din Brașov a devenit oficial instituție colaboratoare la experimentul ATLAS de la LHC¹, CERN², Geneva, Elveția, alături de Institutul de Fizică și Inginerie Nucleară Horia Hulubei din Măgurele, Universitatea Politehnica din București și Institutul Național de Cercetare-Dezvoltare pentru Tehnologii Izo-topice și Moleculare din Cluj-Napoca, ca urmare a recunoașterii de către CERN și echipa de management a experimentului ATLAS a contribuțiilor echipei pe care o coordonez, în special la dezvoltarea sistemului electronic de achiziție de date de la detectorii de muoni din cadrul New Small Wheel;
- **iulie** 2015: Aprobarea și demararea Comitetului Tehnic TC 8-14 în cadrul Diviziei 8 *Image Technology* a CIE³ intitulat *Specification of Spatio-Chromatic Complexity*, propus împreună cu Noël Richard de la laboratorul de cercetare XLIM-SIC, Université de Poitiers, Franța. Obiectivul acestui comitet tehnic este acela de a produce un raport cu

¹Large Hadron Collider.

²Organizația Europeană pentru Cercetări Nucleare.

³Comisia Internațională de Iluminare.

privire la definițiile existente ale noțiunii de complexitate, în special în ceea ce privește texturile color neuniforme și de a combina aceste definiții în vederea obținerii unei definiții unitare care să includă, într-o formă generică și vectorială, atât variațiile spațiale cât și cromatice ale texturii. De asemenea, se dorește elaborarea unor etaloane, atât sub formă de imagini digitale color, cât și sub formă fizică, ce vor permite măsurarea complexității texturilor color neuniforme. Comitetul tehnic este format din Noël Richard, Dominique Lafon, Christine Fernandez-Maloigne (Franța), Mihai Ivanovici (România), Davide Gadia, Alessandro Rizzi (Italia), Kinjiro Amano (Marea Britanie), Jon Hardeberg (Norvegia), Masayuki Tanaka (Japonia), Manuel Mengoza (Spania) și Ghorbel Faouzi (Tunisia);

- **octombrie 2015:** Confirmarea ca director al centrului de cercetare C13 intitulat *Sisteme Electronice Încorporate și Comunicații Avansate* din cadrul Institutului CDI al Universității Transilvania din Brașov, după ce în perioada 2012 - 2015 am ocupat poziția de adjunct al directorului centrului, prof. dr. ing. Gheorghe Toacșe.

Obiective

Obiectivul general pe care mi l-am propus în vederea continuării dezvoltării carierei mele universitare îl constituie dobândirea de noi competențe (cunoștințe, aptitudini, atitudini etc.) atât în ceea ce privește activitatea de cercetare cât și cea didactică, printr-o instruire și o auto-instruire perpetuă, precum și printr-o susținută viață academică. Obiectivul general se derivă în obiective ce țin de activitatea de cercetare și obiective ce țin de activitatea didactică, după cum urmează:

Obiective cu privire la activitatea de cercetare

De menționat că în 2012 când am obținut titlul de conferențiar universitar, unul dintre obiectivele planului meu de dezvoltare a carierei universitare era *dobândirea în cel mult 5 ani a abilitării de conducere de doctorat*. Obținerea abilitării nu este un țel în sine, este doar o unealtă, o bornă kilometrică pe calea atingerii țelului pe care mi l-am propus—acela de a crea la Brașov un *laborator de cercetare* în adevăratul sens al cuvântului, nu doar o structură administrativă într-un cadru instituțional. Cum am mai spus-o, de dragul domnului prof. dr. ing. Gheorghe Toacșe, o încercare de a renaște ITC⁴-ul de altă dată...

- Continuarea traiectului științific început în 2007 - analiză/caracterizare de texturi color, multispectrale și hiperspectrale, și segmentare de

⁴Institutul de Tehnică de Calcul. Este vorba aici de filiala acestuia de la Brașov.

imagini color (multivariate), bazate pe geometrie și analiză fractală, precum și morfologie matematică (inclusiv pseudo-morfologie probabilistică;

- Dezvoltarea unor direcții noi de cercetare în domeniul prelucrării și analizei imaginilor color, multispectrale și hiperspectrale (achiziție imagini multispectrale, prelucrări vectoriale, aproximare PCA⁵), dar și în electronică și microelectronică pentru fizica particulelor - proiectare și implementare de FPGA⁶, ASIC⁷ și PCB⁸ (Read-Out Controller pentru electronica de front-end la detectorii de muoni MicroMEGA din cadrul New Small Wheel, experimentul ATLAS de la Large Hardon Collider, CERN, Geneva);
 - Contribuirea în următorii 4 ani la implementarea obiectivelor științifice și de standardizare ale Comitetului Tehnic CIE TC 8-14 Specification of Spatio-Chromatic Complexity propus împreună cu Noël Richard de la laboratorul de cercetare XLIM-SIC, Université de Poitiers, Franța, împreună cu ceilalți parteneri europeni, americani și japonezi.
- Continuarea dezvoltării centrului de cercetare C13 din cadrul Institutului CDI al universității, precum și a laboratorului *Machine Intelligence and Vision* (MIV) de cercetare din cadrul centrului C13, prin atragerea de fonduri din granturi, proiecte și contracte de cercetare;
 - partener nr. 5 (2014-2015) în cadrul proiectului *Experimentul ATLAS de la LHC*, coordonat de IFIN-HH Măgurele, contract nr. 7 / 2012, PNII, programul RO-CERN, modul CAPACITĂȚI; proiect în derulare cu perspective de continuare pe termen lung;
 - două contracte de cercetare (2014 și 2015, unul din ele în derulare) cu firma S.C. PREH România S.R.L. din Ghimbav, pentru dezvoltarea de sisteme electronice încorporate pentru industria automotive;
 - propunere HORIZON 2020 de tip FET-OPEN intitulată COMET (*COmplexity METrology for the future electronic eyes*) depusă în 29 septembrie 2015 (Universitatea din Poitiers (FR), Universitatea Transilvania din Brașov (RO), Universitatea din Milano (IT)); propunere în curs de evaluare;
 - propunere de înființare a unui centru de competențe în tehnologii spațiale în cadrul programului STAR⁹ al Agenției Spațiale Române

⁵Principal Component Analysis.

⁶Field Programmable Gate Array.

⁷Application-Specific Integrated Circuit.

⁸Printed Circuit Board.

⁹Space Technology and Advanced Research.

- (ROSA¹⁰); propunere în lucru;
- propunere TE 2014 depusă, intitulată ICAR (Imagistică pentru agricultură - analiza texturilor multispectrale pentru monitorizarea stării de vegetație a culturilor de cartof și sfeclă de zahăr) a obținut un punctaj de 85.5, dar nu a fost finanțată;
 - propunere HORIZON 2020 de tip TWINNING - contribuție ca partener, propunere nefinanțată.
- Valorificarea rezultatelor cercetărilor prin publicarea de lucrări științifice în reviste internaționale cu scor relativ de influență (SRI) mare;
 - articol acceptat la Journal on Instrumentation (FI = 1.39) intitulat *The Read Out Controller for the ATLAS New Small Wheel*, autori: R. Coliban, S. Popa, T. Tulbure, D. Nicula, M. Ivanovici, S. Martoiu, L. Levinson și J. Vermeulen;
 - articol în recenzie la revista Pattern Recognition, R. Coliban, M. Ivanovici, N. Richard, *Improved probabilistic pseudo-morphology for noise reduction in color images*.
 - Creșterea reputației științifice personale, atât la nivel național cât și internațional și, implicit, a reputației laboratorului, a departamentului, a facultății și a universității;

Obiective cu privire la activitatea didactică

- Rafinarea programelor de studii, în concordanță cu cele mai noi realizări ale cercetării științifice din domeniul microelectronicii, a achiziției, prelucrării și analizei de semnale, date și imagini color, multi și hiperspectrale;
- Dezvoltarea, rafinarea și actualizarea continuă a conținutului cursurilor predate, precum și a metodelor și mijloacelor de predare;
- Organizarea de evenimente științifice pentru studenți, precum școli de vară și workshop-uri.

Planul de dezvoltare a carierei universitare

Pentru îndeplinirea obiectivelor propuse, am în vedere următorul plan de dezvoltare a carierei universitare.

¹⁰Romanian Space Agency.

Planul de dezvoltare a activității de cercetare

- Dezvoltarea domeniului de interes științific principal, prin elaborarea de noi metrici și algoritmi pentru analiza/caracterizarea texturilor color, multispectrale și hiperspectrale, precum și noi algoritmi pentru segmentarea imaginilor multivariate (color, multi și hiperspectrale) – toate acestea bazate pe geometria și analiza fractală, precum și morfologie matematică. De menționat, că o direcție aparte, în vederea elaborării de noi unelte de analiză fractală, o constituie pseudo-morfologia matematică pentru imagini color, în sens larg - multivariate, direcție în care am propus în 2011 o abordare probabilistică a rezolvării problemei alegerii extremelor unei mulțimi multi-dimensionale, ce deschide noi orizonturi de cercetare;
- Implicarea în realizarea de parteneriate, proiecte, programe, activități sau contracte de colaborare. La nivel internațional, începând cu anul 2007 am menținut colaborarea cu CERN, Organizația Europeană de Cercetări Nucleare, unde am realizat cercetările ce au condus la elaborarea tezei mele de doctorat. De asemenea, am realizat legături cu laboratoare de cercetare și universități din Franța și Germania. La nivel național, prin prisma proiectelor comune, am colaborat cu Universitatea Politehnică din București, Universitatea Tehnică din Cluj-Napoca și Universitatea din Oradea, dar și cu Institutul de Fizică și Inginerie Nucleară Horia Hulubei, Măgurele, Institutul Național Delta Dunării, Tulcea și Institutul Național de Cercetare-Dezvoltare pentru Cartof și Sfeclă de Zahăr, Brașov. În perioada 2012 - 2015 am ocupat poziția de responsabil Erasmus al Facultății de Inginerie Electrică și Știința Calculatoarelor pentru a avea ocazia de a dezvolta noi parteneriate cu universități și institute de cercetare din străinătate. Menționez și colaborările din cadrul Universității Transilvania din Brașov cu colegi de la Facultățile de Matematică-Informatică, Medicină, Silvicultură și Exploatarea Forestiere care constituie baza elaborării unor noi proiecte de cercetare;
- Continuarea colaborării cu laboratorul de cercetare XLIM-SIC de la Universitatea din Poitiers, Franța, în domeniul analizei texturii color și a segmentării imaginilor color. În 2007, datorită mentorului meu domnul profesor Vasile Buzuloiu, am demarat o serie de activități de cercetare împreună cu prof. Christine Fernandez-Maloigne și conf. Noël Richard de la Laboratorul XLIM-SIC din Poitiers, Franța, care au condus la stagii de cercetător sau profesor invitat, la mai multe publicații comune, inclusiv în reviste cu factor mare de impact sau la edituri de renume (e.g. Springer), propuneri de proiecte FP7 sau regionale. În continuare, vom elabora noi articole științifice, noi publicații comune, vom continua eforturile de accesare de fonduri europene pentru

realizarea de proiecte de cercetare, vom crea condițiile efectuării de stagii pentru studenții și doctoranzii facultății noastre în cadrul laboratorului XLIM-SIC, vom asigura cadrul propice pentru desfășurarea de evenimente științifice comune (e.g. școli de vară internaționale) ș.a.m.d.;

- Realizarea de noi legături cu laboratoare și institute de cercetare din țară și străinătate, în vederea creării unei rețele adecvate accesării de fonduri europene. Prin prisma poziției actuale, dar și a activității desfășurate până acum, estimez crearea de noi legături în anii ce urmează – o premisă obligatorie pentru formarea de rețele de excelență necesare accesării de fonduri europene;
- Atragerea de fonduri prin granturi și proiecte de cercetare. Din anul 2007 am desfășurat o intensă activitate de realizare de propuneri de proiect și încheiere de contracte cu industria, bugetele proiectelor implementate până acum ca director de proiect însumând peste 1.250.000 de lei, fonduri atrase exclusiv pentru Universitatea Transilvania din Brașov (în plus, am colaborat la scrierea și implementarea în perioada aprilie 2014 - septembrie 2015, a două proiecte POSDRU ale Școlii Doctorale Interdisciplinare a universității). În acest sens voi continua redactarea de propuneri de proiect pentru competițiile naționale organizate de UEFISCDI, ROSA dar și pentru cele internaționale, precum și realizarea de contracte cu firme din industrie.
- Participarea la conferințe naționale și internaționale în domeniile prelucrării și analizei imaginilor și microelectronicii pentru fizica particulelor, precum și încurajarea participării viitorilor doctoranzi—un element important în formarea acestora. Participarea la aceste conferințe vizează în egală măsură și stabilirea de noi legături/colaborări. Voi continua activitatea de publicare, vizând în special conferințe ale căror lucrări sunt indexate ISI Thompson;
- Organizarea de sesiuni, inclusiv speciale, în cadrul conferințelor naționale și internaționale, atât din țară cât și din străinătate. M-am implicat în acest sens în propunerea și coordonarea de sesiuni speciale în 2010, 2012 și 2014 în cadrul conferinței internaționale IEEE OPTIM (Optimization of Electrical and Electronic Equipment), organizată de către Facultatea de Inginerie Electrică și Știința Calculatoarelor. De asemenea, ținând cont de implicarea mea în organizarea altor conferințe, estimez că vor urma și alte ocazii în care să mă implic în organizarea de sesiuni în cadrul diverselor conferințe internaționale;
- Diseminarea rezultatelor cercetărilor și redactarea a cel puțin două articole de revistă pe an și trimiterea lor spre publicare la reviste cu SRI mare. Nu doar prin prisma standardelor minimale impuse de către

Legea educației naționale nr. 1 / 2011 cu privire la avansarea pe postul de profesor universitar, dar mai ales din nevoia unei vizibilități la nivel național și internațional și de acceptare în rândul comunității științifice internaționale, precum și prin prisma publicațiilor mele recente, dar și a invitațiilor de a face recenzii pentru articole, s-a conturat obligația din punct de vedere științific de a publica în cele mai vizibile reviste la nivel internațional, cum ar fi IEEE Transactions on Image Processing sau Elsevier Pattern Recognition – o premisă atât pentru dezvoltarea personală și profesională, dar și a creșterii prestigiului personal și instituțional, în special a centrului de cercetare C13 din cadrul Institutului CDI al Universității Transilvania din Brașov;

- Supervizarea studenților masteranzi și doctoranzi în vederea realizării de cercetări în domeniul prelucrării și analizei de imagini și redactării de articole științifice. Activitatea de mentorat pentru viitorii cercetători este vitală pentru asigurarea și formarea resurselor umane noi pentru activitatea de cercetare. Actualmente, desfășor activități de co-îndrumare a unei teze de doctorat (drd. ing. Radu Coliban) și am co-îndrumat două teze de doctorat conduse de prof. dr. ing. Gheorghe Toacșe care au fost susținute cu succes la finele lui 2013 și confirmate de CNATDCU (dr. ing. Alexandru Căliman și dr. ing. Simona-Maria Banu). Implicarea într-o astfel de activitate a fost o ocazie bună pentru a dobândi experiența necesară pentru conducerea de doctorate, un deziderat în cariera mea universitară la momentul de față;
- Aplicarea pentru o bursă Humboldt sau Fulbright în vederea efectuării unui stagiu de cercetare într-o universitate din Germania sau Statele Unite ale Americii, în vederea consolidării poziției de cercetător și creșterii vizibilității cercetărilor la nivel internațional, dar și rafinarea abilităților de mentor.

Planul de dezvoltare a activității didactice

- Efectuarea de stagii Erasmus la universități partenere din străinătate, în special Franța și Germania, pentru a fi la curent cu ultimele metode și mijloace de predare. Utilizarea cât mai des a mijloacelor moderne existente deja în dotarea sălilor de curs/seminar sau laborator ale facultății, cum ar fi tabla interactivă inteligentă, precum și a echipamentelor achiziționate în cadrul proiectelor derulate sau aflate în derulare (e.g. sistemul profesional de achiziție imagine/video);
- Utilizarea metodelor activ-participative în activitățile didactice pentru asigurarea implicării studenților în propria formare;

- Folosirea strategiilor didactice axate pe formarea competențelor vizate de programă;
- Folosirea conținuturilor care să îmbine aspectele teoretice cu cele practice, care să promoveze interdisciplinaritatea;
- Utilizarea unor instrumente diverse și moderne de evaluare a activității studenților (portofolii, referate, proiecte ș.a.m.d.);
- Îndrumarea și stimularea studenților în vederea participării la competiții de specialitate. Menționez aici participarea cu studenții și obținerea de premii la concursurile organizate de către firma Continental din Sibiu și firma Digilent din Cluj-Napoca în colaborare cu Universitatea Tehnică din Cluj-Napoca;
- Organizarea în continuare a școlii internaționale de vară ISIP (International School on Image Processing), cu o istorie de 7 ediții deja (anual în perioada 2009 - 2015) sau a unor școli de vară itinerante (e.g. IPCV 2014 care a beneficiat chiar și de finanțare IEEE Signal Processing Society) pentru studenții, doctoranzii și tinerii cercetători din departament și nu numai;
- Organizarea de workshop-uri pentru studenți, masteranzi și doctoranzi;
- Continuarea organizării de concursuri pentru elevi și studenți. Menționez aici concursul LED organizat în 2011 pentru elevii de liceu și concursurile organizate în 2012 și în 2013 (cel din 2012 în colaborare cu firma ROUTE 66 din Brașov);
- Implicarea în activități de proiectare și redactare a ofertei educaționale la nivelul departamentului, atât în ceea ce privește noi programe de master dar și programe de formare continuă.

În final, trebuie să menționez ca fiind obligatorie corelarea activității de cercetare cu cea didactică, în vederea îmbunătățirii acestora, prin următoarele acțiuni conjugate:

- Rafinarea cursurilor, dar și a planurilor de învățământ existente, la nivel de conținut, structură de organizare, metode de evaluare, introducerea de noi discipline;
- Promovarea celor mai noi descoperiri în domeniul metodologiei (e.g. noi laboratoare de specialitate, noi sisteme de evaluare a cunoștințelor sau competențelor);

- Propunerea de noi domenii de formare și/sau perfecționare. Dată fiind viteza cu care evoluează domeniul prelucrării și analizei imaginilor color și multispectrale, ca urmare a dezvoltărilor tehnologice (e.g. noi instrumente de achiziție a imaginilor color și multispectrale sau implementări ale paradigmelor noi de calcul, cum ar fi GPU), a algoritmilor și cerințelor noilor aplicații, se impune o continuă activitate de inovare inclusiv în planul formării tinerilor cercetători;
- Atragerea și implicarea studenților în activitatea de cercetare științifică, în special în contextul proiectelor și contractelor de cercetare în desfășurare în cadrul centrului de cercetare C13.

Consider că abilitarea pentru conducere de doctorat îmi va oferi șansa de realizare a planului de dezvoltare a carierei universitare prezentat, iar activitatea mea științifică și didactică desfășurată până în prezent constituie o garanție a îndeplinirii obiectivelor propuse.

Subpart II.3
Bibliography

Bibliography

- [1] E.I. Tsompanaki A.G. Manousaki, A.G. Manios and A.D. Tosca. Use of color texture in determining the nature of melanocytic skin lesions - a qualitative and quantitative approach. *Computers in Biology and Medicine*, 36:416–427, 2006.
- [2] J. Angulo. *Morphologie mathématique et indexation d'images couleur. Application à la microscopie en biomédecine*. Centre de Morphologie Mathématique, Ecole des Mines de Paris, France, 2003.
- [3] J. Angulo. Morphological colour operators in totally ordered lattices based on distances: Application to image filtering, enhancement and analysis. *Computer Vision and Image Understanding*, 107(1 - 2):56 – 73, 2007.
- [4] J. Angulo. Pseudo-morphological image diffusion using the counter-harmonic paradigm. In J. Blanc-Talon, D. Bone, W. Philips, D. Popescu, and P. Scheunders, editors, *Advanced Concepts for Intelligent Vision Systems*, volume 6474 of *Lecture Notes in Computer Science*, pages 426–437. Springer Berlin Heidelberg, 2010.
- [5] E. Aptoula and S. Lefèvre. A comparative study on multivariate mathematical morphology. *Pattern Recognition*, 40(11):2914–2929, November 2007.
- [6] E. Aptoula and S. Lefèvre. On morphological color texture characterization. In *Proceedings of the 8th international symposium on mathematical morphology*, ISMM '07, pages 153–164, 2007.
- [7] E. Aptoula and S. Lefèvre. α -trimmed lexicographical extrema for pseudo-morphological image analysis. *Journal of Visual Communication and Image Representation*, 19(3):165 – 174, 2008.
- [8] E. Aptoula and S. Lefèvre. α -trimmed lexicographical extrema for pseudo-morphological image analysis. *Journal of Visual Communication and Image Representation*, 19(3):165 – 174, 2008.
- [9] V. Arvis, C. Debain, M. Berducot, and A. Benassi. Generalization of the cooccurrence matrix for colour images: application to colour texture classification. *Image Analysis and Stereology*, 23(1), 2011.
- [10] J.-M. Bardet. Dimension de corrélation locale et dimension de hausdorff des processus vectoriels continus - local correlation dimension and hausdorff dimension of continuous random fields. *Comptes Rendus de l'Académie des Sciences - Series I - Mathematics*, 326(5):589 – 594, 1998.
- [11] V. Barnett. The ordering of multivariate data. *Journal of the Royal Statistical Society*, 139(3):318 – 355, 1976.
- [12] M. V. Berry and Z. V. Lewis. On the weierstrass-mandelbrot fractal function. *Proceedings of the Royal Society of London A: Mathematical, Physical and Engineering Sciences*, 370(1743):459–484, 1980.
- [13] S. Beucher. Watersheds of functions and picture segmentation. *Acoustics, Speech, and Signal Processing, IEEE International Conference on ICASSP '82.*, 7:1928 – 1931, may 1982.

- [14] S Beucher. Watershed, hierarchical segmentation and waterfall algorithm. In J Serra and P Soille, editors, *Mathematical Morphology And Its Applications To Image Processing*, volume 2 of *Computational Imaging And Vision*, pages 69–76, 1994.
- [15] G Bouligand. Ensembles impropres et nombre dimensionnel. *Bull. Sci. Math.*, 52:320 – 344, 1928.
- [16] B. Burgeth and A. Kleefeld. Morphology for color images via Loewner order for matrix fields. In C. L. Hendriks, G. Borgefors, and R. Strand, editors, *Mathematical Morphology and Its Applications to Signal and Image Processing*, volume 7883 of *Lecture Notes in Computer Science*, pages 243–254. Springer Berlin Heidelberg, 2013.
- [17] A Caliman, M. Ivanovici, and N. Richard. Probabilistic pseudo-morphology for greyscale and color images. *Pattern Recognition*, 47(2):721 – 735, 2014.
- [18] A Caliman, M. Ivanovici, N. Richard, and G. Toacse. A multivariate mathematical morphology based on orthogonal transformation, probabilistic extrema estimation and distance optimization. In C. L. Hendriks, G. Borgefors, and R. Strand, editors, *Mathematical Morphology and Its Applications to Signal and Image Processing*, volume 7883 of *Lecture Notes in Computer Science*, pages 255–266. Springer Berlin Heidelberg, 2013.
- [19] Alexandru Caliman, Mihai Ivanovici, and Radu-Mihai Coliban. Pseudo-granulometry and morphological covariance for color psoriasis image segmentation. In *E-Health and Bioengineering Conference (EHB), 2013*, pages 1–4, 2013.
- [20] J. Canny. A computational approach to edge detection. *IEEE transactions on Pattern Analysis and Machine Intelligence*, 8(6):679–698, November 1986.
- [21] A. Carleer, O. Debeir, and E. Wolff. Assessment of very high spatial resolution satellite image segmentations. *Photogrammetric Engineering and Remote Sensing*, 71(11):1285–1294, 2005.
- [22] J. Chanussot and P. Lambert. Total ordering based on space filling curves for multivalued morphology. In *Proceedings of the 4th international symposium on Mathematical morphology and its applications to image and signal processing*, ISMM '98, pages 51–58, Norwell, MA, USA, 1998. Kluwer Academic Publishers.
- [23] Jocelyn Chanussot and Patrick Lambert. Watershed approaches for color image segmentation. In *NSIP'99*, pages 129–133, 1999.
- [24] B.B. Chaudhuri and N. Sarkar. Texture segmentation using fractal dimension. *IEEE transactions on Pattern analysis and Machine Intelligence*, 17(1):72–77, January 1995.
- [25] P. Chebyshev. Des valeurs moyennes. *Journal de mathématiques pures et appliquées*, 2(12):177–184, 1867.
- [26] W.S. Chen, S.Y. Yuan, H. Hsiao, and C.M. Hsieh. Algorithms to estimating fractal dimension of textured images. *IEEE International conferences on Acoustics, Speech and Signal Processing (ICASSP)*, 3:1541–1544, May 2001.
- [27] Chao-Yu Chi and Shen-Chuan Tai. Perceptual color contrast based watershed for color image segmentation. In *Systems, Man and Cybernetics, 2006. SMC '06. IEEE International Conference on*, volume 4, pages 3548 –3553, oct. 2006.
- [28] Laurent D. Cohen. On active contour models and balloons. *CVGIP: Image Underst.*, 53:211–218, March 1991.
- [29] R.-M. Coliban and M. Ivanovici. Color and multispectral texture characterization using pseudo-morphological tools. In *Image Processing (ICIP), 2014 IEEE International Conference on*, pages 630–634, Oct 2014.

- [30] M. L. Comer and E. J. Delp. Morphological operations for color image processing. *Journal of Electronic Imaging*, 8:279–289, July 1999.
- [31] M. Couprie and G. Bertrand. Topological gray-scale watershed transform. In *Proc. of SPIE Vision Geometry V*, volume 3168, pages 136–146, 1997.
- [32] J. Cousty, G. Bertrand, L. Najman, and M. Couprie. Watershed cuts: Minimum spanning forests and the drop of water principle. *Pattern Analysis and Machine Intelligence, IEEE Transactions on*, 31(8):1362–1374, aug. 2009.
- [33] G.R. Cross and A.K. Jain. Markov random field texture models. *IEEE Transactions on Pattern Analysis and Machine Intelligence*, PAMI(1):25–39, 1983.
- [34] B. A. Davey and H. A. Priestley. *Introduction to Lattices and Order*. Cambridge University Press, 2 edition, 2002.
- [35] Y. Deng and B. S.Manjunath. Unsupervised segmentation of color-texture regions in images and video. *IEEE Transactions on Pattern Analysis and Machine Intelligence (PAMI '01)*, 23(8):800–810, August 2001.
- [36] B. Dubuc, S. W. Zucker, C. Tricot, J. F. Quiniou, and D. Wehbi. Evaluating the fractal dimension of surfaces. *Proc. R. Soc. Lond. A*, 425:113–127, 1989.
- [37] G. Edgar. *Measure, Topology, and Fractal Geometry*. Springer, 2007.
- [38] Gerald Edgar. *Measure, Topology and Fractal Geometry*. Springer Verlag, New York, 1990.
- [39] A. N. Evans. Vector area morphology for motion field smoothing and interpretation. *IEE Proceedings in Vision, Image and Signal Processing*, 150(4):219–226, 2003.
- [40] K. Falconer. *Fractal Geometry, mathematical foundations and applications*. John wiley and Sons, 1990.
- [41] R.A. Feagin. Heterogeneity versus homogeneity : a conceptual and mathematical theory in terms of scale-invariant and scale-covariant distributions. *Ecological Complexity*, 2:339–356, 2005.
- [42] A. Fournier, D. Fussell, and L. Carpenter. Computer rendering of stochastic models. *Communications of the ACM*, 25(6):371–384, 1982.
- [43] G.W. Frazer, M.A. Wulder, and K.O. Niemann. Simulation and quantification of the fine-scale spatial pattern and heterogeneity of forest canopy structure : a lacunarity -based method designed for analysis of continuous canopy heights. *Forest ecology and management*, 214:65–90, 2005.
- [44] K.S. Fu and J.K. Mui. A survey on image segmentation. *Pattern Recognition*, 13(1):3 – 16, 1981.
- [45] J.J. Gagnepain and C. Roques-Carmes. Fractal approach to two-dimensional and three-dimensional surface roughness. *Wear*, 109(1 - 4):119 – 126, 1986.
- [46] Rafael C. Gonzalez and Richard E. Woods. *Digital Image Processing (3rd Edition)*. Prentice-Hall, Inc., Upper Saddle River, NJ, USA, 2006.
- [47] J. Goutsias and H. J. A. M. Heijmans. Fundamenta morphologicae mathematicae. *Fundamenta Informaticae - Special issue on mathematical morphology*, 41(1-2):1–31, January 2000.
- [48] Peter Grassberger and Itamar Procaccia. Measuring the strangeness of strange attractors. *Physica D: Nonlinear Phenomena*, 9(1-2):189 – 208, 1983.
- [49] Chuang Gu. Multivalued morphology and its application in moving object segmentation and tracking. In Petros Maragos, RonaldW. Schafer, and MuhammadAkmal Butt, editors, *Mathematical Morphology and its Applications to Image and Signal Processing*, volume 5 of *Computational Imaging and Vision*, pages 345–352. Springer US, 1996.

- [50] A. Hanbury and J. Serra. Mathematical morphology in the hls colour space. In *12th British Machine Vision Conference*, pages 451–460, Manchester, UK, 2001.
- [51] A. Hanbury and J. Serra. Morphological operators on the unit circle. *IEEE Transactions on Image Processing*, 10(12):1842–1850, 2001.
- [52] A. Hanbury and J. Serra. Mathematical morphology in the cielab space. *Image Analysis and Stereology*, 21(3):201–206, 2002.
- [53] R. Haralick, K. Shanmugam, and I. Dinstein. Textural feature for image classification. In *IEEE Transactions on System Man and Cybernetics*, volume 3(6), pages 610–621, November 1973.
- [54] R.M. Haralick and L.G. Shapiro. Image segmentation techniques. *Computer Vision, Graphics, & Image Processing*, 29(1):100–132, 1985.
- [55] R.M. Haralick, S.R. Sternberg, and X. Zhuang. Image analysis using mathematical morphology. *IEEE Transactions on Pattern Analysis and Machine Intelligence*, 9(4):532–550, 1987.
- [56] G. H. Hardy. Weierstrass’s non-differentiable function. *Transactions of the American Mathematical Society*, 17(3):pp. 301–325, 1916.
- [57] C Harris and M Stephens. *A Combined Corner and Edge Detection*, volume 15, pages 147–151. 1988.
- [58] H. J. A. M. Heijmans and C. Ronse. The algebraic basis of mathematical morphology. 1 - dilations and erosions. *Computer Vision, Graphics, and Image Processing*, 50(3):245–295, 1990.
- [59] Q. Huang, J.R. Lorch, and R.C. Dubes. Can the fractal dimension of images be measured ? *Pattern Recognition*, 27(3):339–349, Mars 1994.
- [60] M. Ivanovici, A Caliman, N. Richard, and C. Fernandez-Maloigne. Towards a multivariate probabilistic morphology for colour images. In *Proceedings of the 6th European Conference on Colour in Graphics, Imaging and Vision*, pages 189 – 193, Amsterdam, the Netherlands, May 6-9 2012.
- [61] M. Ivanovici and N. Richard. Colour fractal image generation. In *International Conference on Image Processing, Computer Vision and Pattern Recognition*, pages 93–96, Las Vegas, Nevada, USA, July 13-16 2009.
- [62] M. Ivanovici and N. Richard. The lacunarity of colour fractal images. In *ICIP’09 - IEEE International Conference on Image Processing*, pages 453–456, Cairo, Egypt, November 7-11 2009.
- [63] M. Ivanovici and N. Richard. Fractal dimension of colour fractal images. *IEEE Transactions on Image Processing*, 20(1):227–235, January 2011.
- [64] M. Ivanovici and D. Stoica. Color diffusion model for active contours - an application to skin lesion segmentation. In *Engineering in Medicine and Biology Society (EMBC), 2012 Annual International Conference of the IEEE*, pages 5347–5350, Aug 2012.
- [65] A.K. Jain and F. Farrokhnia. Unsupervised texture segmentation using gabor filters. In *Systems, Man and Cybernetics, 1990. Conference Proceedings., IEEE International Conference on*, pages 14–19, 1990.
- [66] Anil K. Jain. *Fundamentals of digital image processing*. Prentice-Hall, Inc., Upper Saddle River, NJ, USA, 1989.
- [67] Xu Jing, Wu Jian, Ye Feng, and Cui Zhi-ming. A level set method for color image segmentation based on bayesian classifier. In *Computer Science and Software Engineering, 2008 International Conference on*, volume 2, pages 886 –890, dec. 2008.

- [68] Tina Kapur, W. Eric L. Grimson, and Ron Kikinis. Segmentation of brain tissue from mr images. In *Proceedings of the First International Conference on Computer Vision, Virtual Reality and Robotics in Medicine*, CVRMed '95, pages 429–433, London, UK, 1995. Springer-Verlag.
- [69] Michael Kass, Andrew Witkin, and Demetri Terzopoulos. Snakes: Active contour models. *International Journal of Computer Vision*, 1(4):321–331, 1988.
- [70] J.M. Keller and S. Chen. Texture description and segmentation through fractal geometry. *Computer Vision, Graphics and Image processing*, 45:150–166, 1989.
- [71] J. Kolasa and C.D. Rollo. *Ecological heterogeneity (Ecological Studies)*, chapter The heterogeneity of heterogeneity: a glossary, pages 1–23. Springer-Verlag, New-York, 1 edition, May 1991.
- [72] K.I. Laws. Rapid texture identification, 1980.
- [73] W.L. Lee, Y.C. Chen, and K.S. Hsieh. Ultrasonic liver tissues classification by fractal feature vector based on m-band wavelet transform. *IEEE Transactions on Medical Imaging*, 22:382–392, 2003.
- [74] Alex Levinshtein, Adrian Stere, Kiriakos N. Kutulakos, David J. Fleet, Sven J. Dickinson, and Kaleem Siddiqi. Turbopixels: Fast superpixels using geometric flows. *IEEE Trans. Pattern Anal. Mach. Intell.*, pages 2290–2297, 2009.
- [75] O. Lezoray, C. Charrier, and A. Elmoataz. Learning complete lattices for manifold mathematical morphology. In M. Wilkinson and J. Roerdink, editors, *Proceedings of the 9th International Symposium on Mathematical Morphology*, ISMM '09, pages 1–4, the Netherlands, 2009. University of Groningen.
- [76] B. Li and C. Loehle. Wavelet analysis of multiscale permeabilities in the subsurface. *Geophysical Research Letters*, 22(23):3123–3126, 1995.
- [77] H. Li and J. F. Reynolds. On definition and quantification of heterogeneity. *Oikos*, 73(2):280–284, June 1995.
- [78] G. Louverdis, M.I. Vardavoulia, I. Andreadis, and Ph. Tsalides. A new approach to morphological color image processing. *Pattern Recognition*, 35(8):1733 – 1741, 2002.
- [79] B.B. Mandelbrot. *The Fractal Geometry of Nature*. W.H. Freeman and Co, New-York, 1982.
- [80] P. Maragos. A representation theory for morphological image and signal processing. *IEEE Transactions on Pattern Analysis and Machine Intelligence*, 11(6):586–599, June 1989.
- [81] P. Maragos and F.K. Sun. Measuring the fractal dimension of signals: morphological covers and iterative optimization. *IEEE Transactions on signal Processing*, 41(1):108–121, January 1993.
- [82] D. Martin, C. Fowlkes, D. Tal, and J. Malik. A database of human segmented natural images and its application to evaluating segmentation algorithms and measuring ecological statistics. In *Proc. 8th International Conference on Computer Vision*, volume 2, pages 416–423. July 2001.
- [83] G. Matheron. *Random sets and integral geometry*. John Wiley and Sons, Inc., 1975.
- [84] Hans Moravec. Obstacle avoidance and navigation in the real world by a seeing robot rover. In *tech. report CMU-RI-TR-80-03, Robotics Institute, Carnegie Mellon University & doctoral dissertation, Stanford University*, number CMU-RI-TR-80-03. September 1980.
- [85] F. Murtagh, A. Alexander, A. Bouridane, D. Crookes, J. Campbell, J. Starck, F. Bonnarel, and Z. Geradts. Fractal and multiscale method for content-based

- image retrieval. In J.G. Campbell and editors F.D. Murtagh, editors, *IMVIP 2000, Irish Machine Vision and Image Processing Conference 2000*, pages 175–183, Belfast(Ireland), August 2000.
- [86] F. K. Musgrave, C. E. Kolb, and R. S. Mace. The synthesis and rendering of eroded fractal terrains. *SIGGRAPH Comput. Graph.*, 23(3):41–50, July 1989.
- [87] Kenton Musgrave. *Methods for Realistic Landscape Imaging*. PhD thesis, Yale University, May 1993.
- [88] N. Nikolaou and N. Papamarkos. Color image retrieval using a fractal signature extraction technique. *Engineering Applications of Artificial Intelligence*, 15(1):81–96, Février 2002.
- [89] T. Ojala, T. Mäenpää, M. Pietikäinen, J. Viertola, J. Kyllönen, and S. Huovinen. Outex - new framework for empirical evaluation of texture analysis algorithms. In *Proceedings of the 16th International Conference on Pattern Recognition - Volume 1, ICPR02*, Washington, DC, USA, 2002. IEEE Computer Society.
- [90] Nikhil R Pal and Sankar K Pal. A review on image segmentation techniques. *Pattern Recognition*, 26(9):1277 – 1294, 1993.
- [91] A. Papoulis. *Probability, random variables, and stochastic processes*. McGraw-Hill, 3rd edition, 1991.
- [92] K. Pearson. On lines and planes of closest fit to systems of points in space. *Philosophical Magazine*, 2(6):559–572, 1901.
- [93] H.O. Peitgen and D. Saupe. *The sciences of fractal images*. Springer Verlag, 1988.
- [94] S. Peleg, J. Naor, R. Hartley, and D. Avnir. Multiple resolution texture analysis and classification. *Pattern Analysis and Machine Intelligence, IEEE Transactions on*, PAMI-6(4):518 –523, july 1984.
- [95] Ken Perlin. An image synthesizer. *SIGGRAPH Comput. Graph.*, 19(3):287–296, July 1985.
- [96] M. Petrou and P. G. Sevilla. *Image Processing: Dealing with Texture*. John Wiley and Sons, 2006.
- [97] Antonio Plaza, Pablo Martinez, Rosa Perez, and Javier Plaza. A new approach to mixed pixel classification of hyperspectral imagery based on extended morphological profiles. *Pattern Recognition*, 37(6):1097 – 1116, 2004.
- [98] R.E. Plotnick, R.H. Gardner, and R.V. O’Neill. Lacunarity indices as measures of landscape texture. *Landscape Ecology*, 8(3):201–211, 1993.
- [99] Lutz Priebe and Volker Rehrmann. On hierarchical color segmentation and applications. In *Proceedings*, pages 633–634. Proceedings of the Conference on Computer Vision and Pattern Recognition, 1993.
- [100] J. Randall, L. Guan, W. Li, and X.Zhang. The hcm for perceptual image segmentation. *Neurocomputing*, 71(10-12):1966–1979, June 2008.
- [101] N. Richard, M. Léard, and V. Legeay. Classification of roadway asphalt by use of fractal signature. In *QCAV99*, pages 57–62, Quebec (Canada), Mai 1999.
- [102] J.F. Rivest, P. Soille, and S. Beucher. Morphological gradients. In Editors Edward R. Dougherty; Jaakko T. Astola; Charles G. Boncelet, Jr., editor, *SPIE - Non Linear Processing III*, pages 139–150. SPIE, April 1992.
- [103] Jos B.T.M. Roerdink and Arnold Meijster. The watershed transform: Definitions, algorithms and parallelization strategies. *Fundamenta Informaticae*, 41:187–228, 2001.
- [104] S. Roman. *Lattices and Ordered Sets*. Springer Science, 2009.

- [105] C. Ronse. Why mathematical morphology needs complete lattices. *Signal Processing*, 21(2):129 – 154, 1990.
- [106] Azriel Rosenfeld. Connectivity in digital pictures. *J. ACM*, 17(1):146–160, 1970.
- [107] K. Saارينen. Color image segmentation by a watershed algorithm and region adjacency graph processing. In *Image Processing, 1994. Proceedings. ICIP-94., IEEE International Conference*, volume 3, pages 1021 –1025 vol.3, November 1994.
- [108] N. Sarkar and B.B. Chaudhuri. An efficient differential box-counting approach to compute fractal dimension of image. *IEEE Transactions on Systems, Man and Cybernetics*, 24(1):115–120, January 1994.
- [109] D. Saupe. Point evaluation of multi-variable random fractals. In H. Juergen and D. Saupe, editors, *Visualisierung in Mathematik und Naturwissenschaft - Bremer Computergraphik Tage 1988*. Springer-Verlag, Heidelberg, 1989.
- [110] J. Serra. *Image Analysis and Mathematical Morphology*, volume I. Academic Press, 1982.
- [111] Jean Serra. A lattice approach to image segmentation. *J. Math. Imaging Vis.*, 24:83–130, January 2006.
- [112] R. Seve. Practical formula for the computation of CIE 1976 hue difference. *Color Research and Application*, 21(4):314–314, 1996.
- [113] K. Sivakumar and J. Goutsias. Discrete morphological size distributions and densities: estimation techniques and applications. *Journal of Electronic Imaging*, 6(1):31–53, 1997.
- [114] P. Soille. *Morphological Image Analysis: Principles and Applications*. Springer-Verlag, 2002.
- [115] R. P. Taylor, B. Spehar, C. W. G. Clifford, and B. R. Newell. The visual complexity of pollock’s dripped fractals. In *Proceedings of the International Conference of Complex Systems*, 2002. <http://materialsscience.uoregon.edu/taylor/art/Taylor1CCS2002.pdf>.
- [116] D. Terzopoulos. Deformable models: Classic, topology-adaptive and generalized formulations. In S. Osher and N. Paragios, editors, *Geometric Level Set Methods in Imaging, Vision, and Graphics*, chapter 2, pages 21–40. Springer-Verlag, New York, 2003.
- [117] M. Tuceryan and A. K. Jain. Texture analysis. In *The Handbook of Pattern Recognition and Computer Vision*, pages 207–248. World Scientific Publishing Co., 1998.
- [118] M. Turner, R.H. Gardner, and R.V. Odž“Neill. *Landscape Ecology in Theory and Practice: Pattern and Process*. Springerđ“Verlag, New York, 2001.
- [119] J. J. van de Gronde and J. B. T. M. Roerdink. Group-invariant frames for colour morphology. In C. L. Hendriks, G. Borgefors, and R. Strand, editors, *Mathematical Morphology and Its Applications to Signal and Image Processing*, volume 7883 of *Lecture Notes in Computer Science*, pages 267–278. Springer Berlin Heidelberg, 2013.
- [120] M. I. Vardavoulia, I. Andreadis, and P. Tsalides. Vector ordering and morphological operations for colour image processing: fundamentals and applications. *Pattern Anal. Appl.*, 5(3):271–284, 2002.
- [121] S. Velasco-Forero and J. Angulo. Mathematical morphology for vector images using statistical depth. In P. Soille, M. Pesaresi, and G. Ouzounis, editors, *Mathematical Morphology and Its Applications to Image and Signal Processing*, volume 6671 of *Lecture Notes in Computer Science*, pages 355–366. Springer Berlin-Heidelberg, 2011.

-
- [122] S. Velasco-Forero and J. Angulo. Random projection depth for multivariate mathematical morphology. *Selected Topics in Signal Processing, IEEE Journal of*, 6(7):753–763, nov. 2012.
- [123] R. Voss. Random fractals : characterization and measurement. *Scaling phenomena in disordered systems*, 10(1):51–61, 1986.
- [124] Karl Weierstrass. On continuous functions of a real argument which possess a definite derivative for no value of the argument. *Königlich Preussischen Akademie der Wissenschaften*, 2:71–74, 1895.
- [125] Andrew Witkin, Demetri Terzopoulos, and Michael Kass. Signal matching through scale space. *International Journal of Computer Vision*, 1:133–144, 1987.
- [126] Andrew P. Witkin. Scale-space filtering. In *International Joint Conference on Artificial Intelligence*, pages 1019–1022, 1983.
- [127] Qiang Wu and Kenneth R. Castleman. Image segmentation. In *Microscope Image Processing*, pages 159 – 194. Academic Press, Burlington, 2008.
- [128] Chenyang Xu and Jerry L. Prince. Gradient vector flow: A new external force for snakes. In *Proceedings of the 1997 Conference on Computer Vision and Pattern Recognition (CVPR '97)*, CVPR '97, pages 66–, Washington, DC, USA, 1997. IEEE Computer Society.
- [129] Chenyang Xu and Jerry L. Prince. Generalized gradient vector flow external forces for active contours. *Signal Process.*, 71:131–139, December 1998.
- [130] Chenyang Xu and Jerry L. Prince. Snakes, shapes, and gradient vector flow. *IEEE Transactions on Image Processing*, 7(3):359–369, 1998.
- [131] Yu-Jin Zhang. *Advances in Image and Video Segmentation*. IRM Press, 2006.